Development of the Polarized Hydrogen-Deuteride (HD) Target for Double-Polarization Experiments at LEPS

Takeshi Ohta
Department of Physics
& Research Center for Nuclear Physics
Osaka University
Advisor: Mamoru Fujiwara, Masaru Yosoi, Hideki Kohri

2012

Development of the Polarized Hydrogen-Deuteride (HD) Target for Double-Polarization Experiments at LEPS

(LEPS 二重偏極実験の為の偏極重水素化水素標的の開発)

Abstract

Hadron photoproduction experiments without a polarized target have been carried out in the laser-electron photon facility beam-line at SPring-8 (LEPS) since 2000. The hadron photoproduction of the ϕ, K, η, and π^0 mesons is studied by using linearly polarized photon beams with energies of $E_\gamma = 1.5 \sim 2.9$ GeV. At the LEPS facility, linearly and circularly polarized photons are produced by Backward-Compton scattering. An experiment for measuring a complete set of spin observables is expected to give important information to investigate the nucleon hidden structure and hadron photoproduction dynamics. Introduction of the polarized target is expected to conduct the LEPS experiment to the next stage. We plan to carry out hadron photoproduction experiments by using polarized photon beams and the polarized target. We have started to develop the polarized Hydrogen-Deuteride (HD) target since 2005. A polarized HD target is prepared at Research Center for Nuclear Physics Osaka University, and will be installed in the LEPS beam-line at SPring-8. As a first step, we produced the polarized HD target in 2008-2009. The HD gas was fed to a dilution refrigerator, and was solidified. Then, the HD was cooled down to 14 mK with a high magnetic field of 17 T. The polarization degree of about 84% is realized for the proton at T=14 mK and at the magnetic field of 17 T. The target was kept in a surrounding of the low temperature and the high magnetic field for 53 days to grow and freeze the polarization. After 53 days, the polarization degree and the relaxation time were measured and obtained as 40.8±2.3 (stat.)% and 112.8±0.1 (stat.) days, respectively. The relaxation time of 112.8 days is longer than the period of 60 days needed for taking data of investigating the nucleon hidden structure. The relaxation time will be lengthened by taking longer aging time. The measured polarization of 40.8% was smaller than the expected polarization of 84%. We infer that this low-polarization originates from two reasons. One is the circuit linearity of NMR. The magnitude of the signal changes 4000 times from 0.02% at 4.2 K with 1 T, which is the calibration point, to 84% at 14 mK with 17 T. The other is that the polarization did not grow to the expected value because of a small amount of ortho-H_2 in the HD gas. Extremely small amounts of ortho-H_2 and para-D_2 components in the purified HD gas do not grow the polarization of the HD target in this aging time. The appropriate amount of impurities in the HD is approximately an order of 0.01%. A device to analyze a concentration of ortho-H_2 with a high precision of about 0.001% was required in order to optimize the amount of impurities. In order to solve the aforementioned all technical problems, we have developed a new gas purification system and a gas analysis system for the polarized HD target production, and have improved the NMR measurement system for the experiment at SPring-8.

Contents

Part I

Chapter 1

Introduction

Section 1.1

Physics motivation

— 1.1.1 Strangeness content in the proton and neutron —

It is generally accepted that the low-energy properties of nucleon are well described in terms of three constituents consisting of u and d quarks. Therefore, some experimental results are very surprising. Experiments from the lepton deep inelastic scattering indicate that there may be non-negligible strange quark content in the nucleon, and the strange quarks may give 10-20% contributions to the nucleon spin [1, 2]. After these results, there are many experiments [3, 4, 5, 6, 7, 8] which show similar (~20%) or different conclusions (~0%). This spin-puzzle problem is actively discussed now. New experimental information on the $s\bar{s}$-quark content of the nucleon is expected to shed light on solving this discrepancy.

— 1.1.2 ϕ meson photoproduction —

The ϕ-meson photoproduction reaction from proton is dominated by the diffractive production mechanism described in the vector-meson-dominance model (VDM) through Pomeron exchange as shown in Fig. 1.1(a). Conventional meson exchanges such as one-pion exchange (OPE) are shown in Fig. 1.1(b). The OPE contributes incoherently to the unpolarized cross section and the polarization observables of our interest, while the interference of VDM and the knockout amplitudes gives very distinct contributions to the polarization observables. If the proton has the $s\bar{s}$-quark content, the $s\bar{s}$ knockout and uud knockout processes are expected to be possible reaction channels in case of the ϕ meson photoproduction as shown in Fig. 1.1(c, d). In case of the ϕ meson photoproduction on the neutron, the similar processes are possible.

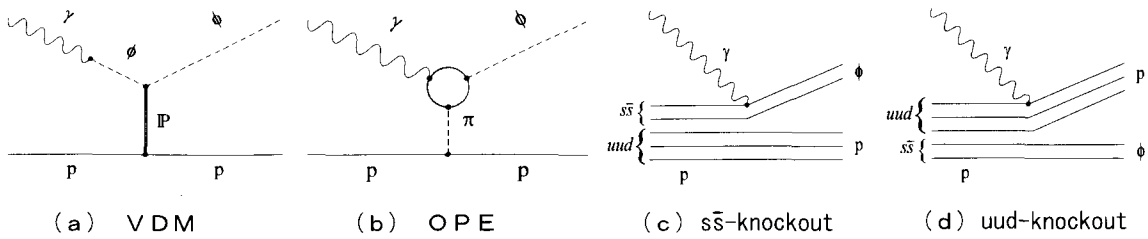

Figure 1.1: Feynman diagram of ϕ meson photoproduction.

— 1.1.3 Double polarization asymmetry —

The double polarization measurement is very sensitive to the $s\bar{s}$ contents in the proton. This has been firstly pointed out by Titov *et al* [9]. They found that the study of cross section in the small ϕ meson scattering angle region was not sensitive to the $s\bar{s}$-quark content in the nucleon. The cross section of VDM is ten times larger than that of the $s\bar{s}$ knockout process, as shown in Fig. 1.2. But the beam-target asymmetry (C_{zz}^{BT}) for the $s\bar{s}$ direct knockout process (Fig. 1.1(c)) is very sensitive to the $s\bar{s}$-quark content in the nucleon (Fig. 1.3) [9].

The interference between the VDM amplitudes and the knockout amplitude gives distinct contributions to the asymmetry at small ϕ meson angles. The beam-target asymmetry C_{zz}^{BT} is defined as

$$C_{zz}^{BT} = \frac{\mathrm{d}\sigma(\rightrightarrows) - \mathrm{d}\sigma(\rightleftarrows)}{\mathrm{d}\sigma(\rightrightarrows) + \mathrm{d}\sigma(\rightleftarrows)} = \frac{\mathrm{d}\sigma(\frac{3}{2}) - \mathrm{d}\sigma(\frac{1}{2})}{\mathrm{d}\sigma(\frac{3}{2}) + \mathrm{d}\sigma(\frac{1}{2})} \tag{1.1}$$

where $\mathrm{d}\sigma$ represents $\mathrm{d}\sigma/\mathrm{d}t$, and $\frac{1}{2}$ and $\frac{3}{2}$ denote the sum of the initial proton and photon helicities. The polarized target enables the measurement of double polarization asymmetries in ϕ meson photoproduction to study the strangeness content in proton and neutron.

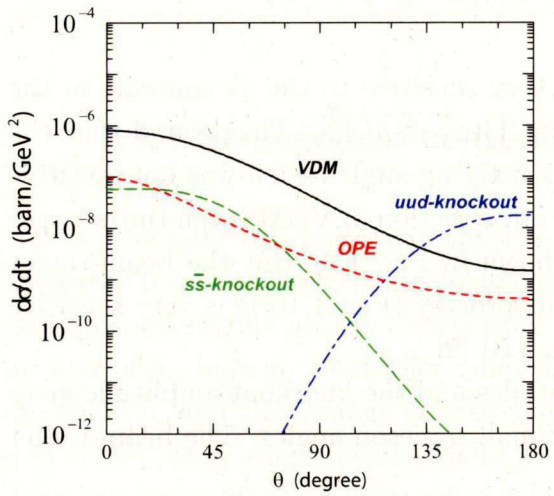

Figure 1.2: The unpolarized ϕ photoproduction cross section $d\sigma/dt$ at E_γ=2.0 GeV. The solid, dotted, dashed, and dot-dashed lines give the cross sections of VDM, OPE, $s\bar{s}$ knockout process, and uud knockout with strangeness admixture of 1% [9].

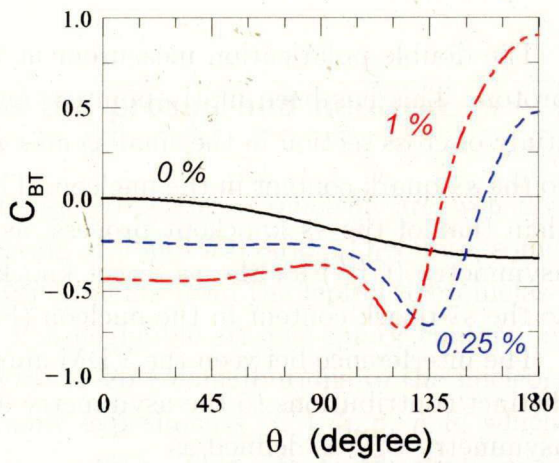

Figure 1.3: The beam-target asymmetry C^{BT} is plotted as a function of the scattering angle of ϕ-meson. Strangeness quark content is assumed to be 0% (solid), 0.25% (dashed), and 1% (dot-dashed) [9].

Section 1.2
LEPS facilities

The polarized HD target will be used at the laser-electron photon facility at the SPring-8 (LEPS), Japan. At SPring-8 BL33LEP beam-line (LEPS facility), the linearly-polarized photon is produced by laser backward Compton scattering. The experimental apparatus for the measurement is described in this section.

— 1.2.1 SPring-8 —

SPring-8, an acronym of **S**uper **P**hoton **ring-8** GeV facility, is the most powerful third-generation synchrotron radiation facility with 62 beam-lines. Figure 1.4 shows a schematic view of SPring-8 accelerator complex. The accelerator complex consists

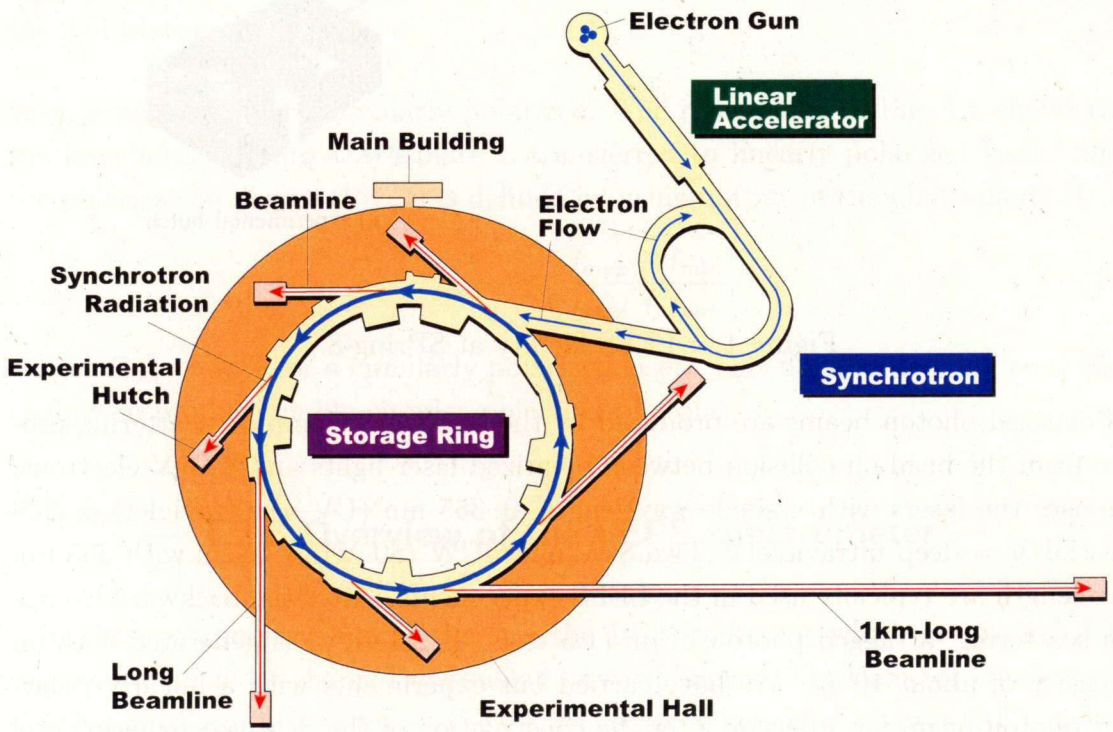

Figure 1.4: Schematic of view of SPring-8.

of an injector linear accelerator, a booster synchrotron and a low emittance storage ring. The linear accelerator accelerates electrons to energy of 1 GeV. The accelerated electron beam is transported to the synchrotron, which boosts up its energy to 8 GeV. 8 GeV electrons are injected into the storage ring, and are stored with an

energy of 8 GeV.

— 1.2.2 Laser electron photon beam at SPring-8 —

We will use circularly polarized photon beams at E=1.5-2.4 GeV. We expect the tagged photon intensity of about 10^6 γ's/sec. Figure 1.5 shows the overall concept of the LEPS facility at SPring-8.

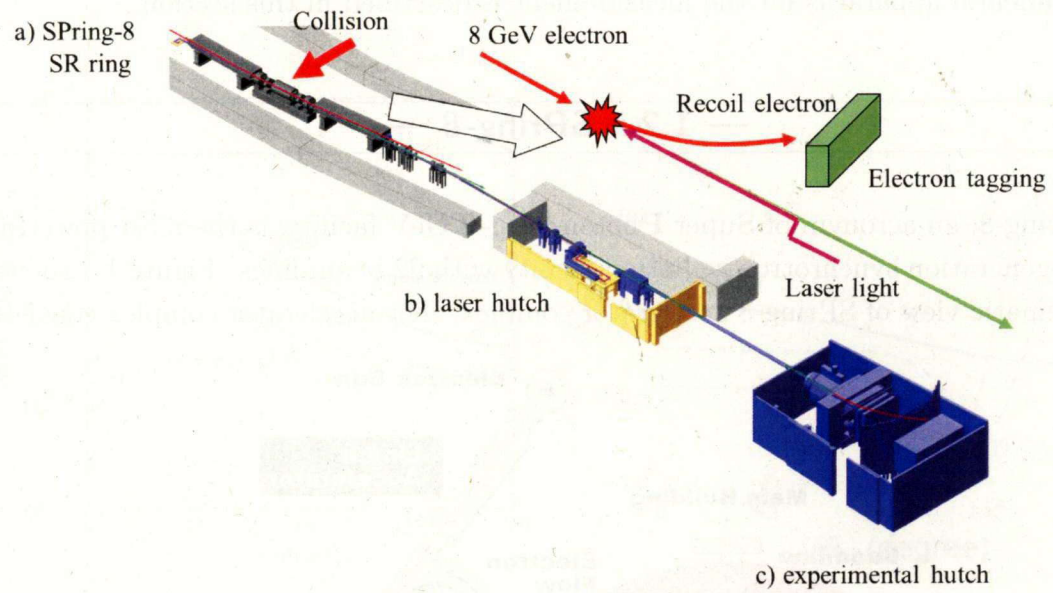

Figure 1.5: LEPS facility at SPring-8.

Polarized photon beams are produced by the backward Compton scattering process from the head-on collision between polarized laser lights and 8 GeV electrons. We uses the lasers with a single wavelength at 355 nm (UV = ultraviolet) or 266 nm (DUV = deep ultraviolet). Two 8-W quasi-CW (80 MHz) lasers with 355 nm wavelength are typically used in the LEPS experiments. After the backward Compton scattering, a tagged photon beam ($1.5 < E_\gamma < 2.4$ GeV) is generated with an intensity of about 10^6/s. We have carried out experiments with a linearly polarized photon beam for a decade after the construction of the SPring-8 experimental facility. A typical linear polarization degree of the injected laser is close to 100%, which produces a photon beam with a polarization degree higher than 90% at the maximum photon beam energy of 2.4 GeV.

Although the technique for obtaining the circularly polarized photon beam has not been completely established yet, the development itself was made once, and was arrived at the final stage. The polarization degree of the circularly polarized laser is measured after transferring to linearly polarized laser by using a $\lambda/4$ plate. Figure

1.6 shows the output of a photo-diode when a polarizer in front of the photo-diode is rotated. The flat distribution shown in the left panel in Fig. 1.6 indicates that the

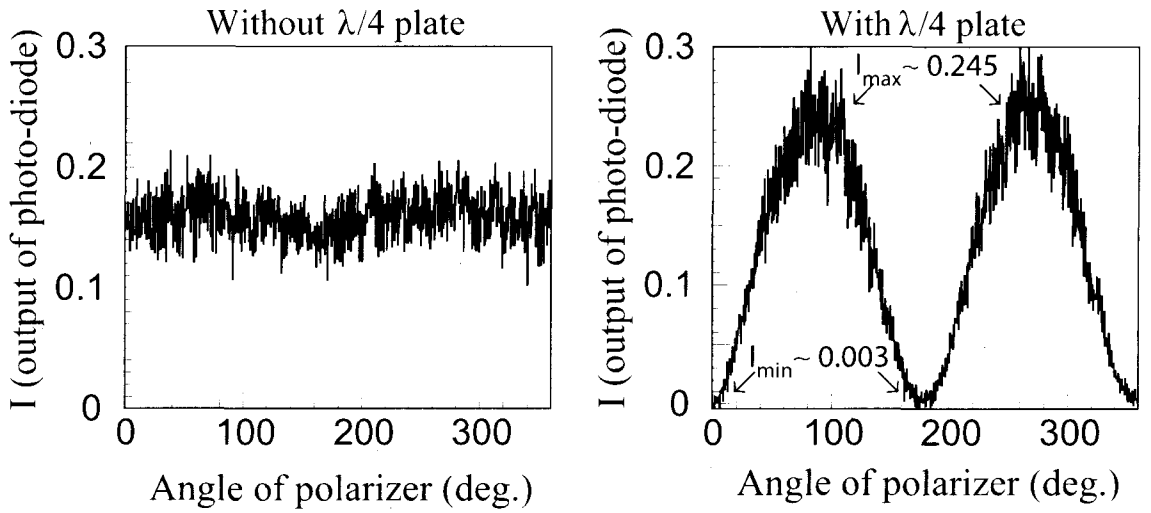

Figure 1.6: Output of the photo-diode when the polarizer is rotated. The left and right panels show the results of the photo-diode measurements without and with the $\lambda/4$ plate, respectively.

laser is unpolarized or circularly polarized. The right panel in Fig. 1.6 shows that the laser after passing a $\lambda/4$ plate is transferred to linearly polarized laser. Since the polarization degree (P_{laser}) is defined by using output of the photo-diode (I) as,

$$P_{laser} = \frac{I_{max} - I_{min}}{I_{max} + I_{min}}, \tag{1.2}$$

we get P_{laser} ~98% for a circularly polarized laser. This polarization degree is good enough to produce highly circular-polarized photons.

— 1.2.3 Overview of the LEPS spectrometer —

In the experimental hutch, there is the LEPS detector which is optimized for the measurement of charged mesons at forward angles. The detector consists of a plastic scintillator after a target (STC), an aerogel Cherenkov counter (AC), silicon-microstrip detector (SVTX), three drift chambers (DC1, DC2, and DC3), a dipole magnet, and time-of-flight (TOF) counters (Fig. 1.7). The opening of the dipole magnet is 135-cm wide × 55-cm high, and the length of the pole is 60 cm. The field strength at the center is 0.7 T. The trigger requires a tagging counter hit, charged particles after the target, and at least one hit of the TOF counters. Electrons, positrons, and high energy pions are vetoed by requiring no signal from the Cherenkov counter. In order to measure the momentum of charged particles, their

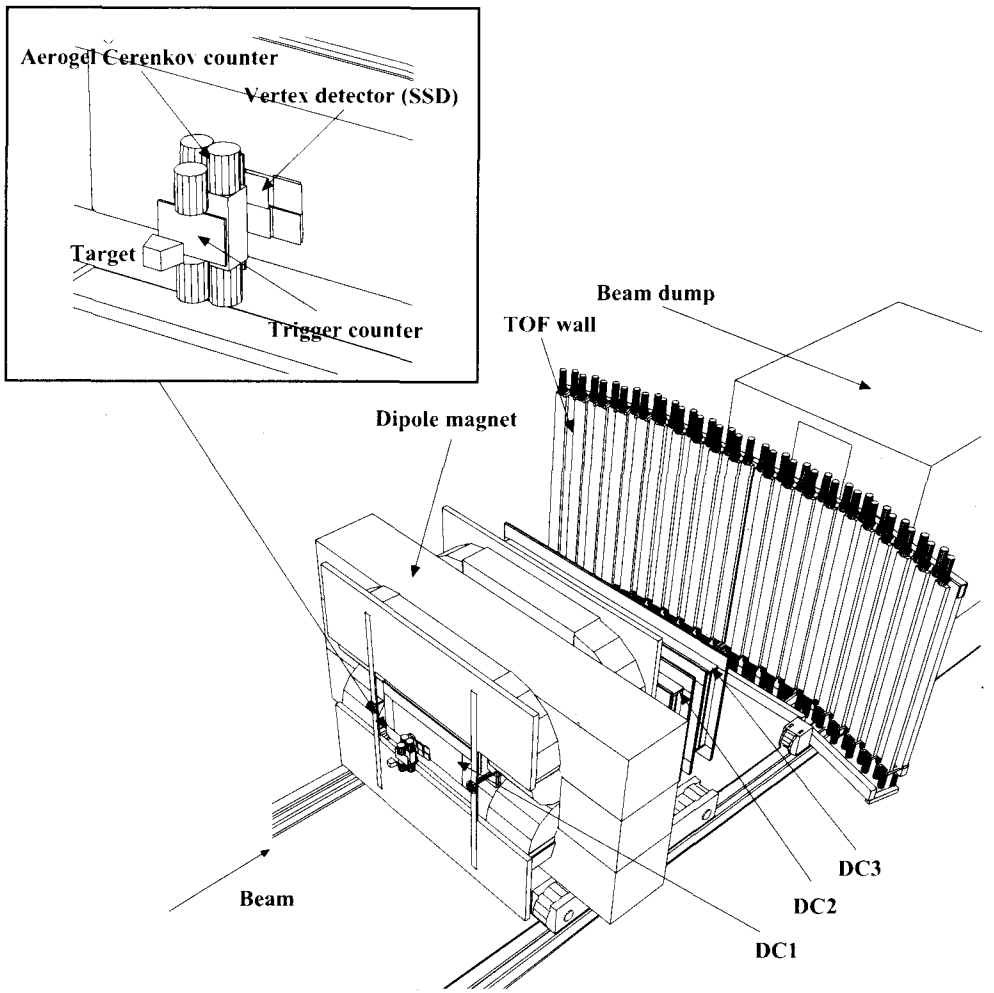

Figure 1.7: Top view of the LEPS detector in the experimental hutch. The photon beam is injected to the target from the left side. A typical event of K^+K^- pairs decaying from ϕ meson is illustrated. Charged particles are bent by the 30 ton dipole magnet and their trajectories are determined by the multiwire drift chambers (DC's) triggered with the STC and TOF counters.

trajectories are measured with the two planes of single-sided silicon-microstrip detectors and the six-plane multiwire drift chamber (MWDC) placed upstream of the dipole magnet, and two sets of five-plane MWDC's after the dipole magnet.

The angle coverage of the spectrometer is about ± 0.4 rad and ± 0.2 rad in the horizontal and vertical directions, respectively. The momentum resolution for 1-GeV/c particles is about 6 MeV/c.

Particle identification is performed by measuring the time of flight (TOF) of momentum-analyzed particles from the target to the TOF wall. A typical spectrum of the reconstructed mass is shown in Fig. 1.8. The mass resolution is about 30 MeV/c^2 for 1-GeV/c kaon. The first physics run with a liquid hydrogen target started in December 2000.

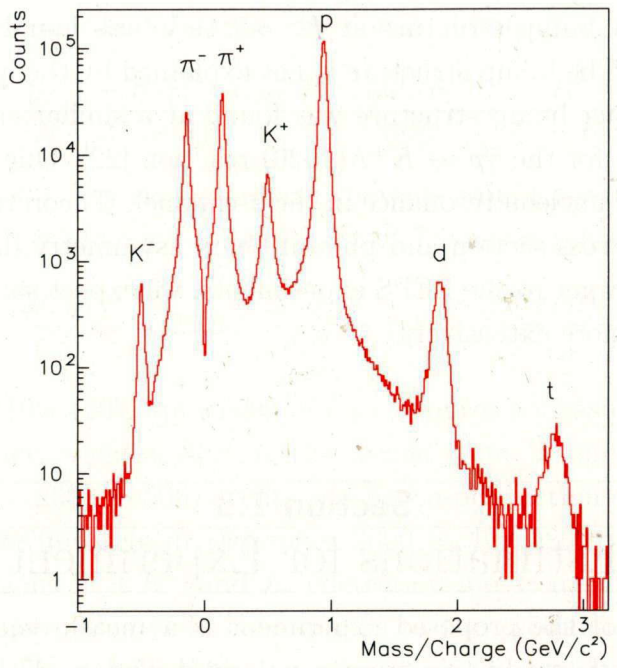

Figure 1.8: Reconstructed mass spectra. The histograms are mass of particles in the full momentum range.

The physics subjects of the LEPS experiments are summarized as follows,

(1) ϕ meson production:
$\vec{\gamma}p \to \phi p$ [10, 11], $\vec{\gamma}d \to \phi d$ [11, 12], $\vec{\gamma}d \to \phi pn$ [13], and
$\gamma A \to \phi X$ [14] reactions,

(2) Strangeness production:
$\vec{\gamma}p \to K^+\Lambda$ [15, 16, 17], $\vec{\gamma}p \to K^+\Sigma^0$ [15, 16, 18],
$\vec{\gamma}n \to K^+\Sigma^-$ [18], $\gamma p \to K^+\Sigma^0(1385)$ [19],
$\vec{\gamma}n \to K^+\Sigma^-(1385)$ [20], $\gamma p \to K^+\Lambda(1405)$ [19], and $\vec{\gamma}p \to K^+\Lambda(1520)$ [21, 22]
reactions,

(3) Pseudo scalar meson production:
$\vec{\gamma}p \to \pi^0 p$ [23] and $\vec{\gamma}p \to \eta p$ [24] reactions,

(4) Exotic baryon resonance search:
$\gamma n \to K^- X$ reaction [25, 26].

The ϕ meson photoproduction is dominated by the diffractive production within the vector-meson-dominance model through Pomeron exchange. Meson exchanges are suppressed by the OZI rule in the t-channel. The Pomeron exchange, $s\bar{s}$-knockout, and other reaction mechanisms are studied in the ϕ meson photoproduction. When the polarized photon beams and the polarized target are used, the $s\bar{s}$-knockout process is clearly observed by measuring double spin polarization

asymmetries [9]. A bump structure at E_γ ~2 GeV was found in the differential cross sections [10]. The bump structure is not explained by the well-known reaction mechanisms. Another bump structure was found at a similar energy in the differential cross sections for the $\vec{\gamma}p \to K^+\Lambda(1520)$ reaction [22]. One explanation of the bump structure is a nucleon resonance in the s-channel. Theoretical calculations do not reproduce the cross section and photon beam asymmetry data. Introducing a polarized nucleon target to the LEPS experiments, we expect such bump structures to be investigated more extensively.

Section 1.3

Estimations for Experiment

A main subject of the proposed experiment is a measurement of beam-target asymmetry of ϕ photoproduction from a polarized proton [27]. The beam-target asymmetry (C_{BT}) is calculated by Eq.1.1. Here we replaced $d\sigma(\overrightarrow{\rightarrow})$ and $d\sigma(\overleftarrow{\rightarrow})$ by $d\sigma_P$ and $d\sigma_A$. $d\sigma_P$ and $d\sigma_A$ represent the spin parallel and anti-parallel cross section from a HD target, respectively. $d\sigma_{BG}$ describes a common background contribution mainly caused from an unpolarized deuteron. Since three measurements of $d\sigma_P$, $d\sigma_A$ and $d\sigma_{BG}$ are independent, an error on the beam-target asymmetry (ΔC_{BT}) is written as

$$\begin{aligned}\frac{(\Delta C_{BT})^2}{C_{BT}^2} = & \frac{4(d\sigma_A - d\sigma_{BG})^2}{(d\sigma_P - d\sigma_A)^2(d\sigma_P + d\sigma_A - 2d\sigma_{BG})^2}(\Delta d\sigma_P)^2 + \\ & \frac{4(d\sigma_{BG} - d\sigma_P)^2}{(d\sigma_P - d\sigma_A)^2(d\sigma_P + d\sigma_A - 2d\sigma_{BG})^2}(\Delta d\sigma_A)^2 + \\ & \frac{4}{(d\sigma_P + d\sigma_A - 2d\sigma_{BG})^2}(\Delta d\sigma_{BG})^2. \end{aligned} \tag{1.3}$$

We defined the ratio R as follows

$$R = \frac{d\sigma_{BG}}{(d\sigma_P + d\sigma_A)/2}. \tag{1.4}$$

Using the background cross section $d\sigma_{BG}$ and an averaged cross section $(d\sigma_P + d\sigma_A)/2$, we obtain a relation between $d\sigma_P$ and $d\sigma_A$ as

$$d\sigma_A = \frac{1 - C_{BT}(1-R)}{1 + C_{BT}(1-R)} d\sigma_P. \tag{1.5}$$

If it is assumed that $d\sigma_P$ and $d\sigma_A$ are measured with the same precision, $\Delta d\sigma_A$ is written as

$$\frac{1 - C_{BT}(1-R)}{1 + C_{BT}(1-R)} \cdot \Delta d\sigma_P. \tag{1.6}$$

By using these relations, the following equation is obtained:

$$\frac{(\Delta C_{BT})^2}{C_{BT}^2} = \frac{\{1 - C_{BT}^2(1-R)\}^2 + C_{BT}^2 R^2}{2C_{BT}^2(1-R)^2} \cdot \frac{(\Delta \mathrm{d}\sigma_P)^2}{\mathrm{d}\sigma_P^2} + \frac{R^2}{(1-R)^2} \cdot \frac{(\Delta \mathrm{d}\sigma_{BG})^2}{\mathrm{d}\sigma_{BG}^2}. \quad (1.7)$$

Titov suggested that 1% of strange quark contents would produce $C_{BT} \sim 0.3$ in a small $|t|$ region. If R is assumed to be 0.5, Eq. 1.7 is rewritten as

$$\frac{(\Delta C_{BT})^2}{C_{BT}^2} = 20.8 \cdot \frac{(\Delta \mathrm{d}\sigma_P)^2}{\mathrm{d}\sigma_P^2} + 1.0 \cdot \frac{(\Delta \mathrm{d}\sigma_{BG})^2}{\mathrm{d}\sigma_{BG}^2}. \quad (1.8)$$

This means that 10% (20%) precision of C_{BT} requires a measurement of $\mathrm{d}\sigma_P$ with 2.2% (4.4%) accuracy, when neglecting the second term. If only statistical error is taken into account, ~2000 (~500) events of ϕ photo-productions has to be collected.

In the LEPS experiment from December 2000 to June 2001, about 3000 events of ϕ photo-productions in a K^+ and K^- detection mode are identified by using a 5 cm-long LH_2 target. This yield corresponds to the production rate per photon of $\sim 1 \times 10^{-9}$. About a half of the events are clarified to belong to the region of $t > -0.2$. Assuming a 5 cm-long HD target, $R = 0.5$ and 2×10^6 photons per second, ~70 events of ϕ productions would be collected for $t > -0.2$ in one day. A collection of 2000 × 2 events (500 × 2 events), which corresponds to the 10% (20%) accuracy measurement for C_{BT}, would be achievable in the 60 days (15 days) run time. Fig. 1.9 shows an expected precision of a beam-target asymmetry measurement as a function of the experimental period. The beam time with 15-60 days will be achievable with present technologies for the HD target.

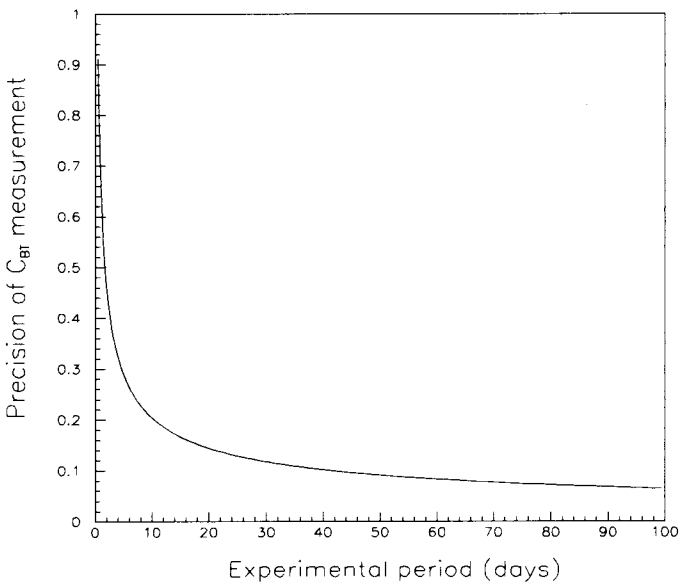

Figure 1.9: Expected precision for the beam-target asymmetry measurement as a function of the experimental period.

Section 1.4

Demand of polarized HD targets

Heteronuclear Hydrogen molecules like HD are polarized, and have interesting properties. The proton with a spin 1/2 and the deuteron with a spin 1 are independently polarized, and are independently reversible. In HD, H and D vector polarizations, exceeding 85% and 25%, respectively, are attainable by using the present low-temperature and high-magnetic-field technology. Solid polarized HD samples are kept in the frozen-spin conditions at the temperature below 4 K and at the moderate holding field of 0.5 T, allowing easy transportation. Therefore, the polarization production site is separated from the experimental one [28]. For nuclear physics experiments, thick targets of several moles (20 cm^3/mole) can be produced, making it possible to use them with low-intensity real-photon beams [29]. Honig first expects the relaxation time much longer than a month for H and D at 0.5 K [30].

High polarizations of proton and deuteron targets are achieved by the static method using "brute force" to polarize the protons in HD at low temperature (15 mK) and high field (17 T), and when the adiabatic fast passage technique is applied to transfer proton's polarization to the deuterons, we are able to get higher polarization for deuteron than that of static method only.

During 5 years, we have carried out a variety of tests for the cryogenic devices and for the development of the NMR system. The demands of a polarized HD target are as follows:

- There is little impurity matter which acts as background in the HD target.
- A high polarization is kept for over three months.
- H nucleus and D nucleus are enable to be polarized, separately.

Chapter 2

Polarized HD target

An HD ice is used to produce a polarized target for measuring double polarization observables in the ϕ meson photoproduction. The HD target does not include any heavier elements, such as C and N. Therefore, it is possible for us to observe photoreactions with a small cross section. The HD molecule can be used as a polarized target both for protons and neutrons. Thin aluminum wires (20% in weight) must be contained in the target cell to enhance the heat conductivity for cooling. In order to achieve high polarizations of proton and deuteron in the HD target, we employ the static method ("brute force" method) at low temperature (10 mK) and at high magnetic field (17 T). The polarized HD target has a unique property with a long relaxation time at low temperature. The relaxation time depends on the residual amounts of ortho-H_2 and para-D_2 in the HD gas. The polarized HD target enables us to measure the complete polarization observables in combination with the polarized γ-ray beam at SPring-8.

— 2.0.1 History of polarized HD targets. —

The frozen-spin molecular HD target was proposed at first in 1967 [31]. Its original idea is backdated to 1957. Honig first suggested that the proton polarization in a solid HD target is able to be explained on the basis of the experimental observation of relaxation times influenced with ortho-hydrogen impurities [32]. In order to polarize protons in the frozen HD target, Honig applied the innovative idea that the HD polarization gradually grows up in the spin-flip process between HD molecules and a small amount of ortho-H_2 with spin 1 by making use of the mechanism originally clarified in earlier years by Motizuki *et al.* [33, 34]. In Table 1, we list the milestone events for the remarkable developments associated with the HD target. Thanks to longstanding efforts at Syracuse [35, 36], BNL [37, 38, 39], and ORSAY [40, 41, 42, 43, 44], the HD target has been firstly used for the actual experiment at LEGS [45], and will be used both at JLab [46] and at SPring-8 [47, 48, 49, 50, 51, 52, 53] in near future. Although there are still many remaining technical problems to improve the performance of the HD system.

Table 2.1: History of polarized HD targets.

1957	M. Bloom	An important relaxation mechanism for the protons in solid HD by using "impurity" ortho-H_2 molecules.
1966	W.N. Hardy and J.R. Gaines	The above relaxation mechanism with o-H_2 was confirmed by relaxation time measurements in very pure HD at 1.2 K $\sim$ 4.2 K $\rightarrow$ proton relaxation time of many hours was obtained by aging a solid HD with a small o-H_2 impurity.
1967	A. Honig	Proposal for a frozen-spin target: polarizing the HD at · high magnetic field (> 10 T) · low temperature (near 10 mK)
1968–1978 (1968–1978) (1971–1977)	 A. Honig, *et al.* H.M. Bozler, E.H. Graf, *et al.*	Study of the relaxation times, depending on temperature, magnetic field, ortho-H_2 and para-D_2 concentration. At Syracuse University · $T = 0.4 \sim 16$ K, $B = 0 \sim 1$ T At SUNY Stony Brook · $T = 35$ mK ~ 4 K, $B = 1.5 \sim 10$ T
1975	H. Mano and A. Honig	Radiation damage was studied at BNL 28 GeV proton synchrotron and Cornell 10.4 GeV electron synchrotron.
1976	A. Honig and H. Mano	RF forbidden transition AFP (Adiabatic Fast Passage) Proton $\Leftrightarrow$ deuteron polarization transfer.
1983–late 1980s	A. Honig, *et al.*	The first application of polarized HD (produced at Syracuse for fusion study).
1991	N. Alexander, *et al.*	Invention of cold-transport devices for moving HD from production site to experimental site.
2001.11	LEGS collaboration	The first double-polarization data of meson photoproduction with polarized HD target

— 2.0.2 Outline of the polarized HD target —

We will here outline the principle of polarized HD target in an intuitive way. The basic symmetry condition imposed on the total wave functions of H_2 (two fermions) and D_2 (two bosons) gives a restriction on the possible nuclear spin orientation at low temperature. In case of H_2, the ortho state (o-H_2) has a nuclear spin S=1 and a molecular orbital angular momentum of L=odd. Since the nuclear spins are aligned, the o-H_2 can be polarized. However, the equilibrium condition at low temperature requires the para-hydrogen state (p-H_2) with S=0 and L=0. Since the nuclear magnetic moments are anti-parallel, the para-hydrogen is not polarized. In case of D_2, it is the p-D_2 combination (S=1;L=odd) that disappears at low temperature, leaving the o-D_2 (S=0,2;L=0). Although 5/6 of the nuclei in o-D_2 have a population with their spins parallel (S=2), the small magnetic moment of the deuteron makes static polarization of pure deuterium very difficult.

In contrast, the orbital and spin angular momenta of the heteronuclear molecules HD are not limited by symmetry requirements (one fermion and one boson). The HD becomes the ground state with the L=0 in the molecular rotation, irrespective of the relative orientation of the proton with a spin 1/2 and the deuteron with a spin 1 at low temperature. Since the spin-lattice coupling is primarily caused in the process of molecular rotations, the relaxation rates are extraordinary small. Although the long relaxation time is essential for using polarized targets in nuclear physics experiments, it makes the polarization phase equally long. This is a dilemma; we hope to prepare the polarized target in a relatively short time, and like to keep the produced polarized target for a long time in experiments. For the polarization of HD, the answer to solve this dilemma was suggested by Honig [31].

The relaxation (polarization) time is reduced by introducing a small (approximately the order of 10^{-4}) contamination of o-H_2 and p-D_2, as an impurity. The presence of o-H_2 and p-D_2 plays an important role to polarize the target. The molecular orbital angular momentum couples with both the lattice and the nuclear spin. Thus, by doping small amounts of o-H_2 and p-D_2 into the pure HD, the relaxation times of the H and D in HD are reduced so that the HD target is polarized. The equilibrium polarizations of 80% for H and 20% (vector) for D can be achieved in this way for HD cooled to ~14 mK in a dilution refrigerator at the magnetic field of 17 T. The HD target must be kept at this low temperature under the magnet field of 17 T for a long time to let the impurities o-H_2 and p-D_2 decay to their magnetically-inert ground states, so that the sample spins are effectively"frozen".

— 2.0.3 Benefits of polarized HD target —

Molecular H_2 has two states, o-H_2 and p-H_2. H_2 contains two protons, which are indistinguishable Fermi particles. The wave function of the two protons should be an antisymmetric. Thus, the spin directions of the two protons must be opposite, or the angular momentum between the protons must be in an odd-L state. Normal hydrogen reaches at the statistical equilibrium of ortho and para-H_2 at high temperature. The ratio of statistical population is 3:1 for o-H_2 and p-H_2 (3/4 ortho and 1/4 para). When hydrogen is liquid or solid at low temperature, the odd-L states quickly decay to L=1, and the even-L states quickly decay to L=0, preserving the ortho/para quantities. The ortho molecules decay to the ground state of hydrogen, para-H_2 with time constant of 6.4 day. Thus, H_2 quickly loses the ability to be polarized. Molecular deuterium has the same issue because the p-D_2 (L=1) decays to o- D_2 (L=0) at low temperature. Hydrogen deuteride (HD) is made of two distinguishable nuclei. The ground state is L=0. The spins of both the proton and deuteron are possible to be aligned with the external magnetic field.

— 2.0.4 Dilution factor —

Dilution factors used as a polarized target shown in Table 2.2. The dilution factor is an indication which is amounts of polarizable nuclei as a target in the material. The materials are polarized by dynamic nuclear polarization (DNP) method except for HD. Since HD only consists of hydrogen and deuteron, the dilution factor of both of hydrogen and deuteron as the target nucleus is high.

Section 2.1
Polarization principle

— 2.1.1 Interaction energy coupled with magnetic field —

The important properties of a nucleus with a spin are magnetic moment $\boldsymbol{\mu}$ and an angular momentum $\boldsymbol{J}$. These two vectors is related as,

$$\boldsymbol{\mu} = \gamma \boldsymbol{J} \tag{2.1}$$

Table 2.2: Dilution factor of target materials used as a polarizing target [54]. Since ^{6}LiD is considered to consists of one α cluster and two deuteron, the dilution dactor of ^{6}LiD is evaluated 0.5.

	Polarization method	Maximum polarization	Dilution factor of hydrogen
C_4H_9OH	DNP	93	13.5
NH_3	DNP	97	17.5
HD	Brute force	94	33.3

	Polarization method	Maximum polarization	Dilution factor of deuteron
C_4H_9OD	DNP	93	23.8
ND_3	DNP	97	30.0
^{6}LiD	DNP	97	50.0
HD	Brute force	94	66.6

where γ is a scalar quality called the "gyro-magnetic ratio". The angular momentum $\boldsymbol{J}$ is related to a dimensionless angular momentum operator $\boldsymbol{I}$ by the equation:

$$\boldsymbol{J} = \hbar \boldsymbol{I} \tag{2.2}$$

$\boldsymbol{I}^2$ has an eigen value $I(I+1)$ where I is either integer or half-integer ($I = 1/2, 1, 3/2, \ldots$). Any component of $\boldsymbol{I}$ (for example I_z) commutes with I^2. We may specify simultaneously eigenvalues of both I^2 and the sub-state m, respectively. The m is one of the $2I + 1$ values I, $I - 1$, $\ldots$ $-I$

When a magnetic field $\boldsymbol{H}$ is applied to a nucleus, an interaction energy of the nucleus, the interaction Hamiltonian is given as

$$\mathcal{H} = -\boldsymbol{\mu} \cdot \boldsymbol{H}. \tag{2.3}$$

Taking the applied magnetic field to be H_0 along the z-direction, we find

$$\mathcal{H} = -\gamma \hbar H_0 I_z. \tag{2.4}$$

The eigen values of this Hamiltonian are simple, being only multiples ($\gamma \hbar H_0$) of the eigen values of I_z. Therefore, the allowed energies are

$$E = -\gamma \hbar H_0 m \qquad m = I, I - 1, \ldots - I \tag{2.5}$$

— 2.1.2 Boltzman distribution —

At a temperature T and under the magnetic field H_0, the polarization can be calculated by Boltzmann distribution of nuclear system. Using Boltzmann distribution, the probability $P(E_j)$ is given as

$$P(E_j) = \frac{exp(-E_j/kT)}{\sum_{i=0}^{\infty} exp(-E_i/kT)}. \tag{2.6}$$

The number of nuclei $n(E_j)$ with an energy E_j is written as

$$n(E_j) = N\frac{exp(-E_j/kT)}{\sum_{i=0}^{\infty} exp(-E_i/kT)}. \tag{2.7}$$

The summation over all energies is N

In the case of $I = 1/2$, we have two eigen values of I_z, $1/2$ and $-1/2$. Therefore, there are two energy levels (see Fig. 2.1),

$$\Delta E = E_{-1/2} - E_{1/2} = 1/2\gamma\hbar H_0 - (-1/2\gamma\hbar H_0) = \gamma\hbar H_0 \tag{2.8}$$

— 2.1.3 Theoretical polarization —

On the basis of the Boltzmann law, the polarization relates only to the magnetic field and temperature, as shown in the following equation

$$n_{1/2} = Nexp(\frac{\Delta E}{k_B T}); \quad n_{-1/2} = Nexp(\frac{-\Delta E}{k_B T}) \tag{2.9}$$

Taking the Eq. 2.8 and 2.9 into account, we can get the proton polarization as

$$P_H = \frac{n_+ - n_-}{n_+ + n_-} = \frac{exp(\frac{\Delta E}{k_B T}) - exp(\frac{-\Delta E}{k_B T})}{exp(\frac{\Delta E}{k_B T}) + exp(\frac{-\Delta E}{k_B T})} = \tanh(\frac{\Delta E}{k_B T}) = \tanh(\frac{\gamma_h \hbar H_0}{k_B T}) \tag{2.10}$$

In the case of $I = 1$ for deuteron, we have three eigen values of $I_z = -1$, 0 and 1. Therefore, there are three energy levels,

$$E_1 = -\gamma_d \hbar H_0, \quad E_0 = 0 \ \ and \ \ E_{-1} = \gamma_d \hbar H_0 \tag{2.11}$$

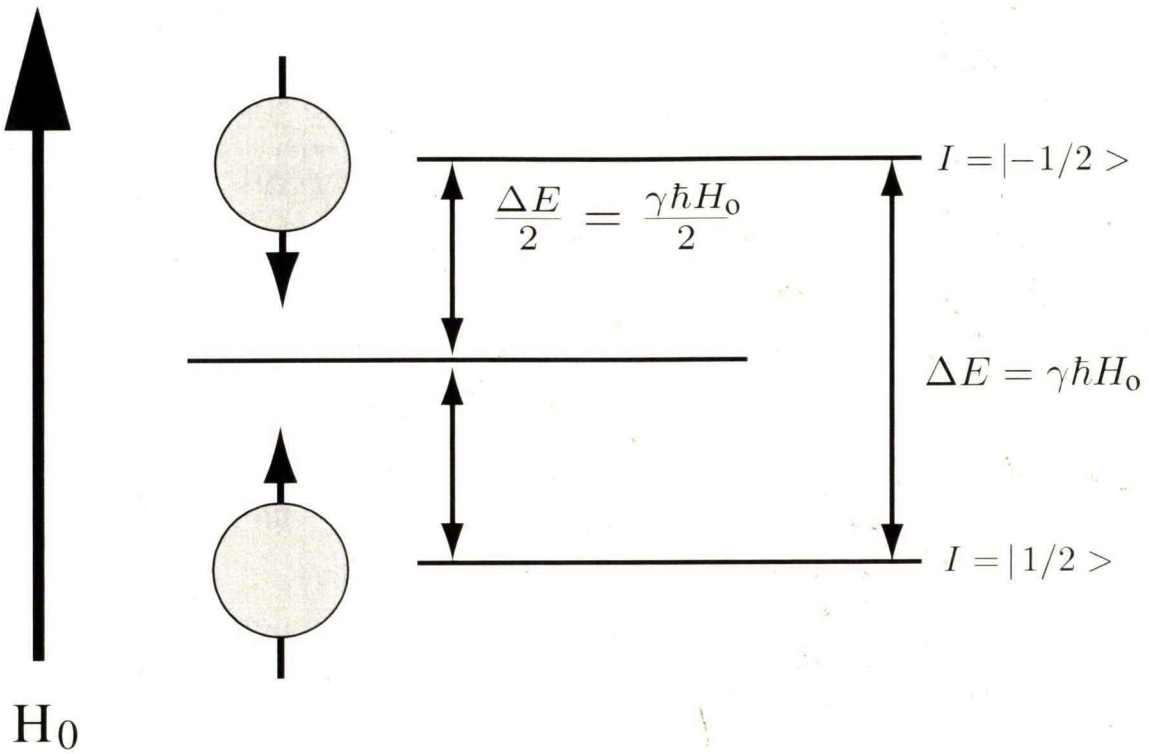

Figure 2.1: Energy levels of proton.

Number of nuclei n_j in three energy levels are

$$E_1 = -\gamma_d \hbar H_0, \quad E_0 = 0 \ \ and \ \ E_{-1} = \gamma_d \hbar H_0 \tag{2.12}$$

The polarization of deuteron is given by

$$P_D = \frac{n_1 - n_{-1}}{n_1 + n_0 + n_{-1}} = \frac{4\tanh(\frac{\gamma_d \hbar H_0}{k_B T})}{3 + \tanh^2(\frac{\gamma_d \hbar H_0}{k_B T})} \tag{2.13}$$

Since the calculation for the D polarization is a little bit complex, we give the detailed equation to obtain the final equation of P_D. We replace $\Delta E/k_B T$ to x.

$$
\begin{aligned}
P_D = \frac{n_1 - n_{-1}}{n_1 + n_0 + n_{-1}} &= \frac{e^x + e^{-x}}{e^x + e^0 + e^{-x}} \\
&= \frac{(e^{x/2} + e^{-x/2})(e^{x/2} - e^{-x/2})}{e^x + e^0 + e^{-x}} \\
&= \frac{\dfrac{(e^{x/2} + e^{-x/2})(e^{x/2} - e^{-x/2})}{(e^{x/2} + e^{-x/2})^2}}{\dfrac{e^x + e^0 + e^{-x}}{(e^{x/2} + e^{-x/2})^2}} \\
&= \frac{4\dfrac{(e^{x/2} + e^{-x/2})}{(e^{x/2} + e^{-x/2})}}{\dfrac{4(e^x + e^0 + e^{-x})}{(e^{x/2} + e^{-x/2})^2}} \\
&= \frac{4\dfrac{(e^{x/2} + e^{-x/2})}{(e^{x/2} + e^{-x/2})}}{\dfrac{3e^x + 6e^0 + 3e^{-x} + e^x - 2e^0 + e^{-x})}{(e^{x/2} + e^{-x/2})^2}} \\
&= \frac{4\dfrac{(e^{x/2} + e^{-x/2})}{(e^{x/2} + e^{-x/2})}}{\dfrac{3(e^{x/2} + e^{-x/2})^2 + (e^x - e^{-x})^2}{(e^{x/2} + e^{-x/2})^2}} \\
&= \frac{4\tanh(x)}{3 + \tanh^2(x)}
\end{aligned}
$$

Table 2.3: Polarizations of H and D calculated with the Boltzmann raw.

	Hydrogen	Deuteron
μ/μ_N	2.79	0.857
H_0	17 T	17 T
Temperature	P_H	P_D
300 K	0.006%	0.001%
273 K	0.006%	0.001%
77 K	0.023%	0.005%
4.2 K	0.414%	0.085%
1.0 K	1.737%	0.355%
100 mK	17.196%	3.553%
14 mK	84.563%	24.797%
6 mK	99.390%	52.582%

Using the aforementioned equation, we can estimate the polarization in the ther-

mal equilibrium state. In the thermal equilibrium state at H_0=17 T and T=14 mK, the H and D polarization reaches 85%, and 25%, respectively as shown in Fig. 2.2.

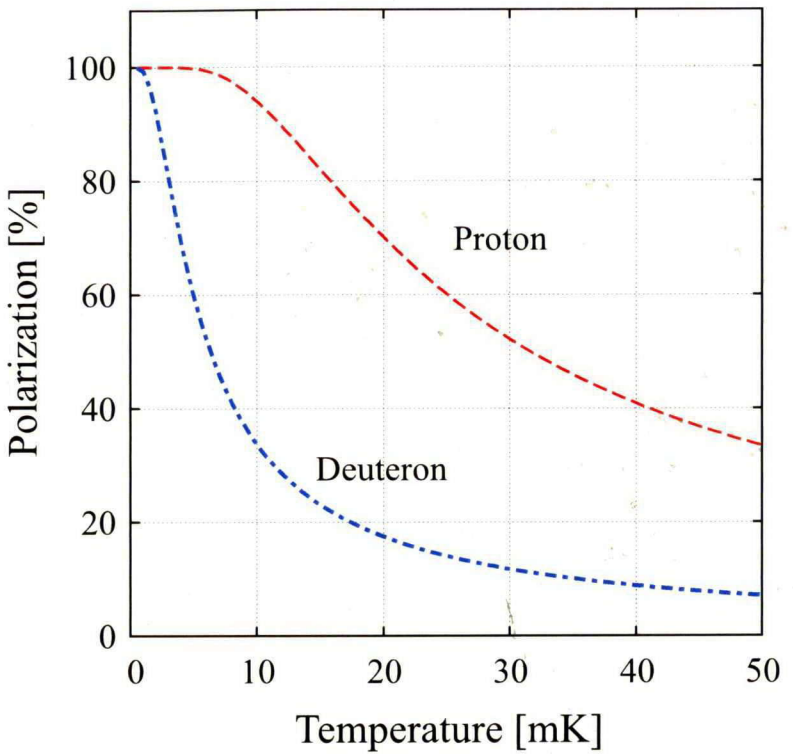

Figure 2.2: The polarizations P_H and P_D estimated by using Eq. 2.10 and Eq. 2.13. The P_H and the P_D are 84.5% and 24.8% at 14 mK and 17 Tesla, respectively.

Section 2.2
Production method of polarized HD target

— 2.2.1 Polarization method —

Heteronuclear diatomic molecule like HD is polarized, and has some interesting properties. The proton with a spin 1/2 and the deuteron with a spin 1 are independently polarized, and are independently reversible.

As mentioned in Section 2.0.2, we can obtain a polarized target at low temperature and under the high magnetic field with a small mixture of o-H_2 and p-D_2. Figure 2.3 shows a schematic view of the polarization process making the HD target. The equilibrium condition at low temperature requires the p-H_2 state with S=0 and L=0. The presence of o-H_2 and p-D_2 in the HD plays an important role to polarize

the target. The molecular orbital angular momentum couples with both the lattice and the nuclear spin. Thus, by doping small amounts of o-H_2 and p-D_2 into the pure HD, the relaxation times of the H and D in HD are reduced so that the sample can be quickly polarized. Therefore, by introducing a small (approximately the order of 10^{-4}) contamination of o-H_2 and p-D_2, as an impurity, we can shorten the relaxation time.

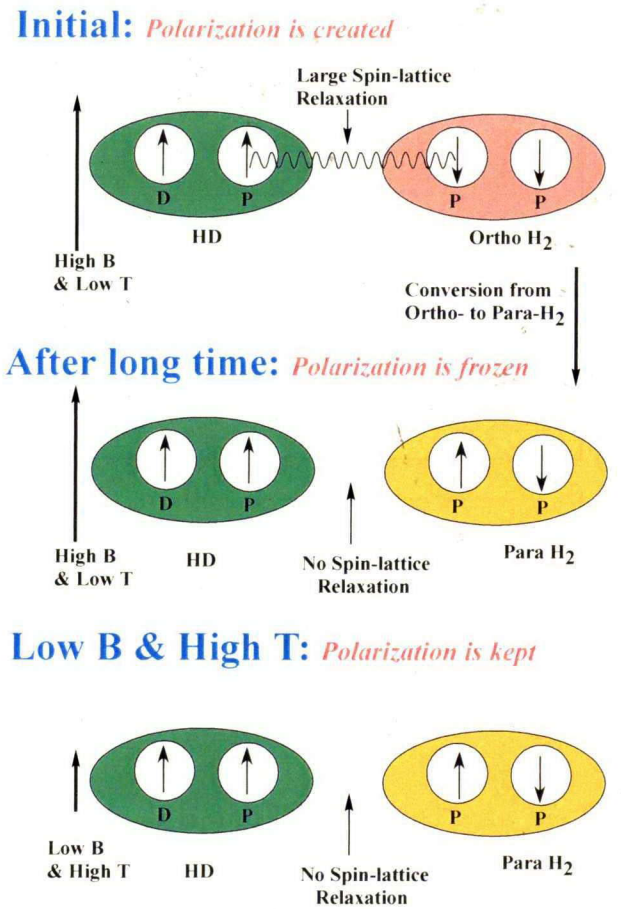

Figure 2.3: An intuitive picture showing a principle of HD target

The equilibrium polarizations are achieved to be 85% for H and 25% for D at 14 mK under the magnetic field of 17 T. The HD sample must be kept under this conditions long enough to let the impurities o-H_2 and p-D_2 decay to their magnetically-inert ground states, so that the sample spins are effectively frozen. In view of the corresponding decay time constants, this aging process is very long. Unfortunately, the D polarization is only 25%. Therefore, in the practical cycle which has been applied to polarize HD, only o-H_2 doping has been used to polarize H. The D polarization has been obtained by transferring the H polarization to the D, using a method commonly known as "Adiabatic Fast Passage (AFP)" [55]. This technique takes advantage of the dipole coupling of H and D nuclei in different HD molecules. In this way, the polarization of deuteron reaches 60% [30, 56].

— 2.2.2 Frozen-spin mode —

A unique property of pure HD is the long relaxation time of polarization at low temperature. The o-H_2 decays to the p-H_2 at low temperature, and becomes unpolarizable. We manipulate this feature of HD [55]. The spin-lattice relaxation time, T_1, is defined as the lifetime in an exponential decay (or growth) of polarization. By developing a method to change the spin-lattice relaxation times (T_1, corresponding to the polarization lifetime of the proton, and T_1^D, corresponding to the polarization lifetime of the deuteron), one can polarize a target with a short time, and can transfer it to a lower field and higher temperature environment where it still has a long T_1. Figure 2.4 shows the explanation drawing of the frozen-spin mechanism. The polarization of the HD target grows to that of thermal equilibrium. The relaxation time of the HD target becomes longer with decreasing the o-H_2 by hydrogen ortho-para conversion . The growing rate of the polarization of the HD slows down with prolonging the relaxation time. This frozen-spin is a key feature of the polarized HD system. This mechanism is well accomplished by introducing a small fraction ($\sim 10^{-4}$) of the o-H_2 impurity for the proton and a small amount of the p-D_2 impurity for the deuteron. This impurity is polarizable and cross-relaxes with the corresponding nucleus of HD. In the case of the proton, by introducing a small amount of o-H_2, we can shorten T_1 in polarizing HD, and allow the proton to be polarized by the conventional "brute force" method at low temperature and high magnetic field. Similarly, by putting a small amount of the p-D_2 in HD, we can shorten T_1^D (the deuteron is a spin 1 particle and p-D_2 with L=1 is dominated at low temperature and decays to the o-D_2 state with L=0). Unfortunately, the reality is even more complicated, because amounts of H_2 shortens T_1^D and vice versa. In pure H_2 at a temperature of 4 K and below, the existing o-H_2 decays to the p-H_2 with a rate of about 15% per day. In pure H_2, this means that the amount of magnetically active hydrogen decreases soon. For the o-H_2 impurity in HD, the decay lifetime is not the same. But it still decays with an exponential function of time. As the o-H_2 in HD converts to the p-H_2 , T_1 grows longer and this process is referred as aging. The aging of the target contributes to highly polarize the HD target with a long T_1 and T_1^D (frozen-spin). This is a tremendous advantage of the polarized HD target. When the HD is at room temperature, the ortho- and para- species back-convert to equilibrium populations. A frozen-spin highly polarized target can be transported or stored in a relatively low magnetic field and at a temperature of a few K. This means a frozen-spin target may be placed in a in-beam cryostat with a small magnet for a holding field and with less massive thermal radiation shields to keep it cold. This allows us to perform an experiment under the condition of a low particle energy loss, likely photoreactions, since the target is not heated up, and we

can obtain a good statistics from a high polarization.

— 2.2.3 Drawbacks of the polarized HD target system —

There is no research program without any difficulty. The polarized HD target is not exceptional. A polarized HD target cannot be used in a hadron beam inducing high ionization. A hadron beam knocks many electrons out of the HD crystal lattice, and allows an unexpected spin-relaxation mechanism through the spin exchange process between electrons and protons in the HD. This effect degrades the polarization of the target by shortening T_1 which causes the high polarization to diminish. A hadron beam of non-ionizing radiation with a high amount of ionizing radiation impurity will reduce the useful life time of the polarized target in beam. These limitations make the HD target inappropriate for using a beam of electrically charged particles. If a frozen-spin polarized target is not in a magnetic holding field at all times, T_1 and T_1^D are shortened to be less than seconds. This produces a frozen-spin unpolarized HD target useless for a double-polarization experiment, and the three months for aging the target are wasted. Care must be taken to ensure that the target does not encounter a near-zero magnetic field region.

— 2.2.4 Target cell —

The target cell is designed for transporting the solid HD. Figure 2.5 shows the photographs of the cell for the polarized HD target. The main components of the target cell are PCTFE (Kel-F). The target cell consists of the copper screw ring, aluminum cooling wires and the PCTFE end-caps. The copper screw ring is used to connect the cold finger of the DRS, and is fabricated with sufficient high-purity copper material to provide a good thermal conductivity in the mK region of temperature. The target should be non-magnetic so that it does not interfere with the NMR line-shape. The aluminum cooling wires are 50 μm in diameter and 99.999% purity. They are bundled and attached to the target ring. There are approximately 2000 such cooling wires in the target cell. The total mass of the aluminum wires is about 20% of the mass of the HD target material.

The PCTFE cell and end-caps dose not contain any atomic hydrogen, in order to avoid the additional background for the NMR measurements. The majority of the nuclear background comes from PCTFE material so that the parts of the end-caps which will be in the beam are made as thin as possible. The top cap is necessary to reduce the size of hole open to vacuum (or He exchange gas) so that the amount of HD which sublimates from the solid target is negligible. [57].

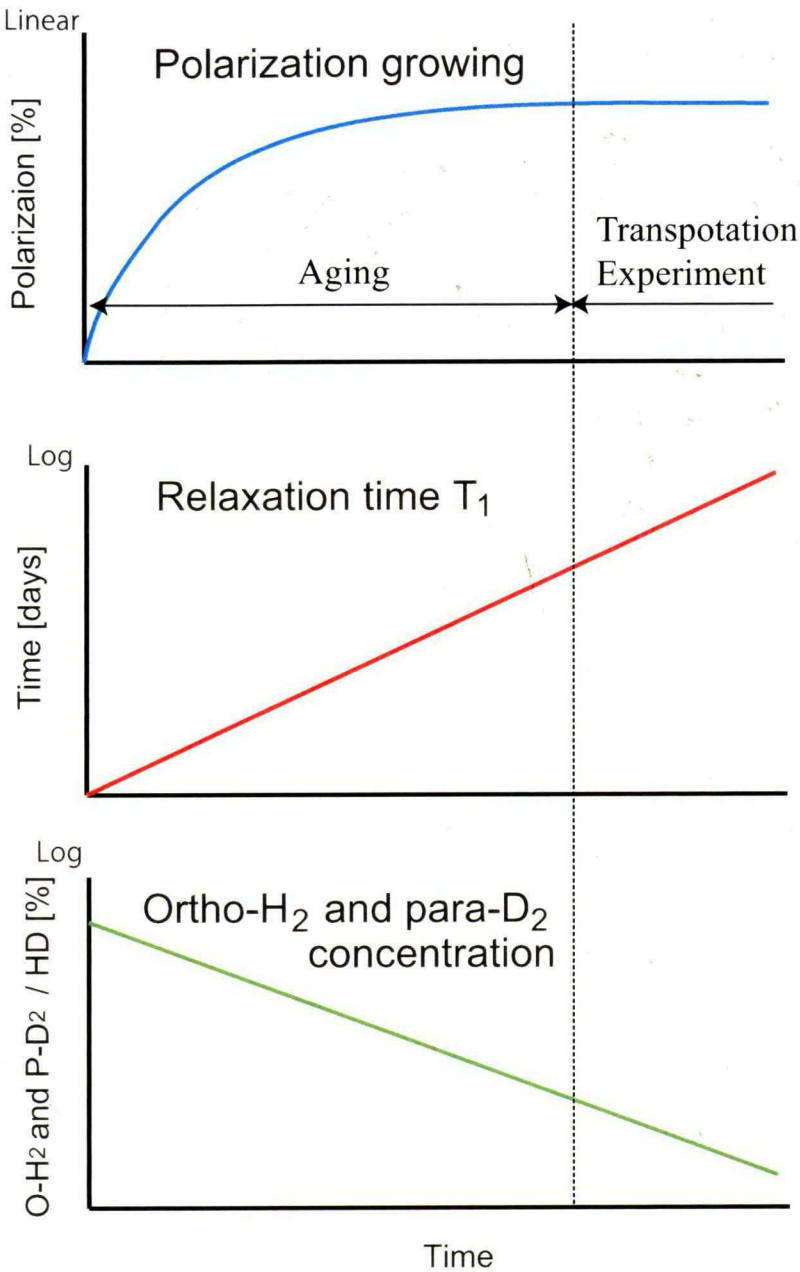

Figure 2.4: A model of frozen spin mechanism with elapsed day. The panels shows variances of the polarization, relaxation time and o-H_2 concentration in HD with elapsed day.

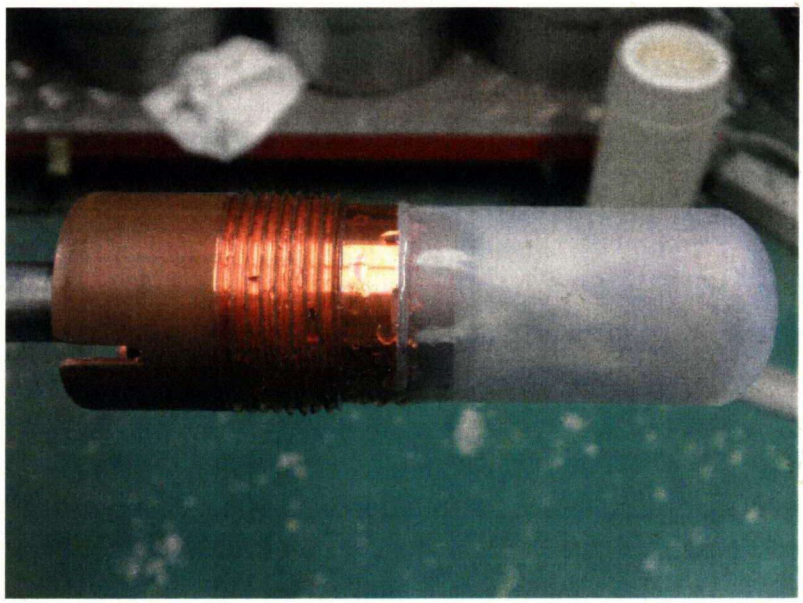

Figure 2.5: Photograph of target cell

Section 2.3

Polarization measurement

We try to obtain the nuclear polarization of solid HD at low temperature and in a high magnetic field. The HD sample is paramagnetic substance. The relation between the magnetization and applied magnetic field obeys the famous Curry's law, in which the magnetization is proportional to the applied magnetic field, and the proportional constant is called "(static) susceptibility". In the case of electron systems, it is not so difficult to measure the magnetization of substances in static magnetic field because of existing a large enhancement factor in the system. Unfortunately, in case of nuclear systems, even if at low temperature below 1 mK in a high magnetic field higher than 1 T, we need to use the NMR technique. In addition to the external static magnetic field, a week oscillating magnetic field with near the resonance frequency (rf: radio frequency ω) of nucleus is applied to a sample substance by applying an alternating current to a tank circuit coil in which the sample substance is inserted. The static susceptibility is a response of the static magnetic field, like that, the complex susceptibility is yielded by the oscillating magnetic field which is expressed by a complex manner. Then, the complex susceptibility has a real part and an imaginary part. When the resonance occurs, we have an oscillating NMR signals. We can treat the signal as a complex expression, that is, absorption signals (inphase signals or real signals) and dispersion signals (quadrature signals or imaginary signals). The absorption signal is proportional to the imaginary part of the complex susceptibility and the dispersion signal is proportional to the real part. Therefore, we have two kinds of NMR signals which are described as a function

of ω. From theoretical considerations about the complex susceptibility, there are relations between the real and imaginary parts. By using these relations, we can obtain the static susceptibility of the sample. The area of absorption signals (the peak area in the spectrum) is proportional to an integration of the imaginary part of the complex susceptibility related to polarization and which is directly proportional to static susceptibility.

— 2.3.1 Magnetization —

When I is 1/2, the magnetization of the polarized target is

$$M(T, H_0) = \frac{1}{2}\gamma\hbar n_+ - \frac{1}{2}\gamma\hbar n_- = \frac{1}{2}\gamma\hbar N P_H(T, H_0) \tag{2.14}$$

A paramagnetic substance which has N nuclei in a unit volume can be magnetized by the static magnetic filed H_0. We have a magnetization $M(T, H_0)$ as

$$M(T, H_0) = \chi_0 H_0, \tag{2.15}$$

Where χ_0 is the static susceptibility of the substance in a unit volume. χ_0 for the proton can be written in terms of the polarization P_H as

$$\chi_0 = \frac{\gamma\hbar N}{2H_0} P_H(T, H_0) \tag{2.16}$$

This is called Langevin paramagnetic equation. Under high temperature approximation, $\tanh(\gamma\hbar H_0/2k_BT) \approx \gamma\hbar H_0/2k_BT$, we obtain

$$\chi_0 = \frac{\gamma\hbar N}{2H_0}\frac{\gamma\hbar H_0}{2k_BT} = \frac{1}{4}\frac{(\gamma\hbar)^2}{k_BT}N \tag{2.17}$$

This equation is the famous Curry's law. For deuteron with $I = 1$, the magnetization $M(T, H_0)$ is given as

$$M(T, H_0) = \gamma\hbar n_+ - \gamma\hbar n_- = \gamma\hbar N P_D(T, H_0). \tag{2.18}$$

In this case, χ_0 can be written by the polarization P_D as

$$\chi_0 = \frac{\gamma\hbar N}{H_0} P_D(T, H_0). \tag{2.19}$$

Under high temperature approximation, we obtain the following equation,

$$\frac{4\tanh(\gamma\hbar H_0/2k_BT)}{3 + \tanh(\gamma\hbar H_0/2k_BT)^2} \approx \frac{2}{3}\gamma\hbar H_0/2k_BT \tag{2.20}$$

Then we have

$$\chi_0 = \frac{1}{3}\frac{(\gamma\hbar)}{k_BT}. \tag{2.21}$$

— 2.3.2 Bloch equations —

When a rotating field H_1 with ω_z frequency is applied in the $x-y$ plane perpendicular to H_0, the Bloch equations in the rotating frame are written as

$$\begin{aligned}
\frac{dM_{z'}}{dt} &= -\gamma M_{y'} H_1 + \frac{M_0 - M_z}{T_1}, \\
\frac{dM_{x'}}{dt} &= +\gamma M_{y'} H_0' - \frac{M_{x'}}{T_2}, \\
\frac{dM_{y'}}{dt} &= +\gamma (M_{z'} H_1 - M_{x'} H_0') + \frac{M_y'}{T_2},
\end{aligned}$$

where $M_0 = M(T, H_0)$ and denoting $H_0 + (\omega_z/\gamma)$ by H_0'. We define M_+ as $M_{x'} + iM_{y'}$, then,

$$\begin{aligned}
\frac{dM_+}{dt} &= -M_+\alpha + i\gamma M_0 H_1; \text{ where } \alpha = \frac{1}{T_2} + i\gamma H_0' \\
\frac{dM_+}{dt} &= -\alpha(M_+ - i\gamma M_0 H_1/\alpha) \\
\frac{d(M_+ - i\gamma M_0 H_1/\alpha)}{dt} &= -\alpha(M_+ - i\gamma M_0 H_1/\alpha) \\
M_+ - i\gamma M_0 H_1 &= Ae^{-\alpha t}.
\end{aligned}$$

Therefore, we obtain

$$M_+ = Ae^{-\alpha t} - \frac{i\gamma M_0 H_1}{1/T_2 + i\gamma H_0'}. \tag{2.22}$$

If we neglect the transient term and substitute $M_0 = \chi_0 H_0$, and define $\omega_0 = \gamma H_0$, $\omega_z = \omega$, we get

$$M_+ = -\frac{i\gamma M_0 H_1}{1/T_2 + i\gamma H_0'},$$

Then,

$$M_{x'} = \chi_0 \omega_0 T_2 \frac{(\omega_0 - \omega)T_2}{1 + (\omega_0 - \omega)^2 T_2^2} H_1, \tag{2.23}$$

$$M_{y'} = \chi_0 \omega_0 T_2 \frac{1}{1 + (\omega_0 - \omega)^2 T_2^2} H_1. \tag{2.24}$$

When the rotating frame (x', y') converts to the laboratory frame (x, y), we obtain

$$M_x(t) = M_{x'} \cos(\omega t) + M_{y'} \sin(\omega t). \tag{2.25}$$

If we write the magnetic field as being a linear filed,

$$H_x(t) = H_{x0} \cos(\omega t), \quad 2H_1 = H_{x0} \tag{2.26}$$

then we see that both $M_{x'}$ and $M_{y'}$ are proportional to H_{x0} and we can write

$$M_x(t) = (\chi'(\omega)\cos\omega t + \chi''(\omega)\sin\omega t)H_{x0}, \tag{2.27}$$

definning the quantities $\chi'(\omega)$ and $\chi''(\omega)$. By using (2.25) and (2.26), we get

$$\chi'(\omega) = \frac{\chi_0}{2}\omega_0 T_2 \frac{(\omega_0-\omega)T_2}{1+(\omega_0-\omega)^2T_2^2}, \tag{2.28}$$

$$\chi''(\omega) = \frac{\chi_0}{2}\omega_0 T_2 \frac{1}{1+(\omega_0-\omega)^2T_2^2}. \tag{2.29}$$

It is convenient to regard both $M_x(t)$ and $H_x(t)$ as the real parts of complex functions $M_x^C(t)$ and $H_x^C(t)$. Then, the compex susceptibility χ is obtained as

$$\chi(\omega) = \chi'(\omega) - i\chi''(\omega), \tag{2.30}$$

By writing as

$$H_x^C(t) = H_{x0}e^{i\omega t}, \tag{2.31}$$

we find

$$\begin{aligned} M_x^C(t) &= \chi(\omega)H_x^C(t) && (2.32)\\ &= (\chi'(\omega) - i\chi''(\omega))H_{x0}e^{i\omega t} && (2.33)\\ &= (\chi'(\omega) - i\chi''(\omega))H_{x0}(\cos\omega t + i\sin\omega t) && (2.34)\\ &= (\chi'(\omega)\cos\omega t + \chi''(\omega)\sin\omega t)H_{x0} && (2.35)\\ &\quad +i(\chi'(\omega)\sin\omega t + \chi''(\omega)\cos\omega t)H_{x0}. && (2.36) \end{aligned}$$

Then, we see again (2.26) as

$$M_x(t) = Re\chi' H_x^C(t) = (\chi'(\omega)\cos\omega t + \chi''(\omega)\sin\omega t)H_{x0} \tag{2.37}$$

The integral of χ'' is essentially the area under the absorption curve.

When we perform the NMR measurement with continuous wave

— 2.3.3 Detection of the NMR signal —

If a coil with a inductance L_0 filled with a material of susceptibility χ, the inductance is increased to

$$L(\omega) = L_0(1 + 4\pi\eta\chi(\omega)), \tag{2.38}$$

where η is a quantity of "filling factor" and is less than 1.

Denoting the coil resistance in the absence of a sample as R_0, the coil impedance Z becomes

$$\begin{aligned} Z(\omega) &= iL_0\omega(1 + 4\pi\eta\chi(\omega)) + R_0\\ &= iL_0\omega(1 + 4\pi\eta\chi'(\omega) - i4\pi\eta\chi"(\omega)) + R_0\\ &= iL_0\omega(1 + 4\pi\eta\chi'(\omega)) + 4\pi L_0\omega\eta\chi"(\omega) + R_0. \end{aligned}$$

The real part of the susceptibility χ' therefore changes the inductance, whereas the imaginary part χ'' modifies the resistance. The fractional change in resistance $\delta R/R_0$ is given as

$$\frac{\Delta R}{R_0} = \frac{L_0\omega}{R_0} 4\pi\eta\chi''(\omega) = 4\pi\eta Q\chi''(\omega), \tag{2.39}$$

where we introduce the quality factor Q, typically in the range of 50 to 100 for NMR coils.

Chapter 3

Equipments

Section 3.1

Cryogenic and magnet systems

The polarized HD system consists of five refrigerators called SC, TC1, DRS, TC2 and IBC (see Fig. 3.1). The three cryostats SC, TC1, TC2 are liquid-^{4}He cryostats used during the transportation of the HD target. The SC and the TC1 cryostats were donated by France ORSAY group to us after the end of their project. The production of the polarized HD target is simply explained as follows.:

1. At RCNP, pure HD gas with the amount of 1 mole is produced by using the HD gas distillator.

2. The HD gas is solidified at the Storage Cryostat (SC), and the polarization of the reference HD is measured in the SC.

3. Another ^{4}He refrigerator called Transfer Cryostat 1 (TC1) allows us to move the solid HD target from the SC to the Dilution Refrigerator System (DRS) by keeping the HD target at 4 K.

4. The polarization of the solid HD is grown and is frozen by aging at B=17 Tesla and at T=14 mK in DRS.

5. The polarized HD target is transferred from the dilution refrigerator (DRS) to the SC by using the TC1.

6. The polarization of the HD target is measured in the SC.

7. The SC is transported to SPring-8/LEPS by a truck.

8. At SPring-8/LEPS, the polarized HD is transferred from the SC to a dilution refrigerator, called "In-Beam Cryostat" (IBC) by using the last ^{4}He refrigerator called "Transfer Cryostat 2" (TC2).

All polarization measurements are performed by using the SC. The flow chart of the target transportation is shown in Fig. 3.1. The IBC will be operated under the

condition with a magnetic field of 1 Tesla and a temperature of 300 mK during the physics experiment for a few months.

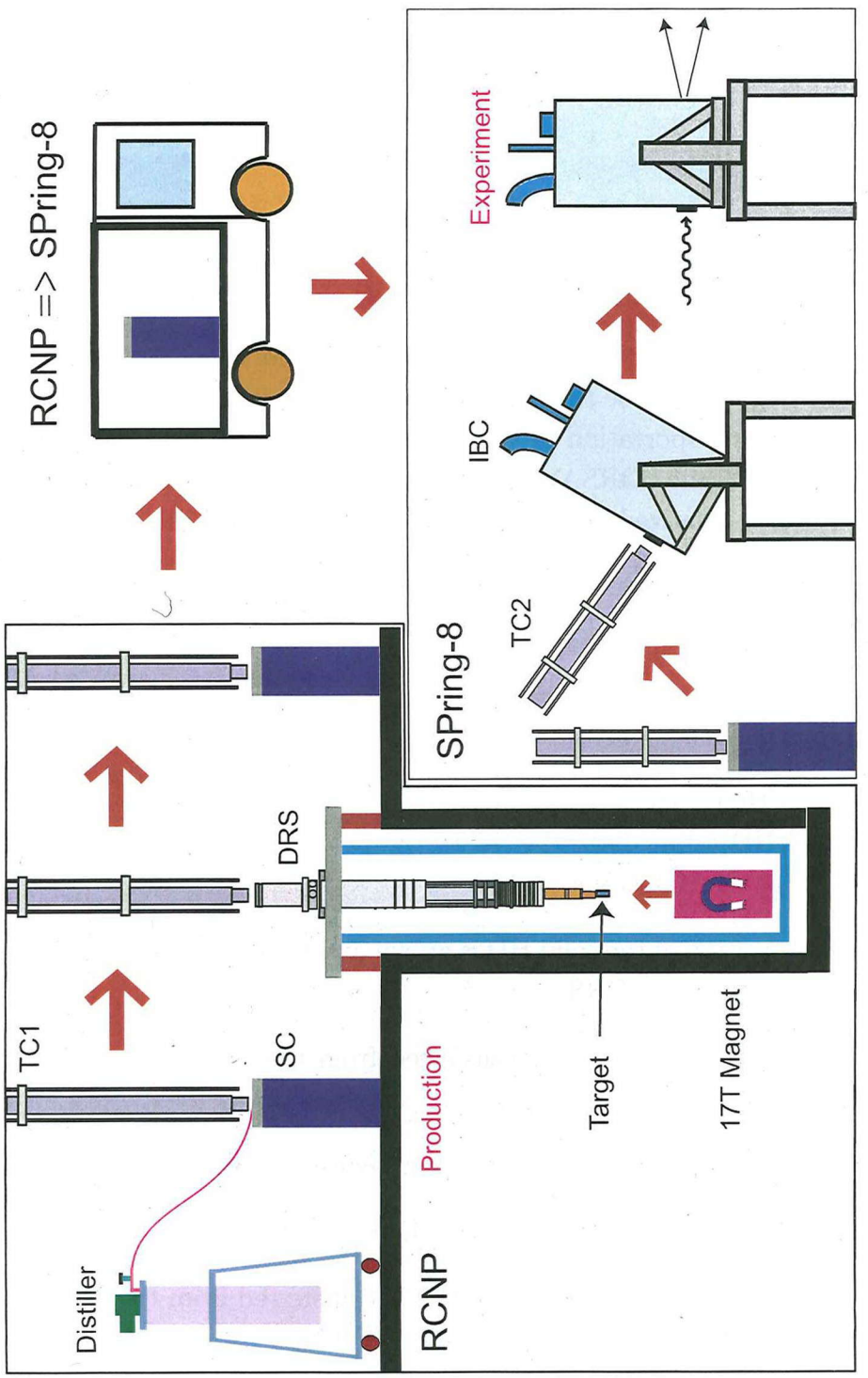

Figure 3.1: The flow chart of target transportation.

Section 3.2
Distillator

The purity of commercial HD gas is about 96%. The main contaminations are H_2 (2%) and D_2 (2%). Distillator purifies the HD gas up to 99.99% in order to optimize the amount of impurities. There are packings called "Helipack" inside the distiller. Temperature gradient is realized by cooling the top and heating the bottom of the distiller. Heat exchange between gas and liquid takes place on the packings. A low-boiling element is vaporized and extracted from the top of the distiller. The difference of the boiling points of HD, H_2 and D_2 enables for the HD gas to be separated from the others. The concentration of H_2 and D_2 is measured by a quadrupole mass spectrometer. [58]

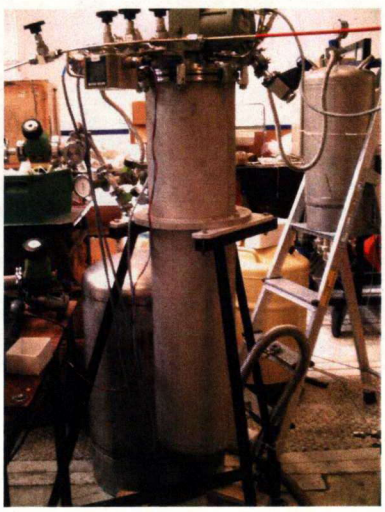

Figure 3.2: Photograph of distiller for HD gas

Section 3.3
Storage Cryostat (SC)

The Storage Cryostat (SC) is used for producing the soild HD and for holding the polarized HD target on the way of the transportation from RCNP to SPring-8. The cryostat (SC) is fabricated by Oxford, and consists of a stock cryogenic system with vacuum-cooler in a liquid helium bath with a standard liquid nitrogen space and shield. It contains a custom-built insert which holds the target and the NMR coil-frame. The SC is transported to SPring-8/LEPS by using a truck. The SC has an evaporative liquid-He refrigerator system with a lowest temperature of 1.2 K and with a superconducting magnet with the highest magnetic field of 2.5 Tesla. During

the transportation of polarized HD target, the power supply for a vacuum pomp and instruments is supplied from a 12 V battery. The SC is also used to solidify the HD gas and to measure the polarization of the reference HD.

Figure 3.3: The photo picture of the Storage Cryostat (SC)

Section 3.4

Dilution Refrigerator System (DRS)

The DRS is to polarize the HD target for the first stage at RCNP. We prepared a vertical hole, where the dilution refrigerator (DR) and a dewar were installed. The depth of the hole is 5.5 m. The diameter of the hole is 1.6 m. A support frame for the DR and the dewar was constructed to remove vibrations for avoiding the temperature increase of the target. We installed the DR, fabricated by Leiden Cryogenics, with a cooling power of 2500W at 120 mK and a lowest temperature of 6 mK (see Fig. 3.6). Figure 3.4 shows the photographs of the dilution refrigerator unit.

The dilution refrigerator is controlled by a gas-handling system, coupled to each other by flexible stainless-steel lines, cables for the valves and gauges fitted to the insert (see Figure 3.4). The ^{3}He and ^{4}He mixture gas is circulated by means of two

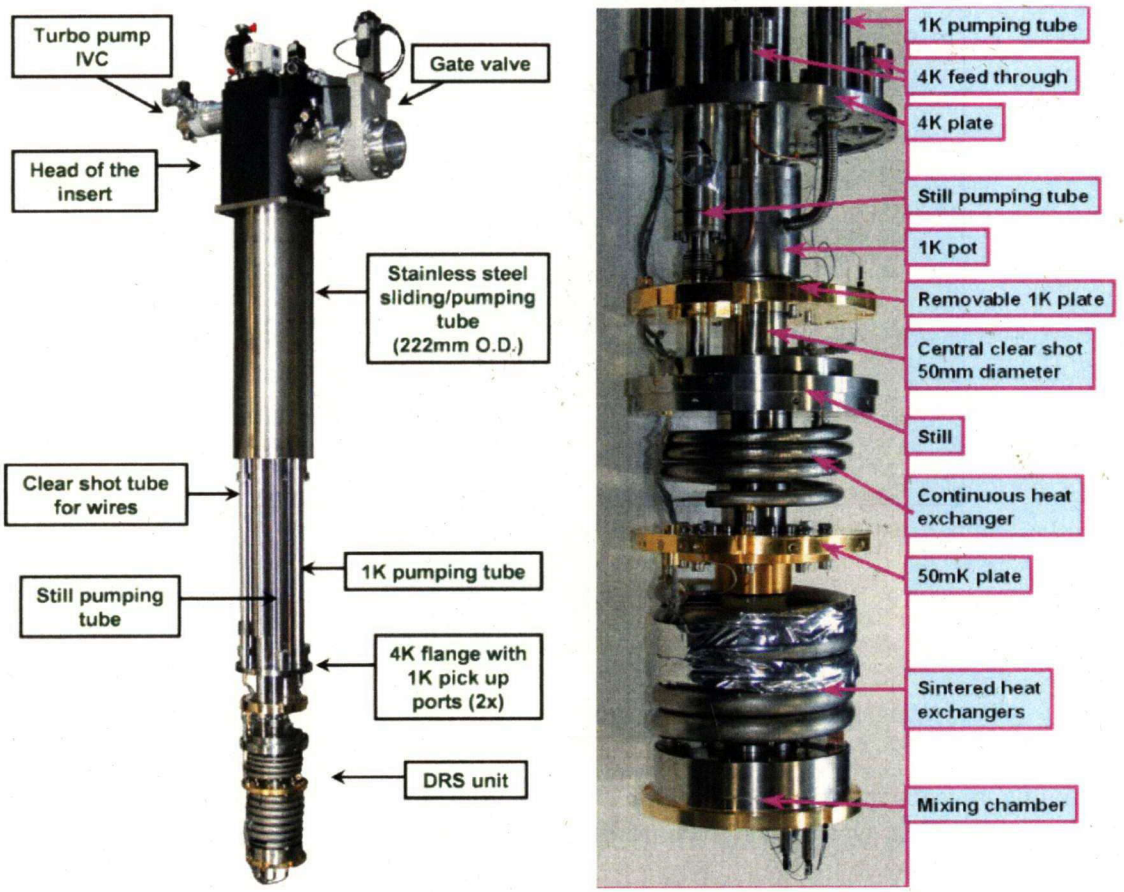

Figure 3.4: Photograph of the dilution refrigerator unit

turbo-molecular drag-pumps backed by a dry rotary pump. A turbo-drag pump is used for the evacuation of the IVC (Inner Vacuum Chamber).

The dilution refrigerator unit of the DRS series is screwed to the removable 1K pot. The still is fitted with a capacitance level gauge, a heater and a 10 kW RuO_2 resistance thermometer. All are placed inside the liquid. The temperature of the 1K pot (which is a part of the insert) is measured with a similar thermometer. The mixing chamber is fitted with a Speer 100 W thermometer that has been sliced and inserted into a special copper holder, together with small capacitance filters. A 1K pot is attached to the bottom flange of the insert with a Kapton o-ring. It contains two copper-spiral heat exchangers for precooling and condensing the mixture. As shown in Fig. 3.5, the ^{4}He liquid is fed to the 1 K pot via two lines. One goes directly to ^{4}He bath, with a high impedance. The other goes through a bypass micro-valve placed at the top of the insert and has a lower impedance. The high impedance one is used in normal operation while the low impedance one is used during condensation or at the highest circulation rates. The inlet ports for the 1 K pot are placed on the bottom flange of the insert (4 K flange), and are fitted with removable filters. The dilution refrigerator unit is screwed to the 1 K pot by means of a flexible bellows

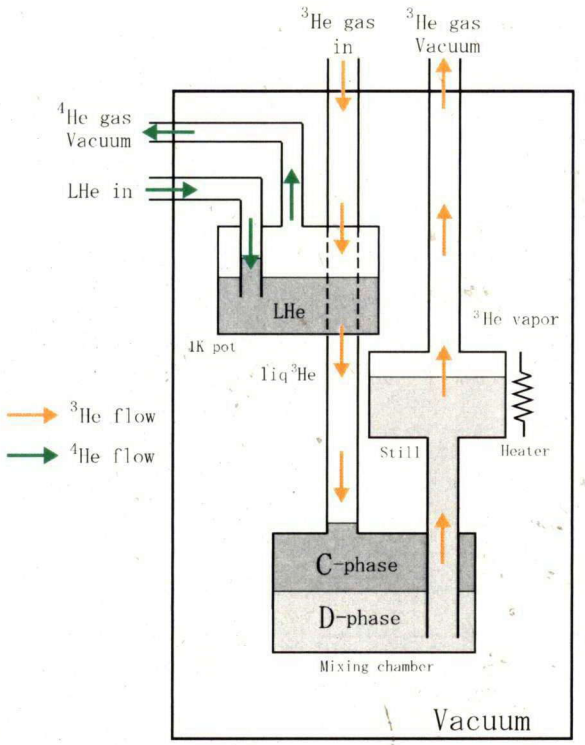

Figure 3.5: Detailed flowchart of the ^{3}He-^{4}He gas circulation system

and flange fitted with a Kapton o-ring. It is also screwed to the 50 mm central hole of the 1 K pot but without sealing rings. The unit consists of a still, a cold-plate and a mixing chamber plus a series of heat exchangers. The mixing chamber is made of an upper part of stainless steel and a bottom part of gold-plated copper where a number of samples can be fastened. The still is made completely of stainless steel with a flange where a silver-plated copper shield is attached. A cold-plate (CP) at a temperature of around 60 mK is fitted between the still and the mixing chamber (MC) for thermal anchoring. The unit has a tube-in-tube continuous heat exchanger (HE) followed by a silver HE, before the 60 mK plate, and a continuous silver HE between the cold-plate and the MC. The still and CP radiation shields are cylindrical, but tails can be optionally added.

Section 3.5

17 T Superconducting magnet

Figure. 3.7 shows the superconducting magnet for making the polarization of HD. The magnet generates a high magnetic field of 17 Tesla in the region of 7 cm in diameter. The polarized HD target, which is located at the inside of the DRS,

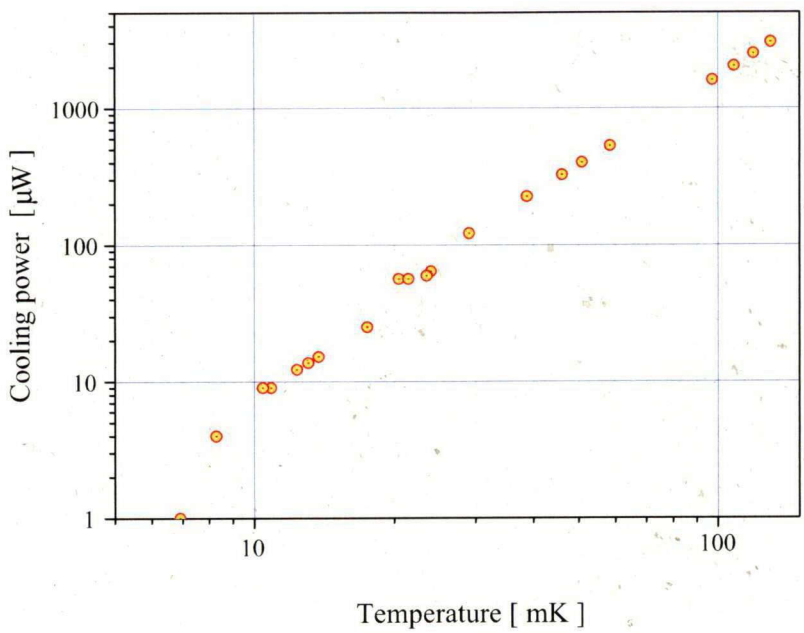

Figure 3.6: Measured cooling power of dilution refrigerator

is placed at the center of the magnet. The magnet has a structure in which the magnetic field does not make a spin reversed. In the case of a normal solenoid coil, a generated magnetic field of the solenoid coil cross over 0 Tesla at the edge of the coil. The magnetic field makes a spin reverse and induces depolarization of the polarized target when the polarized HD target is extracted. The 17 Tesla superconducting magnet has a null coil which generates a weak magnetic filed to prevent the depolarization of polarized target.

The super conducting magnet is fabricated by Japan Superconductor Technology Inc. (JASTEC) in Japan. A superconducting wire employed is Nb_3Sn (Niobium Tin) conductors of which critical temperature is 18 K manufactured by the bronze process. The wire is reinforced by Ta (Tantalum) located in the center to fit special needs of high enough in strength, stable in time and uniform in space. The first two points depend on two fundamental characteristics of the applied superconducting wires, that is a high limited current and a high limited temperature in a high magnetic field. Moreover, the magnetic force on the wire increases with increasing the magnetic field. Therefore, an improvement of mechanical properties of the wire is required for generating a high magnetic field. The wire is rolled to aluminum bobbin with a high tension for preventing a small space movement of the wire. The small movement induces the quenching when a high electrical current is applied to the wire. The wire is fixed to the bobbin by epoxy. A high magnetic field of 17 T is achieved after these processes.

A high magnetic field induces heat-up of the mixing chamber and the cold finger which are placed upper of the target. The magnetic field induces the eddy current

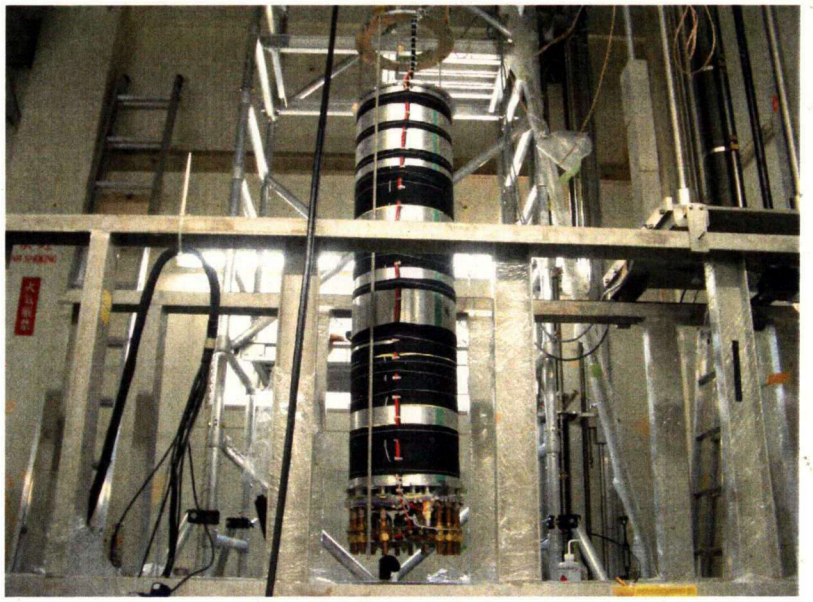

Figure 3.7: Photograph of the 17 Tesla superconductor magnet

in the conductive metal inside the superconducting magnet. In the region of the mixing chamber of the DRS, the magnetic field has to be kept under 400 gauss.

Figure 3.8 shows the measured magnetic field of the superconducting magnet. The measurement is performed along with the vertical axis of the solenoid coil. The dotted points are the measured value. The curve shows that the agreement between the designed values and the measurements are good. The measured value is in agreement with the designed value with the accuracy less than 10^{-4}. This magnetic field is sufficient for the NMR measurement to obtain the polarization of the HD target.

Table 3.1: The parameters of the superconducting magnet.

Nominal current at 17 T	271.8 A
Ramp-up time (0 $\rightarrow$ 17 T)	20 min
Field homogeneity ($\triangle$/B)	10^{-5}

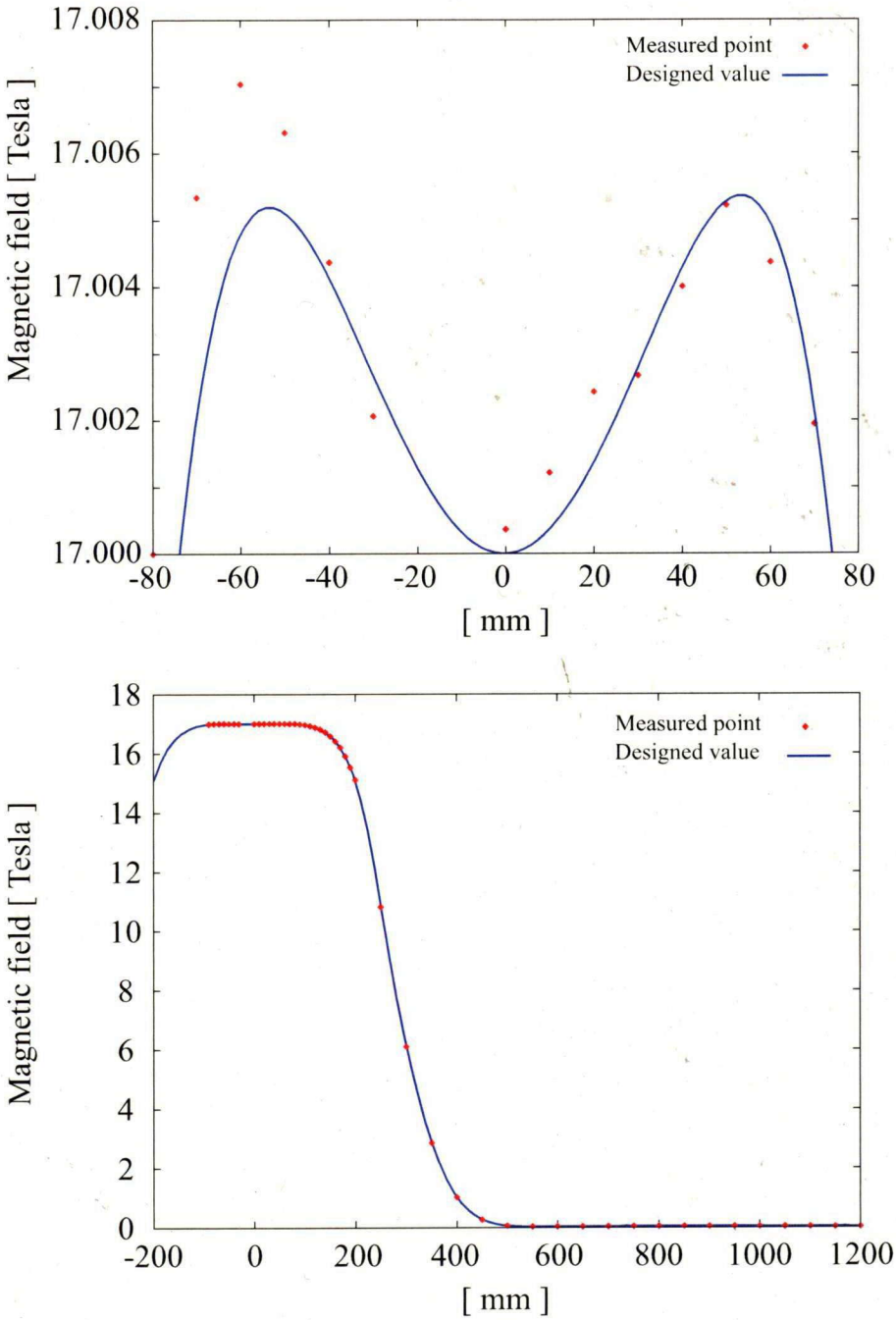

Figure 3.8: The magnetic field distribution along the central axis of the 17 Tesla superconducting magnet. The measurement is performed along the vertical axis of the solenoid coil. The dotted points are the measured values. The upper panels shows the distribution of the magnetic field in the region of the vertical axis z from -80 mm to +80 mm. The lower panels showsthe distribution of the magnetic field in the region of thevertical axis z from -200 mm to +1200 mm. The z=0 mm position indicates the center of the target cell

Section 3.6

Transfer Cryostat 1(TC1) and (TC2)

After completing the polarization process, the HD target is extracted from the DRS. The Transfer Cryostat (TC) is used for transferring the polarized HD target from one cryostat dewar to another. The TC1 are provided by France IPN Orsay in 2006 and is mainly used for moving the HD target between the DRS and the SC.

Figure 3.9 shows the photographs of the TC1 and TC2. The TC1 has the three-layer structure which consists of LN_2 layer, magnet layer and target layer. In each layer, liquid N_2 or liquid He is stored. The LN_2 layer is cooled by liquid nitrogen, and shields the radiation heat to the inner layer from the outer layer. The magnet layer has a superconducting magnet and is cooled down by liquid-He. The superconducting magnet generates a magnetic field of 0.1 Tesla, and hold the target polarization during a transfer process. The target layer has a set-in structure at the end, and is used to extract the target cell which is placed in the DRS or the SC. The target cell is hold in the DRS and the SC with a right hand thread structure. When the target cell is extracted from the DRS, the target layer extends to the tip of the cold finger in the DRS 3.5 meter away. The target cell is removed by screwing left hand, and is extracted with a temperature of 4.2 K and of magnetic field of 0.5 Tesla. The Transfer Cryostat 2 (TC2) is mainly used for moving the target from the SC to the IBC in SPring-8. The shield layer and magnet layer are cooled down by the 4.2 K refrigerator. The target layer is cooled down by liquid-He. The TC2 allows us to operate with a lying position.

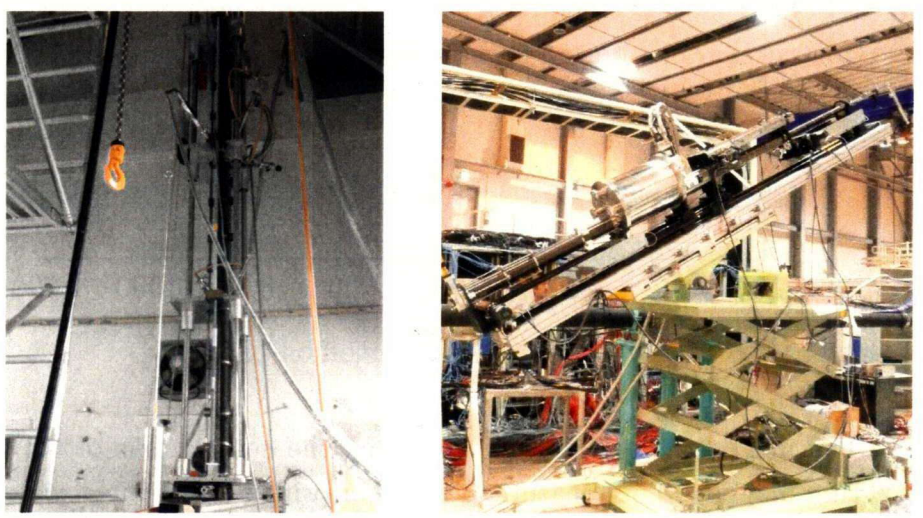

Figure 3.9: Photographs of the TC1 (left) and TC2 (right). The TC1 is used for moving the target from the DRS to the SC. The TC2 is used for moving the target from the SC to the IBC.

Section 3.7

In Beam Cryostat (IBC)

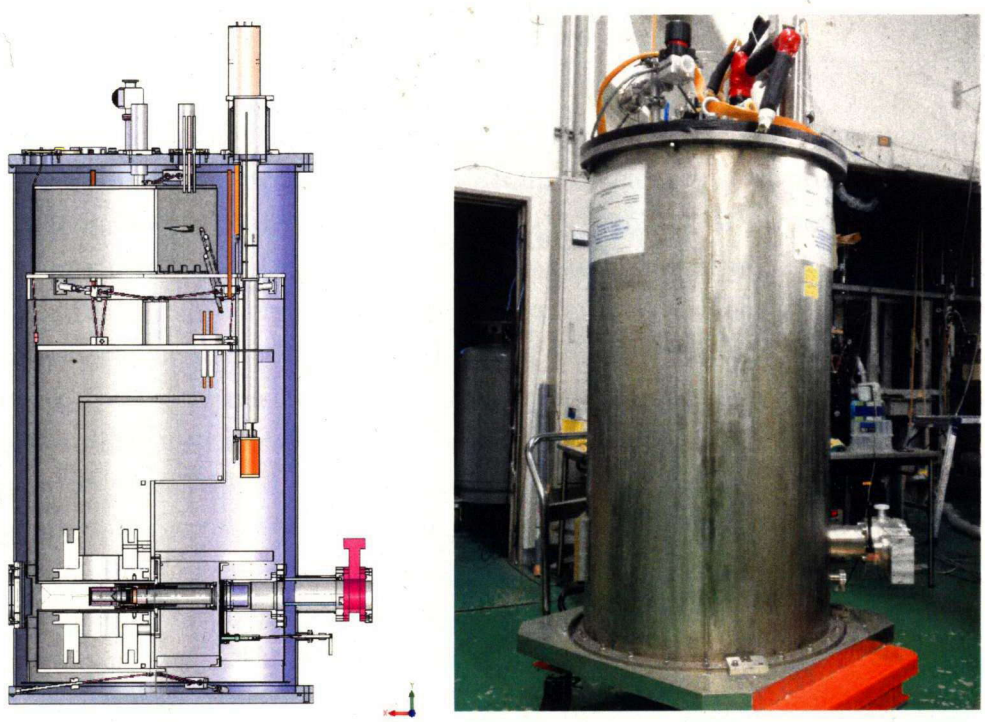

Figure 3.10: Left:Schematic drawing of the In Beam Cryostat (IBC) used during the experiment. Right: Photograph of the IBC

The In Beam Cryostat (IBC) is used to cool the target and to rotate the spin direction during the experiment at SPring-8. Figure 3.10 shows the perspective drawing the real picture of the IBC. The IBC mainly consists of a ^{3}He-^{4}He dilution refrigerator with a superconducting magnet. The dilution refrigerator part in the IBC is saved by a liquid nitrogen shield and has a helium refrigeration condenser to minimize evaporation. The cooling power of dilution refrigerator is 1000 μW at 350 mK. The attainable temperature is as low as 250 mK. The magnetic field to hold the polarization of the HD target is 1 Tesla. The superconducting magnet is a Helmholtz coil, which is set up around the polarized target for rotating the spin direction. The homogeneity of the longitudinal magnetic field is 7×10^{-4} in the HD target region. The polarization of the HD target is observed during the experiment by using an NMR system. The polarized HD target is inserted to the IBC by using

the TC2.

The IBC is installed just in front of the LEPS spectrometer as shown in Fig. 3.11. The gas circulation system and compressor are installed in the BL33LEP hutch and the control unit is placed outside the hutch. When the HD target is transferred from the TC2 to the IBC, the IBC is moved to the inside of the experimental hutch.

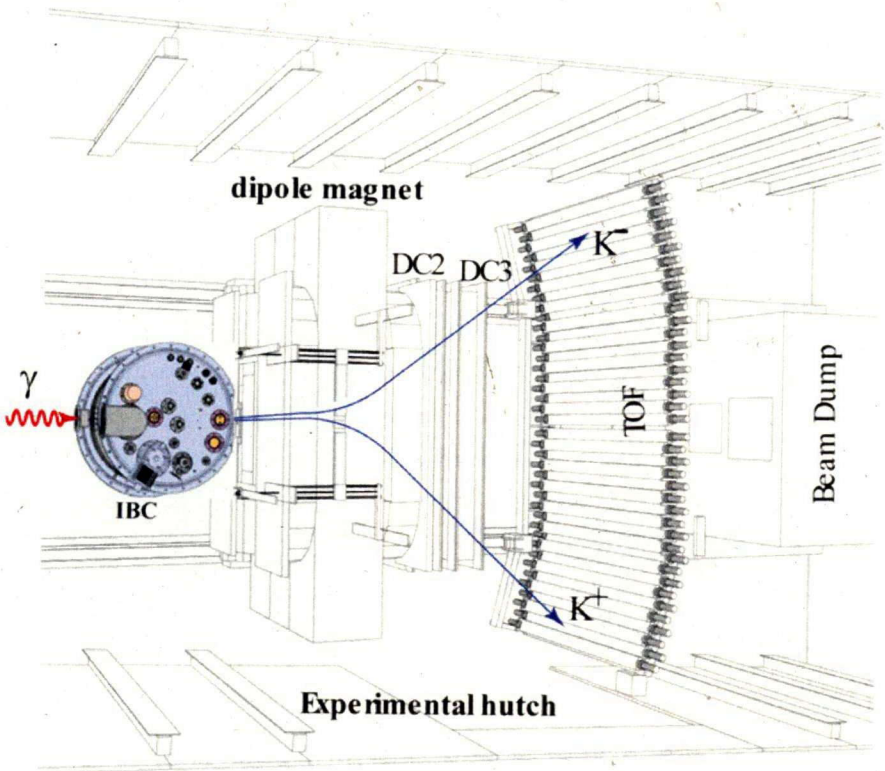

Figure 3.11: The IBC installed in front of standard LEPS magnetic spectrometer.

Section 3.8
NMR polarimeter

— 3.8.1 NMR principles —

Nuclear magnetic resonance (NMR) is a physical resonance phenomenon involving the observation of magnetic properties of an atomic nucleus in the presence of an applied external magnetic-field. All nuclei with odd numbers of protons and neutrons have an intrinsic magnetic moment and angular momentum. A large static magnetic field breaks the energy degeneracy between the nuclear Zeeman levels. The transitions between the split Zeeman levels are induced by a RF field applied perpendicular to the static magnetic field. The energy absorbed or emitted is proportional to the difference in the populations of the magnetic sub-states. Hence, the NMR signal is proportional to the polarization of the target material. The RF frequency required, known as the Larmor frequency, is determined by the gyromagnetic ratio of the nuclei of interest and the strength of the static magnetic field. In practice, the frequency response is broadened by small variations in the local magnetic field. However, the NMR resonance in a narrow frequency band is centered around the Larmor frequency, because the local magnetic field is normally weaker than the applied NMR field.

The net absorption or emission of electromagnetic radiation by the nuclear spin system can be modeled macroscopically as the imaginary component of complex magnetic susceptibility, $\chi(\omega) = \chi'(\omega) - i\chi''(\omega)$, where the real part represents the absorption part and the imaginary part represents the dispersion part. The vector polarization P can be written as

$$P \propto \int_0^\infty \chi''(\omega)\mathrm{d}\omega \tag{3.1}$$

which forms the basis that the polarization is determined by obtaining the NMR signal area.

— 3.8.2 NMR hardware and software —

The single coil method is used for both transmitter and receiver coils. When the single coil is used, one should construct an electronic circuit so that the RF signal from a transmitter does not mix with a signal from a receiver. Therefore, we use a cancellation circuit which is proposed by Jefferey and Armstrong [59]. Figure 3.12 shows a diagram of the cancellation circuit, the picture of the cancellation circuit and a Q curve response. The cancellation circuit can cancel a signal with a selected frequency. When a receiver coil receives the signal, the signals come from transmitter. However, the input signal is canceled easily by using a cancellation circuit. The responding NMR signal can pass through the circuit, and is detected as an output signal in the NMR measurement. Even if a cancellation circuit is employed, the frequency sweeping will produce unexpected noise.

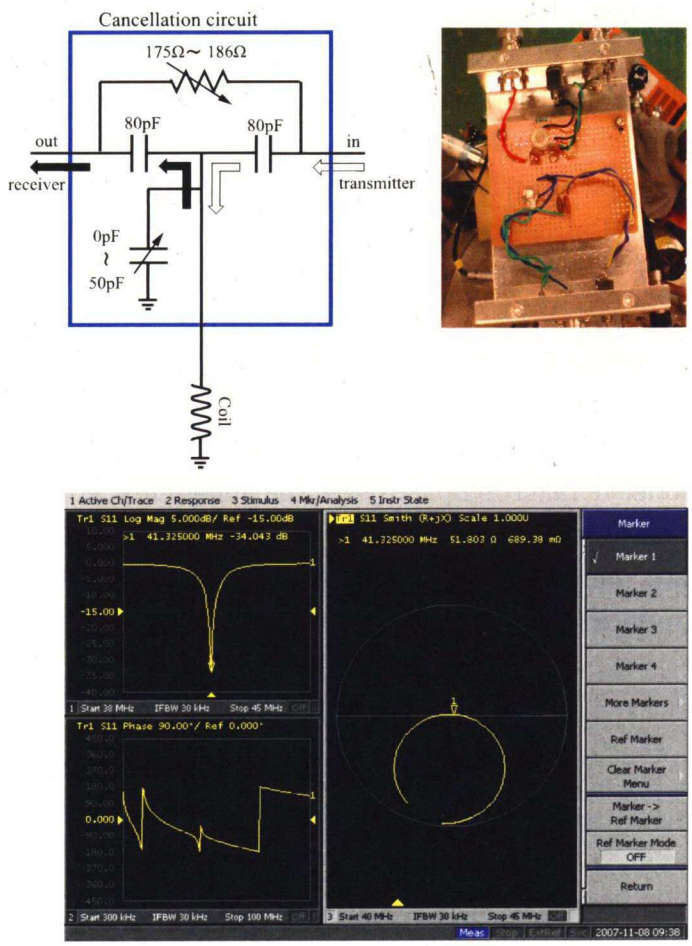

Figure 3.12: (a) The diagram of cancellation circuit. (b) The photograph of cancellation circuit. (c) The Q curve response.

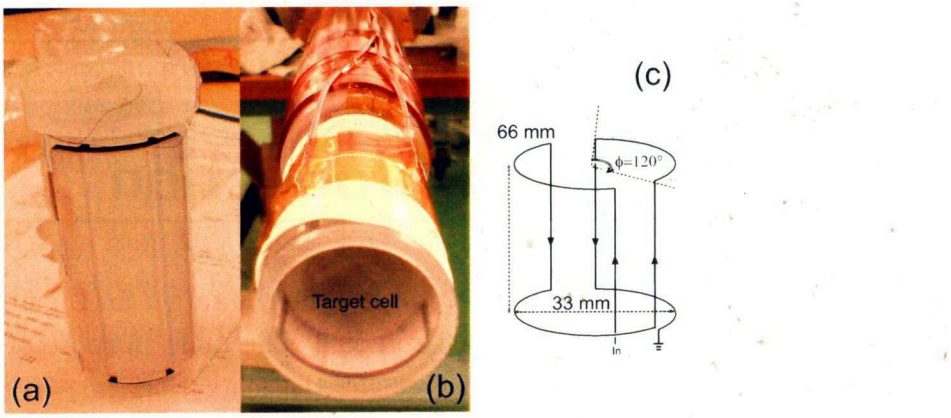

Figure 3.13: (a) The PCTFE coil supporter with a coil. The turn number of both the transmitter and receiver coils is 50. (b) The PCTFE coil supporter with the target cell. (c) The schematic drawing of the single coil.

Phase correction is performed by using the phase shifter in a lock-in amplifier, and is aligned the phase of the reference signal and measuring signal. In the lock-in amplifier, reference and measuring signals are multiplied and integrated. If two signals have the same frequency, one can get the amplitude of the signal. If the frequency of two signals are different, signal vanishes. Thus, we extract the small signal with a fixed frequency embedded in the large noise. Figure 3.13 shows the photographs of the NMR coil supporter, and the schematic drawing of the coil. Figure 3.14 is a diagram of the whole circuit for the NMR measurement.

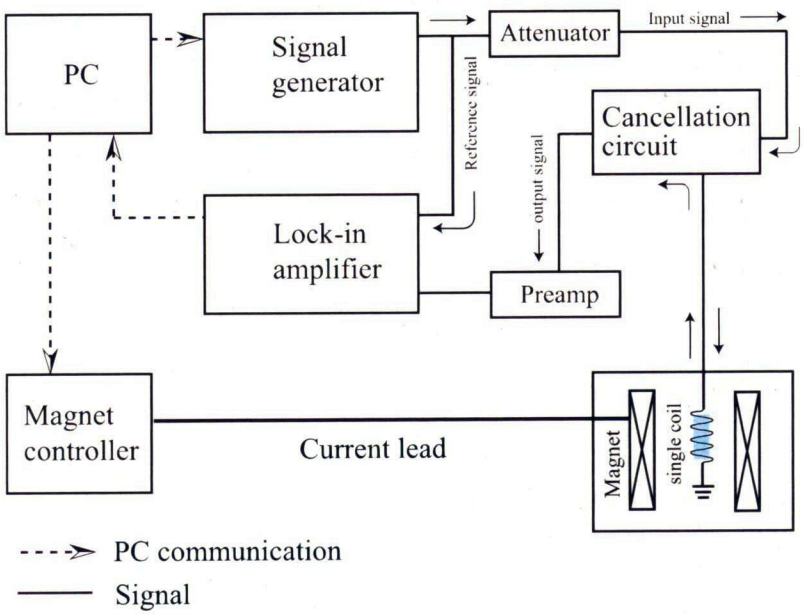

Figure 3.14: The signal flow of the single coil method for NMR.

Chapter 4

First production

We carried out an experiment to polarize the HD target for the first time at RCNP in the period from the end of 2008 to 2009. The main purpose of this experiment was to measure the polarization degree and the relaxation time T_1 of the HD target.

Section 4.1

Experimental setup and measurement

The HD gas was purified by the distiller before filling to the target cell. Firstly, the H reference signal was measured at 1 Tesla and 4.2 K without HD. And then the distilled HD gas was poured in the DRS via a 1/16" stainless tube. The concentrations and amount of HD gas are shown in table 4.1. The HD was solidified and the H reference signal was measured at 1 Tesla and 4.2 K with HD again. The NMR signal of HD is obtained from the difference between measured signals without HD and with HD. The obtained NMR signal of HD is used as a calibration signal at 1 Tesla at 4.2 K to determine the equilibrium polarization of the target. The equilibrium polarization of 0.024% is given by using the following equation,

$$P_H = \tanh\left(\frac{g\mu_h H_0}{k_B T}\right) = \tanh\left(\frac{2.79 \times 10^{-26} \cdot 1}{1.38 \times 10^{-23} \cdot 4.2}\right) = 0.024\%. \tag{4.1}$$

The produced HD target was continuously cooled at 15 mK and at 17 T. The polarization of HD was grown and was frozen after a long aging time. After 53 days, we measured NMR signals of the HD target. To evaluate the relaxation time of hydrogen, we continued to measure NMR signals for 20 days.

Figure 4.1 shows the NMR spectra of the HD target and cell. The H(hydrogen) peak and the F(fluorine) peak were confirmed in the NMR spectrum. Figure 4.1(a)

Table 4.1: The concentrations and amount of the HD gas poured in the cell inside the DRS.

concentrations			
$[H_2]$	[HD]	$[D_2]$	amount
1.26%	97.66%	2.07%	0.68 mol

shows the NMR spectra without HD for evaluation of background signal. The NMR signals of hydrogen and fluorine are observed in the spectra. The NMR signal of hydrogen seems to arise from grease and enamel wire. The NMR signal of fluorine arises from the coil-frame and cell made by PCTFE(Kel-F). Figure 4.1(b) shows the NMR signal with HD for evaluation of calibration signal. The NMR signal of hydrogen mixes signals from HD, grease and enamel. Figure 4.1(c) shows the first NMR signal of HD target with frozen polarization after long aging. A temperature is increased to 300 mK from 14 mK.

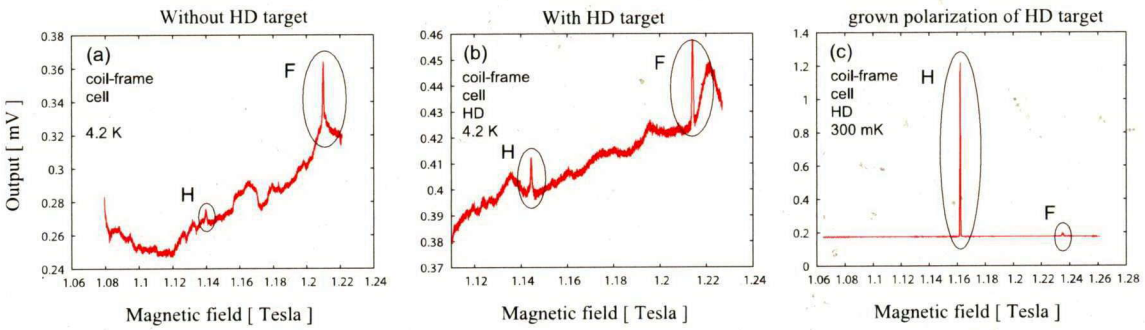

Figure 4.1: Measured NMR spectra at 4.2 K without HD, 4.2 K with HD and 300mK with HD after the aging. (a) the NMR spectrum obtained at 4.2 K without the HD target. (b) the NMR spectrum obtained at 4.2 K with the HD target. (c) the NMR spectrum of frozen polarization of hydrogen in the HD target at 300 mK after long aging . These NMR spectra are obtained by using the magnetic field sweep method at a frequency of ~48.4 MHz.

Fig. 4.2 shows the obtained NMR spectra of hydrogen and fluorine after the aging time of 53 days. The peak shape for hydrogen and fluorine were distorted. The distortion of the NMR spectra seems to arise from a inhomogeneity of magnetic field. This problem is discussed in the next section 4.6.

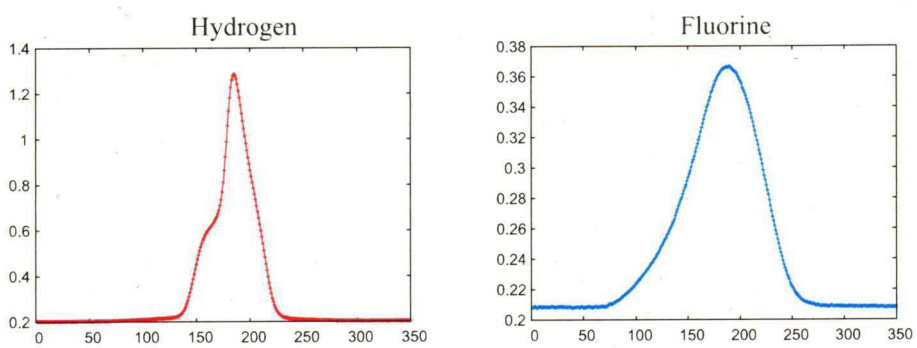

Figure 4.2: Distorted NMR spectra of hydrogen and fluorine. The NMR signal of hydrogen is distorted. The NMR signal of fluorine also seems to be distorted.

NMR measurement of D

In the NMR measurement for hydrogen in the HD, the NMR spectra of deuteron were also obtained. Figure. 4.3 shows the measured NMR spectrum of deuteron. A degree of distortion seems to be bigger than those for hydrogen and fluorine.

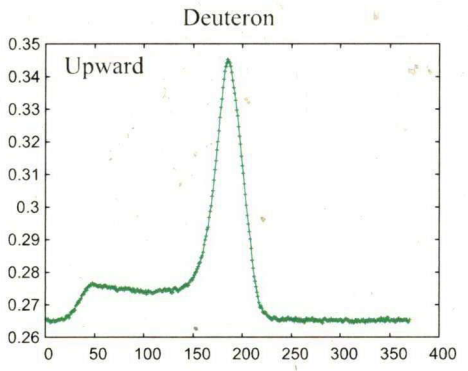

Figure 4.3: Obtained NMR spectrum of deuteron. The NMR peak for deuteron is more distorted

Decay of polarized signal

To estimate the relaxation time of hydrogen in the HD target, we continued to measure the NMR spectra. Figure. 4.4 shows the measured NMR spectra of hydrogen and fluorine. It is quite interesting to have observed the fact that the polarization of fluorine decreased quickly, while that of hydrogen was maintained for a long time. The measurement process was continued for 20 days after the aging.

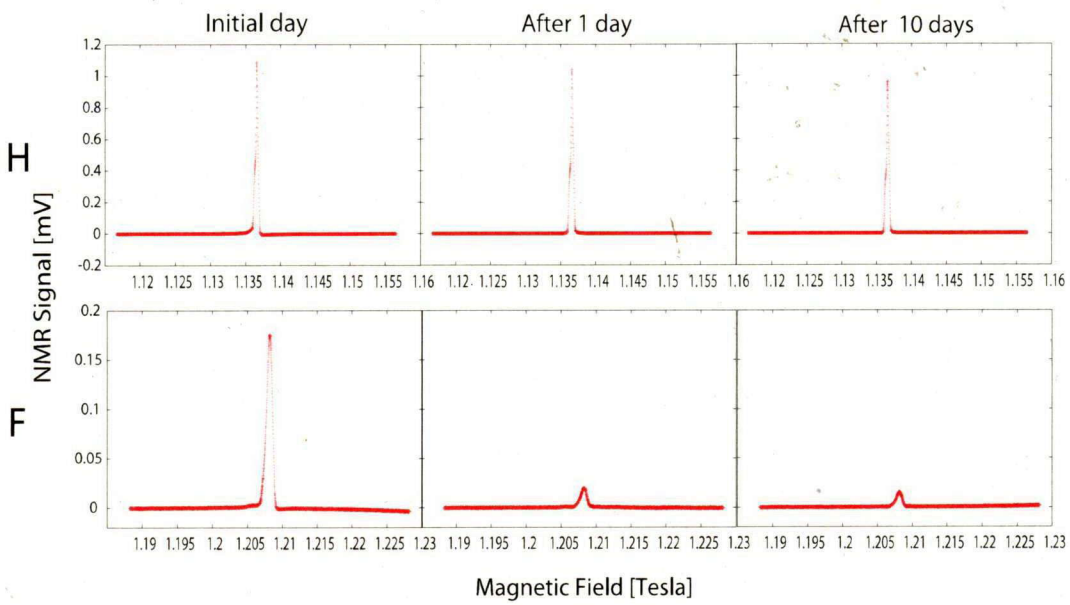

Figure 4.4: Observed NMR spectra with elapsed time. The NMR peak heights of H (top) and F (bottom) decay as a function of passage time. These signals were measured on initial day, after 1 day, and after 10 days.

Section 4.2
Preparation for analysis

— 4.2.1 Smoothing magnetic field data —

The NMR spectra are obtained by using the magnetic sweep method. When we sweep the magnetic field, we obtain an output signal strength as a function of the magnetic field strength of the superconducting magnet. Although the output signal passed through an AC filter, a fluctuation of signal remains. Figure 4.5 shows the fluctuation of magnetic field around the NMR resonance of hydrogen and a deviation. In the NMR measurement, the magnetic field is swept upward or downward with the fluctuation as shown in Fig. 4.5(a). The deviation is shown in Fig. 4.5(b). A standard deviation of this fluctuation is 0.2 mTesla and equal to ~0.2% of the strength of the magnetic field. The deviation is big compared with the width of the NMR spectra. The deviation is considered to be due to the actual magnetic field or due to the circuit noise.

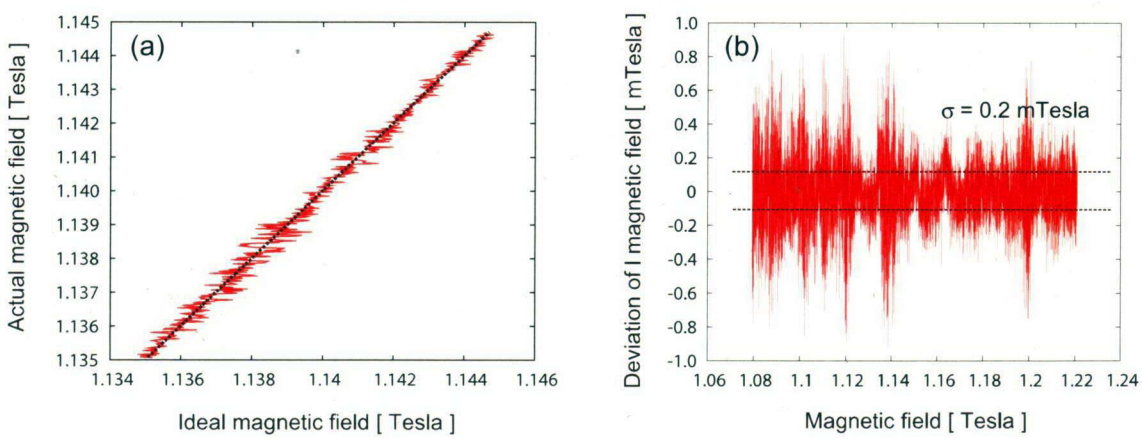

Figure 4.5: The fluctuation of magnetic field during the NMR measurement. (a) The fluctuation of magnetic field. (b) The deviation of magnetic field.

Figure 4.6 shows the obtained magnetic field data as a function of ideal magnetic field. The upper and bottom panels in Fig. 4.6 show the NMR spectra for hydrogen and fluorine, respectively. The data points of the NMR spectra in Fig. 4.6(a-1) and (a-2), which are ordered along the magnetic field, swing in response to the fluctuation of the magnetic field like Brown motion. On the other hand, the data

points of the NMR spectra in Fig. 4.6(b-1) and (b-2), which are ordered along the sequence number. If it is assumed that the actual magnetic field are fluctuated, the NMR data points shift to correspond to the fluctuation of the magnetic field. We consider that the actual magnetic field did not fluctuate but that the output signal from the power supply fluctuates. The output signal is obtained through a shunt register. The observed fluctuation maybe owe to a temperature fluctuation of the shunt register. For analysis, the obtained magnetic field have to be reassembled.

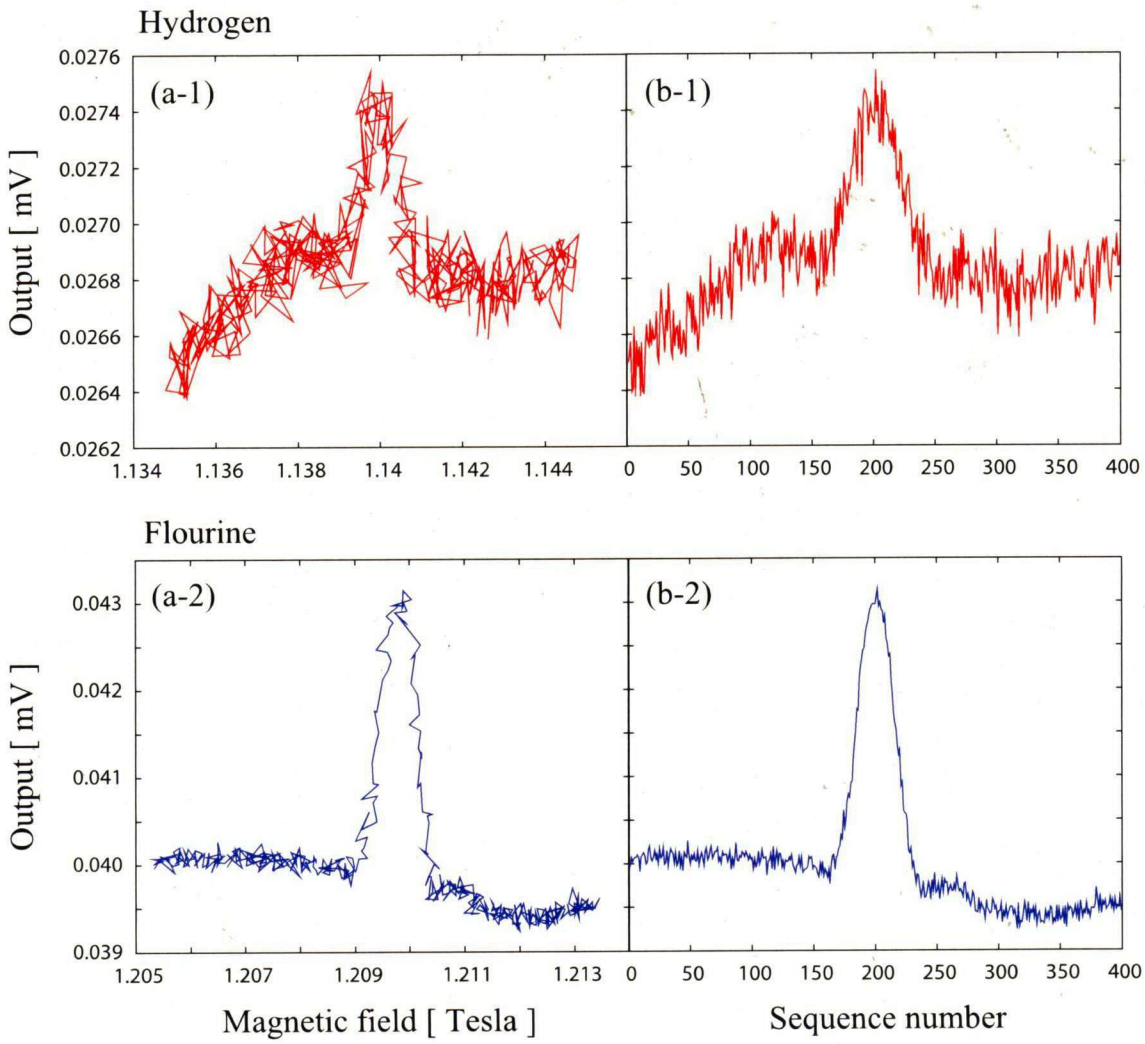

Figure 4.6: Comparison of the plotted the NMR spectrum as a function of the obtained magnetic filed (a-1),(a-2) and as a function of the sequence number (a-1),(a-2) in real time.

Since the width of NMR resonance is very narrow, the smoothing procedure of the magnetic field is beneficial in evaluating the NMR strength. We reassembled the magnetic field by polynomial fitting to the obtained magnetic field. Figure 4.7 shows the NMR spectra before and after the smoothing procedure of the magnetic

field.

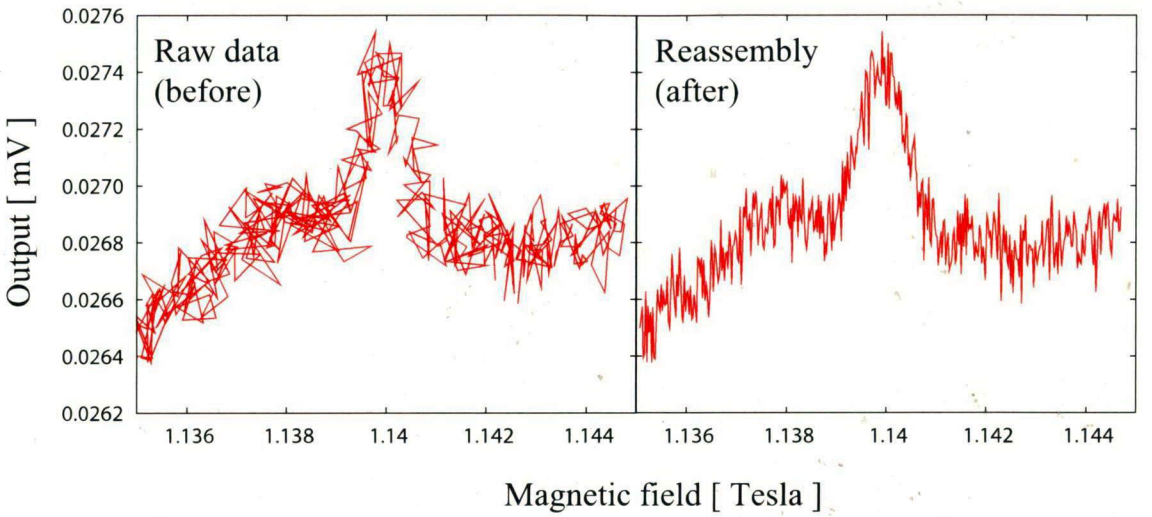

Figure 4.7: NMR spectra with/without the smoothing procedure of the obtained magnetic field.

— 4.2.2 Phase adjustment —

In practice, in a real NMR measurement, a phase correction is applied to either the time or frequency domain spectra to obtain an absorption spectrum as the real output. Phase correction is performed by the phase shifter in lock-in amplifier and is to align the phase of the calibration signal and measured signal. If the phases between the measuring signal and reference signal in lock-in amplifier are different, the value obtained is $I_n \sin\phi + Q_u \cos\phi$ (I_n is the inphase component and equivalent to χ''; Q_u is the quadrature component and is equivalent to χ'; ϕ is the difference of the phase). These value be able to re-coordinated as follows,

$$\begin{pmatrix} I'_n \\ Q'_u \end{pmatrix} = \begin{pmatrix} -\sin(\phi) & \cos(\phi) \\ \cos(\phi) & \sin(\phi) \end{pmatrix} \begin{pmatrix} I_n \\ Q_u \end{pmatrix} \tag{4.2}$$

We adjusted the phase in the lock-in amplifier when we got the signal. But that is just roughly adjusted by eyes. Figure 4.8 shows the examples of spectra with a good phase and a bad phase. The phase was adjusted in the measurement of NMR in the real time operation. However for a small NMR spectrum with a bad S/N ratio, the phase adjustment was difficult. In this case, the phase was re-adjusted in the analysis.

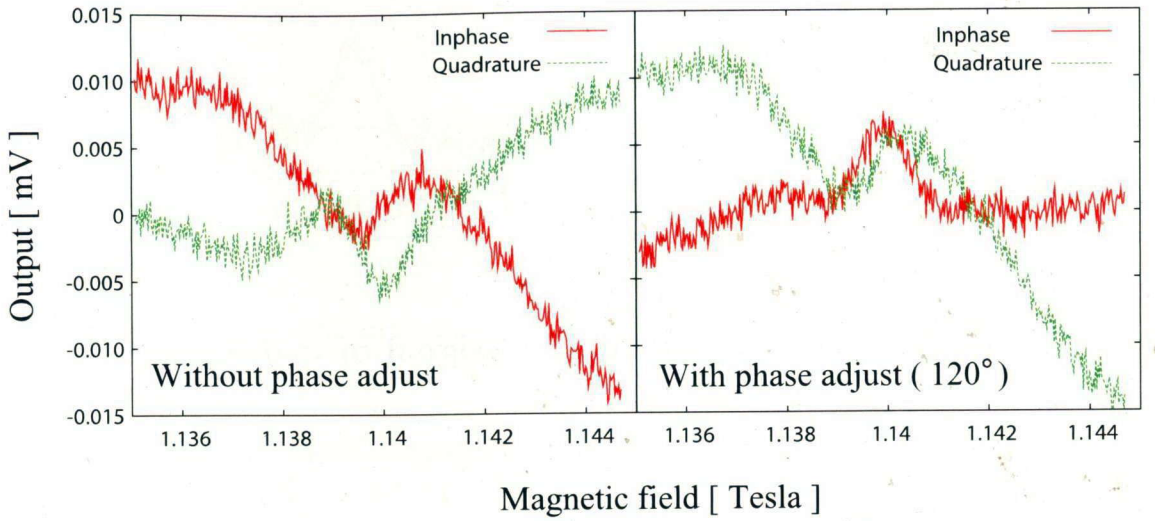

Figure 4.8: The NMR spectra with/without the phase conversion.

— 4.2.3 Position adjustment —

Although the magnetic field was smoothed, a position of the NMR peaks is shifted due to the hysteresis of superconducting magnet. The degree of shift differs between a upward and downward of the magnetic field. The difference of the center of the NMR peaks is 23 mTesla between the upward and downward. When we sweep the magnetic field in the same direction, the difference of the peak positions in the hydrogen NMR spectrum is 0.17 mTesla. We find the highest peak position by Gaussian fitting in the NMR spectrum, and shift the data points horizontally by adjusting the data point to the values expected from the theoretical resonance magnetic field.

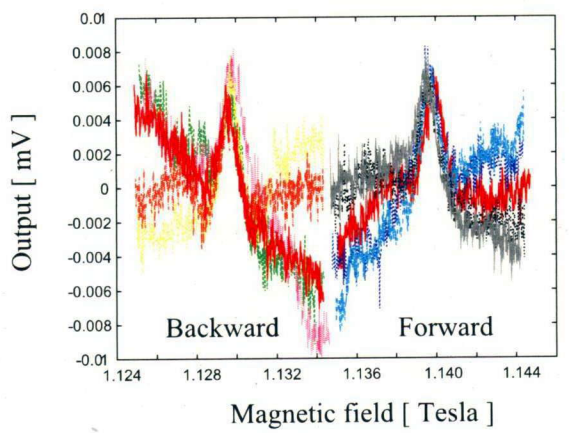

Figure 4.9: The NMR spectra obtained by sweeping the magnetic fields in the upward and downward directions.

Section 4.3
Analysis of NMR spectrum

— 4.3.1 Analysis of background signal of hydrogen —

In this analysis, we evaluate the background due to hydrogen included in grease and enamel wire. We measured a NMR spectrum at 4.2 K without the HD before pouring the HD gas to cell in the DRS. We considered that there was helium gas around the coil and a temperature of the HD was constant by heat exchange between outer liquid He and target via helium gas. Common parameters for measurement are listed in Table 4.2. Since the resonance frequency of hydrogen is 42.578 MHz, a resonance is calculated to locate at the position where the magnetic filed is 1.136 Tesla. The magnetic field was swept from 17.1 A to 19.9 A, which was equivalent from 1.08 Tesla to 1.22 Tesla. Data were acquired with a speed of 80000 samples per second. The acquired data was averaged every 5000 samples on time and recorded. Accordingly, an acquisition speed was the 40 data point/sec. The sweep speed was 300 A/1000 min. It took 9.3 min to raise up the magnetic field from 17.1 A to 19.9 A. In the NMR data, the data-taking time and the magnetic field were recorded in the real-time. A peak height and FWHM after the phase adjustment is obtained by using the polynomial function and with Gaussian fitting. Table 4.3 shows the analysis result of the measured NMR spectra with the analyzed filename. The NMR spectra were measured at 4.2 K without the HD target are shown in Fig. 4.10.

Table 4.2: Common parameters for the data set without the HD at 4.2 K.

Frequency	Sweep region	Sweep speed	Level	phase
48.373 MHz	17.1 A$\Longleftrightarrow$19.9 A	No.10 (300 A/1000 min)	-8 dbm	0
filter slope	Time constant	Sensitivity	rate	sample
24 dB/oct	1 ms	1 mVrms /10 V	80.000k	5.000k

These 10 spectra are summed up to make one spectrum. Figure 4.11 shows the summed NMR spectra. Three lines are drawn in the figure. "All" is the summed NMR spectra for all data. "Upward" is the summed NMR spectra for data taken with the upward sweeping of the magnetic field. "Backward" is the summed NMR spectra for data taken with the downward sweeping of the magnetic field. Off set is removed by fitting for comparison of"All", "Upward" and "Downward". There

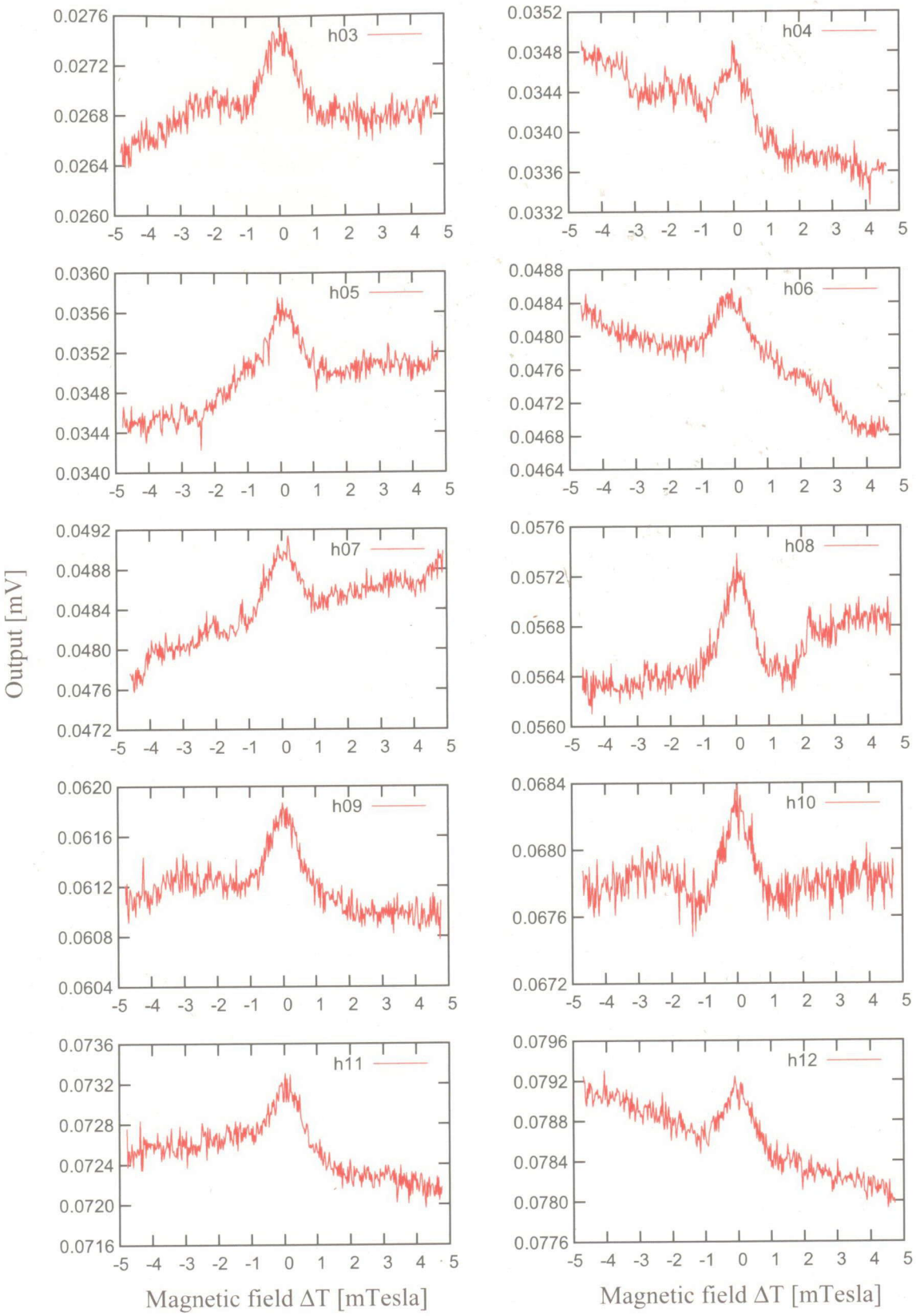

Figure 4.10: The NMR spectra obtained at 4.2 K without the HD target. The position of the magnetic field and the phase is adjusted. The NMR spectra h03,h05,h07,h09 and h11 runs are obtained at upward of the magnetic field. The NMR spectra h04,h06,h08,h10 and h12 runs are obtained at downward of the magnetic field.

Table 4.3: Analysis result of the NMR spectra obtained at 4.2 K without the HD target.

File name	Direction	Sampling speed			Phase [degree]	Height [μV]	Center [Tesla]	FWHM [mTesla]
		S/s	S/mTesla	mTesla/s				
h03	Upward	15.96	41.4	0.385	120.0	0.57	1.13989	1.43
h04	Downward	15.96	43.23	0.369	120.0	0.61	1.12976	1.41
h05	Upward	15.97	41.68	0.383	120.0	0.69	1.13959	2.07
h06	Downward	15.97	42.80	0.373	120.0	0.69	1.12999	2.07
h07	Upward	15.97	41.96	0.380	120.0	0.60	1.13965	1.42
h08	Downward	14.80	42.65	0.347	120.0	0.74	1.12968	1.31
h09	Upward	15.97	41.72	0.382	120.0	0.60	1.13966	1.44
h10	Downward	15.97	42.28	0.377	120.0	0.48	1.12963	1.18
h11	Upward	15.97	41.82	0.3820	120.0	0.62	1.13949	1.67
h12	Downward	15.97	42.26	0.378	120.0	0.55	1.12960	1.37

is almost no difference between "Upward" and "Downward" spectrum. The peak height is 0.0061. The FWHM of the peak calculated by Gaussian fitting is 1.48 mTesla .

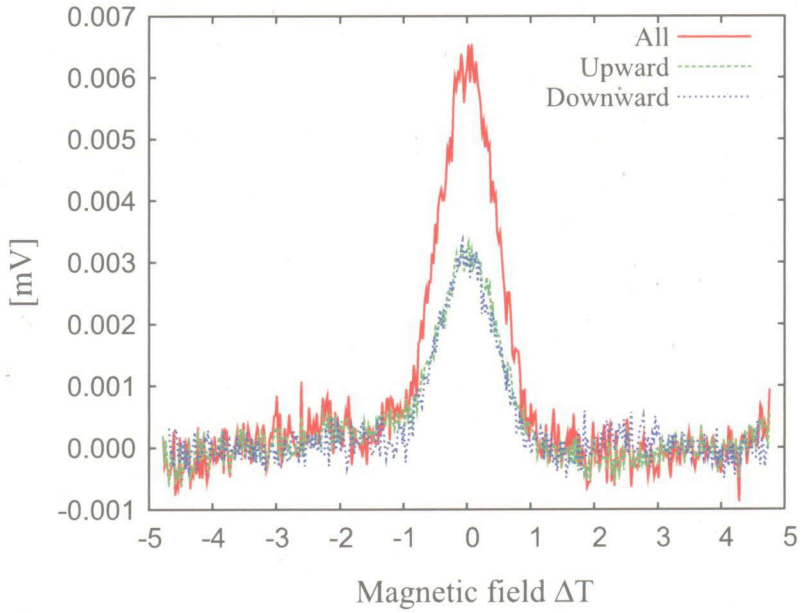

Figure 4.11: The summed NMR spectra from h03~h12 measured at 4.2 K without the HD.

The peak area in the spectra was obtained by various methods for estimating

systematic error. The peak in the summed NMR spectrum was fitted by using a polynomial or a linear function for estimating the background, and was fitted by using a Gaussian function. This fitting process is necessary for removing the background. The peak areas are obtained by integration of the NMR peak after subtracting the background. Figure 4.12 shows the fitted NMR spectra. Table 4.4 shows results of the peak areas of the summed NMR spectra. The fitting methods are listed as follows:

- "All" is a result of the NMR peak area obtained by fitting summed NMR spectra for all data using the polynomial and Gaussian functions in the region of 400 points.
- "Upward" is a result of the NMR peak area obtained by fitting summed NMR spectra for data taken with the upward sweeping of the magnetic field using the polynomial and Gaussian functions in the region of 400 points.
- "Downward" is a result of the NMR peak area obtained by fitting summed NMR spectra for data taken with the downward sweeping of the magnetic field using the polynomial and Gaussian functions in the region of 400 points.
- "Linear" is a result of the NMR peak area obtained by fitting summed NMR spectra for all data using the linear and Gaussian functions in the region of 400 points.
- "350 points" is a result of the NMR peak area obtained by fitting summed NMR spectra for all data using polynomial and Gaussian functions in the region of 350 points.
- "300 points" is a result of the NMR peak area obtained by fitting summed NMR spectra for all data using polynomial and Gaussian functions in the region of 300 points.

Table 4.4: Obtained peak areas in various fittings for data taken at 4.2 K without the HD target.

Fitting Method	All [mV]	Upward [mV]	Downward [mV]	Linear [mV]	Fitting region [mV]	
					350 points	300 points
Summed area	0.283	0.149	0.136	0.336	0.288	0.293
Statistical error	±0.004	±0.003	±0.003	±0.005	±0.004	±0.004

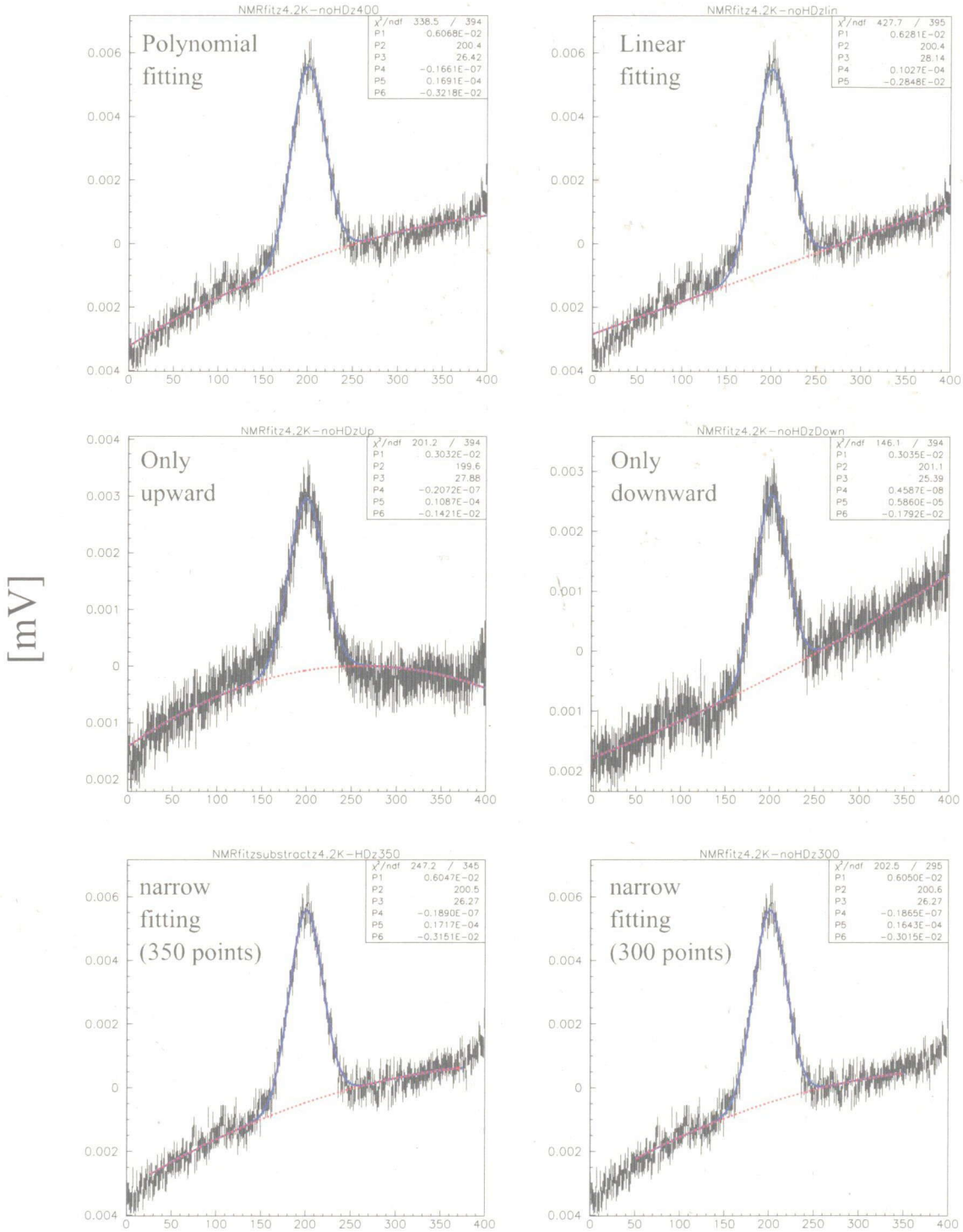

Figure 4.12: Fitting results of the summed NMR spectra obtained in the h13∼h22 runs at 4.2 K without the HD target.

— 4.3.2 Analysis of calibration signal of hydrogen —

In this analysis, we evaluate the NMR spectrum from HD, grease and enamel wire. The NMR spectrum of only HD is evaluated by subtraction. The NMR spectra were measured at 4.2 K with the HD target.

Common parameters for measurement are listed in Table 4.5. Table 4.6 shows the analysis result of measured NMR spectrum with analyzed filename. These spectrum were removed an off-set, adjusted the phase and positions to take the peak in the center. The NMR spectrum, which were measured at 4.2 K with the HD target, are shown in Fig. 4.13. The FWHM of the NMR peak is narrow compared to that of the NMR peak without the HD target. The height of the NMR peak is higher than that of the NMR peak without the HD target. Next, we summed the adjusted NMR spectra for H.

Table 4.5: Common parameters for data acquired at 4.2 K with the HD target.

Frequency	Sweep region	Sweep speed	Level	phase
48.373 MHz	17.1 A⇔19.5 A	No.10 (300 A/1000 min)	-8 dbm	0
filter slope	Time constant	Sensitivity	rate	sample
24 dB/oct	1 ms	1 mVrms / -47 dBm	80.000k	5.000k

Table 4.6: Analysis result of the NMR spectra obtained at 4.2 K with the HD target.

File name	Direction	Sampling speed			Phase	Height	Center	FWHM
		S/s	S/mTesla	mTesla/s	[degree]	[μV]	[Tesla]	
h13	Upward	15.97	41.66	0.3833	120.0	1.21	1.14412	0.97
h14	Downward	15.98	41.57	0.384	120.0	1.22	1.13439	0.88
h15	Upward	15.96	41.34	0.3861	120.0	1.24	1.14437	1.06
h16	Downward	15.98	41.87	0.3816	120.0	1.34	1.13450	1.03
h17	Upward	15.99	41.72	0.3831	120.0	1.30	1.14415	0.98
h18	Downward	15.97	41.50	0.3848	120.0	1.28	1.13432	0.97
h19	Upward	15.96	41.91	0.381	120.0	1.28	1.14428	1.18
h20	Downward	15.95	41.69	0.3827	120.0	1.31	1.13436	1.08
h21	Upward	15.96	41.91	0.3808	120.0	1.32	1.14442	1.06
h22	Downward	15.98	42.31	0.3776	120.0	1.32	1.13437	1.04

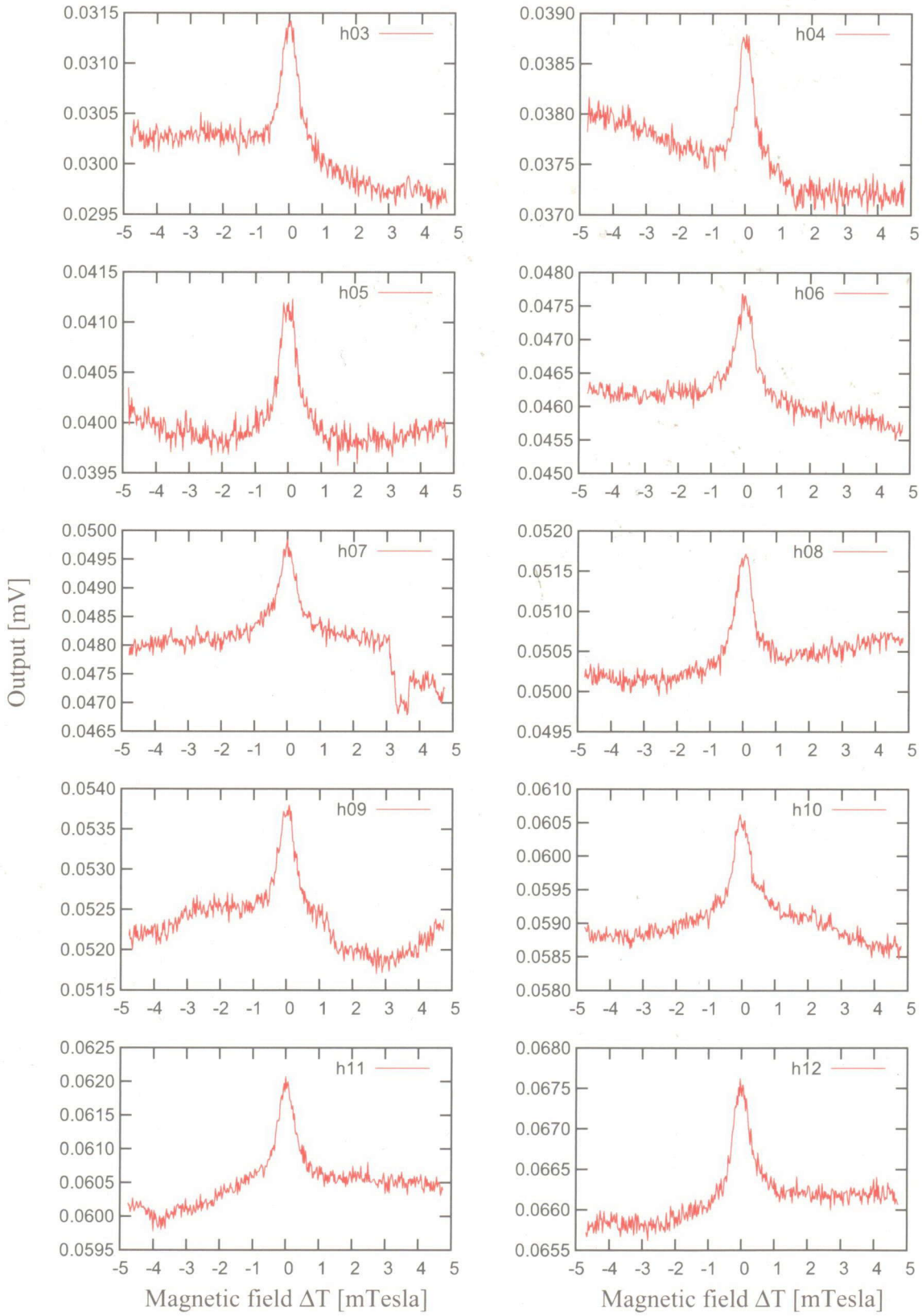

Figure 4.13: The NMR spectra obtained at 4.2 K without the HD target. The position of the magnetic field and the phase is adjusted. The NMR spectra h13,h15,h17,h19 and h21 runs are obtained at upward of the magnetic field. The NMR spectra h14,h16,h18,h20 and h22 runs are obtained at downward of the magnetic field.

Figure 4.14 shows summed NMR spectrum measured at 4.2 K with the HD target . The spectrum are sharply-peaked compared with the NMR resonance measured at 4.2 K without the HD target. It would appear that a sharply-peaked spectrum of 0.68 mol HD is superimposed in a broadly-peaked spectrum. There is no difference between "Upward" and "Downward" spectrum. A peak height is 0.013 and FWHM is 0.95 mTesla calculated by Gaussian fitting.

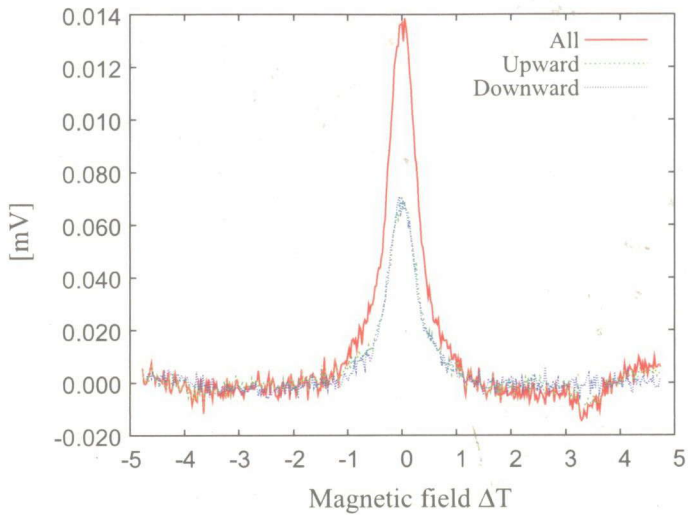

Figure 4.14: A summed NMR spectra obtained in the h23~h31 runs measured at 4.2 K with the HD target. The green line shows the NMR spectrum measure under the condition in which the magnetic field is changed upward. The blue line shows the NMR spectrum measured under the condition in which the magnetic field is changed downward. The red line shows the summed NMR spectrum.

The summed NMR spectrum was fitted by polynomial or linear function for the background and Gaussian function for the NMR spectrum. The NMR strength is obtained by integration the NMR spectrum. Figure 4.15 is shown fitted NMR spectra and statistical information. Table 4.7 is shown a result of summed peak areas A result of summed peak areas is listed in Table 4.7.

Table 4.7: Obtained peak areas in various fittings for data taken at 4.2 K without the HD target.

	All [mV]	Upward [mV]	Downward [mV]	Linear [mV]	Fitting region [mV]	
					350 points	300 points
Summed area	0.426	0.218	0.211	0.580	0.381	0.333
Statistical error	±0.007	±0.005	±0.005	±0.006	±0.007	±0.004

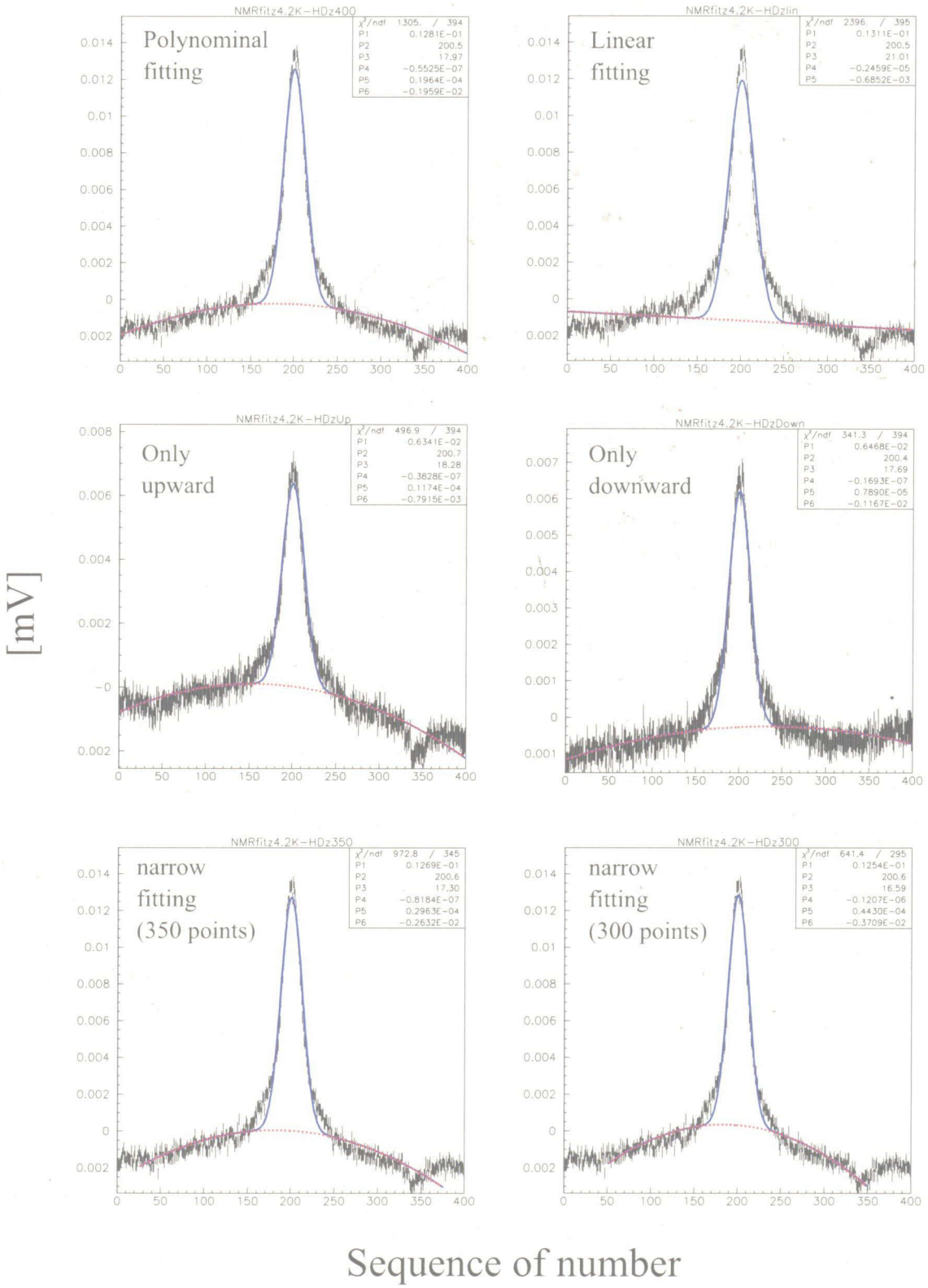

Figure 4.15: Fitting results of the NMR spectra obtained in the h13∼h22 runs measured at 4.2 K with the HD target.

Subtracted NMR spectrum for evaluation of contribution of only HD

We subtract the NMR spectrum at 4.2 K without the HD target from the NMR spectrum at 4.2 K with the HD target for evaluating the NMR strength of contribution of only HD. Figure 4.16 shows the NMR spectra of obtained 4.2 K without the HD target, the spectra of obtained at 4.2 K with the HD target and subtracted NMR spectra of them. The width of subtracted NMR spectra is narrower than NMR spectra of obtained 4.2 K without the HD target and NMR spectra of obtained 4.2 K with the HD target. We can consider the two meanings. One is that relaxation time T_1 is long and hydrogen molecular in the HD is fixed. The other HD was placed locally heterogeneous.

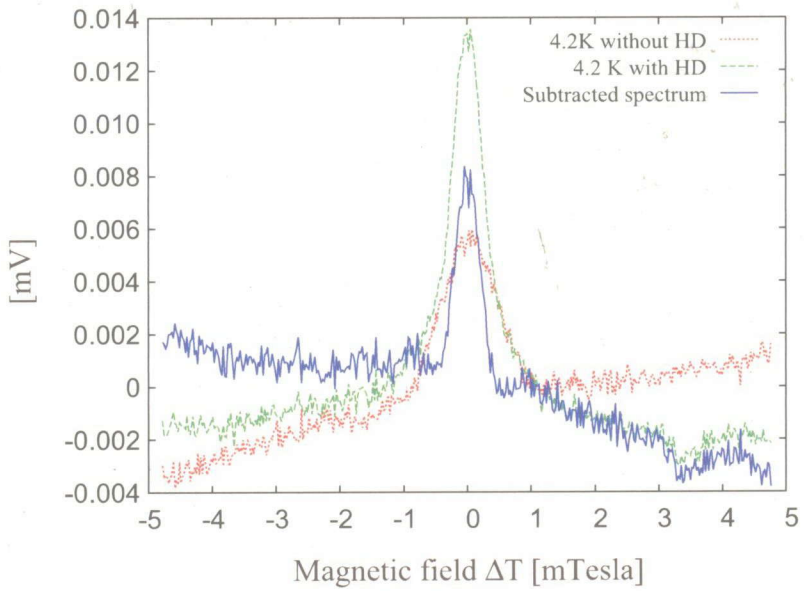

Figure 4.16: NMR spectrum subtracted from the NMR data obtained with the HD target to the NMR data obtained without the HD target at 4.2 K. Baselines of the NMR spectra is set to zero for comparison. The dotted line shows the NMR spectrum obtained at 4.2 K without the HD target. The dashed line shows the NMR spectrum obtained at 4.2 K with the HD target. The blue (solid) line shows the subtracted NMR spectrum.

We evaluate the peak area of subtracted NMR spectrum as shown in Fig. 4.17. Subtracted NMR spectrum were fitted by polynomial and Gaussian functions, respectively. The left panel shows fitting in the region of 400 points. The right panel shows fitting in the region of 300 points. Teble 4.8 shows the result of calculated area of NMR resonance. The areas are obtained 0.175±0.007 mV by fitting in the region of 400 points and 0.153±0.006 mV by fitting in the region of 300 points The calculated area by fitting in the region of 400 points is larger than that of fitting in the region of 300 points.

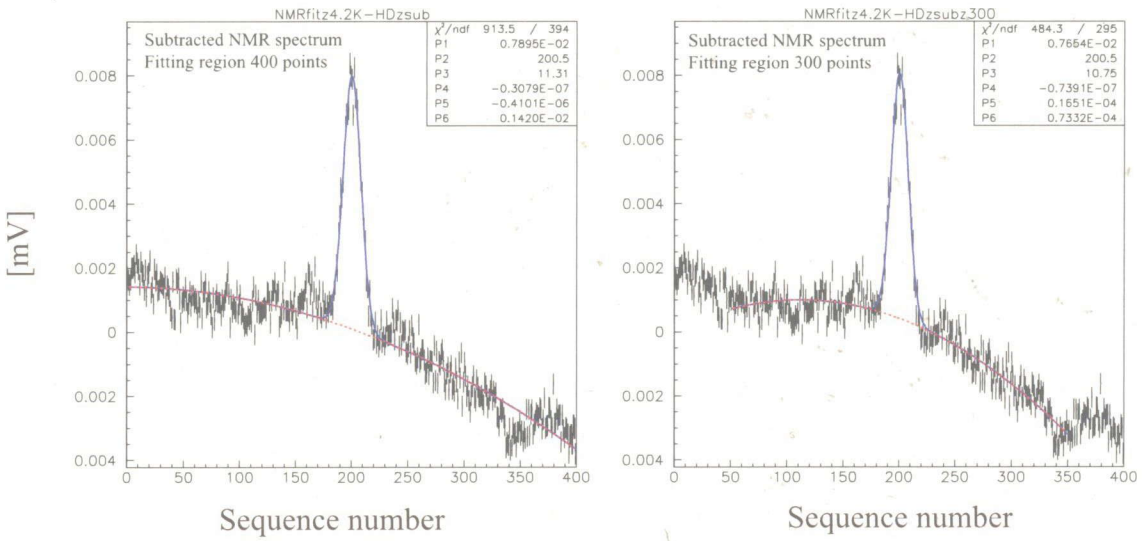

Figure 4.17: The fitting results for the subtracted NMR spectra. The left panel shows the results of fitting with 400 points. The right panel shows the results of fitting for the region of 300 points.

Table 4.8: Obtained the NMR peak areas in subtracted NMR resonance of the HD.

	Subtraction [mV]	
Fitting region	400 points	300 points
Summed area	0.175	0.153
Statistical error	±0.007	±0.006

— 4.3.3 Analysis of polarization signal of hydrogen —

In this analysis, we evaluate the polarization of H in the HD using by calibration signal. The NMR spectra were measured at 300 mK with the HD target after long aging time. A temperature was increased to 300 mK from 15 mK. Common parameters for measurement are shown in Table 4.9. A peak height and FWHM after the phase adjustment are obtained by polynomial function and Gaussian fitting. Table 4.10 shows the analysis result of measured NMR spectrum with analyzed filename. These spectrum were subtracted a off-set, adjusted the phase and positions to take the peak in the center. The NMR spectra, which were measured at 300 mK with the HD target, are shown in Fig. 4.18.

Table 4.9: Common parameters for data acquired at 300 mK with the HD target.

Frequency	Sweep region	Sweep speed	Level	phase
48.395 MHz	17.2 A⇔20.5 A	No.8 (300 A/200 min)	-8 dbm	0
filter slope	Time constant	Sensitivity	rate	sample
24 dB/oct	1 ms	10 mVrms / -47 dBm	80.000k	0.50k

Table 4.10: Analysis result of the NMR spectra obtained at 300 mK with the HD target after 53 days .

File name	Direction	Sampling speed			Phase [degree]	Height [mV]	Center [Tesla]	FWHM [mTesla]
		S/s	S/mTesla	mTesla/s				
h22	Upward	158.70	78.54	2.021	180.0	0.928	1.16325	0.743
h23	Downward	158.88	83.42	1.905	180.0	1.10	1.13920	0.615
h24	Upward	159.11	80.08	1.987	180.0	0.924	1.16327	0.731
h25	Downward	158.99	84.23	1.888	180.0	1.103	1.13926	0.609
h26	Upward	158.34	80.36	1.971	180.0	0.923	1.16327	0.728
h27	Downward	159.24	82.89	1.923	180.0	1.080	1.14020	0.618
h28	Upward	159.56	80.13	1.991	180.0	0.923	1.16320	0.730
h29	Downward	159.85	84.05	1.902	180.0	1.080	1.14023	0.612
h30	Upward	159.42	78.66	2.027	180.0	0.923	1.16316	0.746
h31	Downward	158.79	82.90	1.916	180.0	1.080	1.14012	0.618

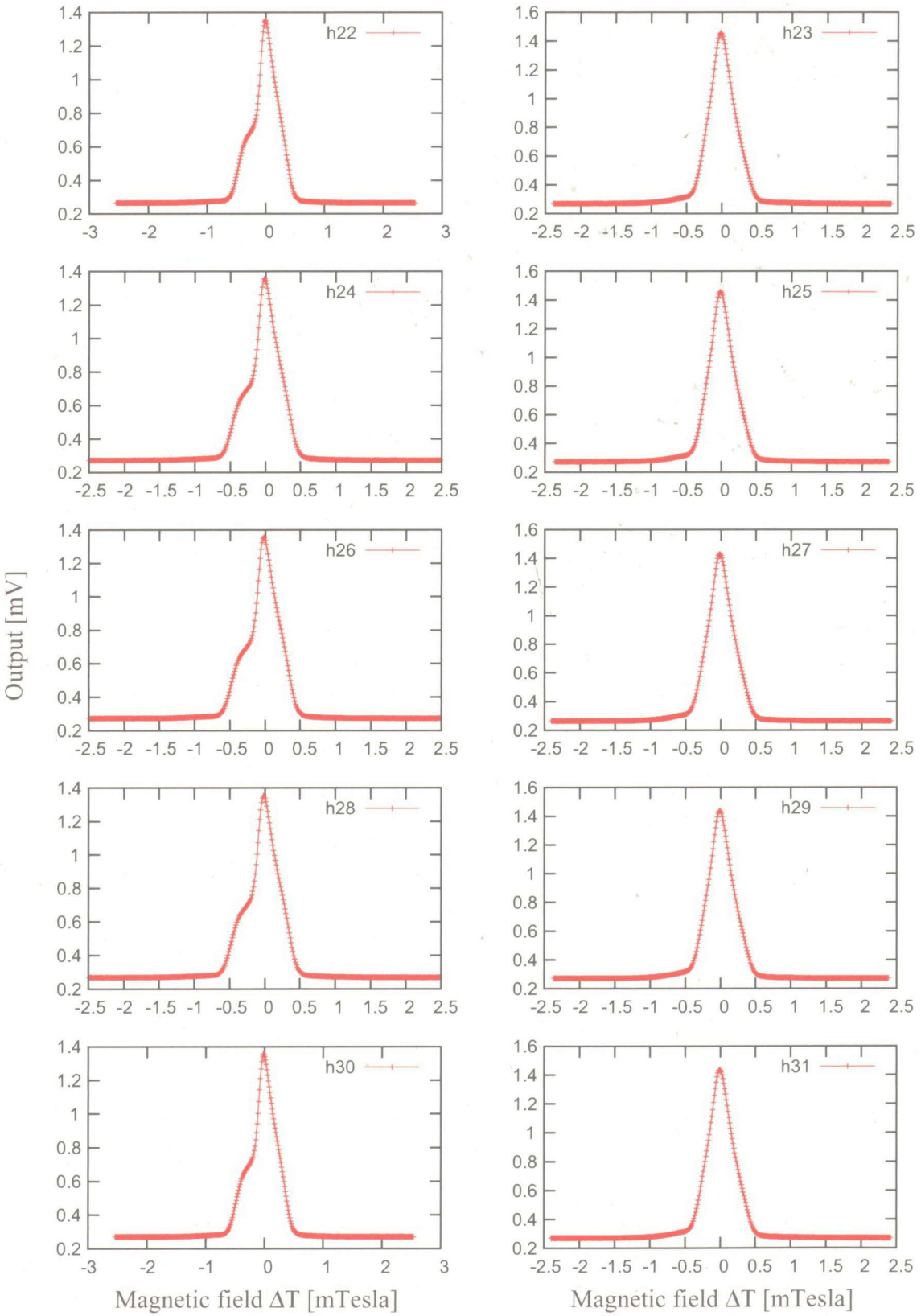

Figure 4.18: The NMR spectra obtained obtained at 300 mK with the HD target after 53 days. The NMR spectra h22,h2,h26,h28 and h30 runs are obtained at upward of the magnetic field. The NMR spectra h23,h25,h27,h29 and h31 runs are obtained at downward of the magnetic field.

Figure 4.19 shows summed NMR spectrum measured at 300 mK with the HD target. The shape of NMR resonance is difference between "Upward" and "Downward" spectrum. The NMR resonance of "Upward" is distorted and the NMR resonance of "Downward" is not distorted This distortion is due to homogeneity of magnetic field. This distortion is discussed in the later section. Height and FWHM of NMR resonance are 10.0 mV and 0.66 mTesla respectively. The area of NMR resonance is evaluated 419.81±0.02. This NMR spectra was measured at the beginning after the aging time of 53 days. This time was defined 0 hour. Next, we continued the NMR measurement to obtain the relaxation time T_1 of hydrogen in the HD.

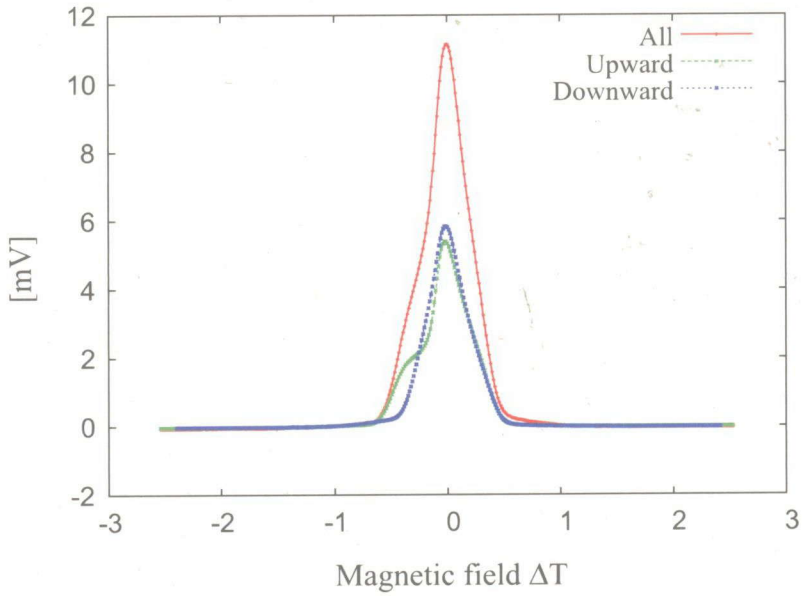

Figure 4.19: Summed NMR spectra obtained in the h23∼h31 runs measured at 300 mK with the HD target. The distortion of the NMR spectra is seen in "Upward. The distortion and difference is considered a cause of inhomogeneity of the magnetic field during a sweep.

Section 4.4

Evaluation of the relaxation time of hydrogen

To evaluate the relaxation time of hydrogen, the NMR spectrum was measured for two weeks. The NMR spectra were taken with 10 spectra as one group data set and summed at one measurement. The NMR spectrum is measured at 1.4, 17.3, 25.1, 45.4, 66.8, 97.2, 193.0, 265.1, 332.7 hours elapsed after the aging at 300 mK with 1 Tesla. Table 4.11 shows the result of summed area of the NMR spectra as a NMR strength with elapsed time. Hydrogen backgrounds contributed from the enamel wire of coil and grease are included in the obtained area. The relaxation time T_1 depends on a temperature, a strength of magnetic field and the structure of a material. A length of relaxation time T_1 of hydrogen backgrounds is unknown at 300 mK with 1 Tesla. We have to separate the decay of the NMR strength contributed from backgrounds and only HD. A contribution of these background is evaluated in fitting to the decay of the NMR strength.

Table 4.11: Summed area of the NMR spectra with elapsed time

Elapsed time		NMR strength	Statistical error
Hours	Days	[mV]	[mV]
0	0	419.81	0.02
1.4	0.058	419.89	0.02
17.3	0.72	413.75	0.03
25.1	1.05	415.44	0.02
45.4	1.89	407.60	0.02
66.8	2.78	403.80	0.02
97.2	4.05	399.26	0.02
193	8.04	387.93	0.03
265.1	11.05	380.04	0.02
332.7	13.86	364.45	0.01

To evaluate the relaxation time of only HD, The function $f(t)$ is defined as follows

$$f(t) = S_{BG}exp(-t/T_1^{BG}) + S_{HD}exp(-t/T_1^{HD}) \tag{4.3}$$

S_{BG} and S_{HD} are the contributions from backgrounds and only HD, respectively. T_1^{BG} and T_1^{HD} the relaxation time of backgrounds and only HD, respectively. The function $f(t)$ fitted to NMR strengths measured after the aging time as shown in

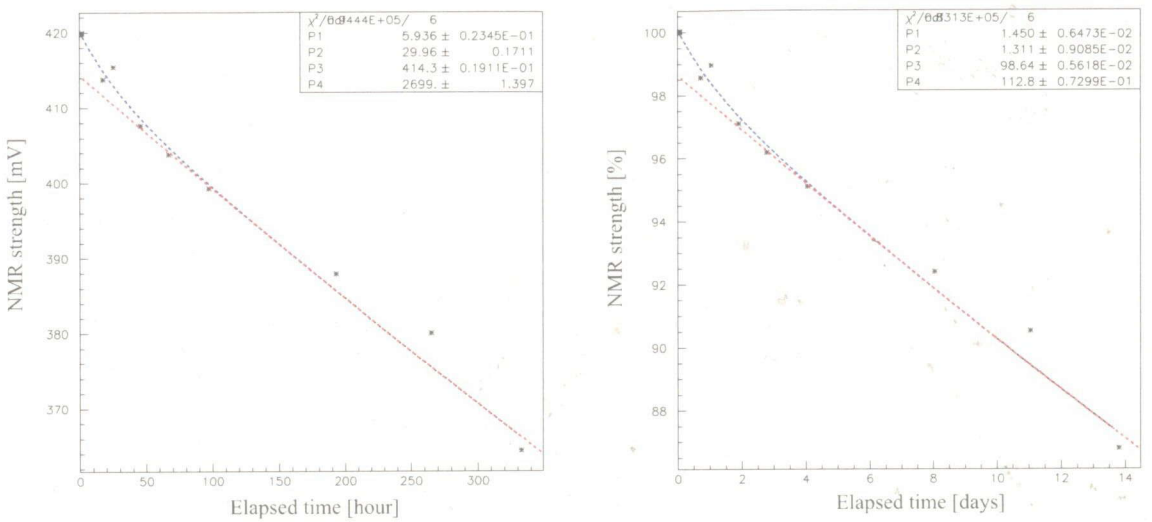

Figure 4.20: Fitting to a decay of the NMR strength of hydrogen in HD and background material. The left panel shows the obtained NMR strength by mV as a function of elapsed hours. The right panel shows obtained NMR strength by percentage as a function of elapsed days.

Fig. 4.20. The left panel shows the NMR strength as a function of the elapsed hours. The right panel shows the rate of decrease of NMR strength. The NMR strength decays quickly in the early measurement. This reduction is inferred to be due to the hydrogen background from the coil wire and from the grease. The relaxation time of the hydrogen in the HD target and background was obtained as listed in Table 4.12

Table 4.12: Summary of relaxation time.

	NMR strength [mV]	Relaxation time T_1 Hours	Days
Background	5.9±0.02	30.0±0.02	1.31±0.01
HD	414.3±0.02	2699±1	112.8±0.1

Section 4.5

Evaluation of polarization of hydrogen

From evaluation of relaxation time, the strength of NMR resonance was deduced to be 414.3 mV at the beginning after the aging time of 53 days. Since the back-

ground and calibration signals were evaluated previously, a polarization of HD was calculated as listed in Table 4.13. Polarization of hydrogen in the HD was evaluated by many methods. The magnetic field was 1.135 Tesla. The calibrating polarization is calculated 0.0276% at 4.2 K. A sampling speed per magnetic sweep speed (S/mTesla) is different between the calibration measurement at 4.2 K and the polarization measurement at 300 mK. The sampling speed per magnetic sweep speed at 4.2 K is 42.2 S/mTesla. The sampling speed per magnetic sweep speed at 300 mK is 82.5 S/mTesla. By taking into account the different factors of sampling speed per magnetic sweep speed, the polarization of the HD target after the aging is calculated as follows,

$$\text{Polarization} = \frac{\text{Evaluated NMR strength of HD at 300 mK}}{\text{Calculated NMR strength of HD at 4.2 K}} \times 0.0276\% \times \frac{42.2}{82.5}. \tag{4.4}$$

We obtained the polarization of 40.8±2.3(stat)% from the result of the analysis.

Table 4.13: Obtained peak area in the NMR spectrum in many analyses.

	All [mV] 400 points	Upward [mV] 400 points	Downward [mV] 400 points	Linear [mV] 400 points
(1) 4.2 K noHD	0.283±0.004	0.149±0.003	0.136±0.003	0.336±0.005
(χ^2/ndf)	(0.854)	(0.518)	(0.370)	(1.082)
(2) 4.2 K HD	0.426±0.007	0.218±0.005	0.0211±0.005	0.580±0.006
(χ^2/ndf)	(6.06)	(1.413)	(0.866)	(6.06)
(1)-(2)	0.143±0.008	0.069±0.006	0.075±0.006	0.244±0.008
(χ^2/ndf)	(—)	(—)	(—)	(—)
Polarized HD	414.3±0.2	210.5±0.2	205.8±0.2	414.3±0.2
Polarization	40.8±2.3%	43.0±3.6%	38.7±3.0%	23.9±0.7%

	Fitting region [mV]		Subtraction [mV]	
	350 points	300 points	400 points	300 points
(1) 4.2 K noHD	0.286±0.004	0.288±0.004	—	—
(χ^2/ndf)	(0.686)	(0.724)	(—)	(—)
(2) 4.2 K HD	0.386±0.009	0.381±0.007	—	—
(χ^2/ndf)	(2.81)	(2.17)	(—)	(—)
(1) -(2)	0.100±0.010	0.0931±0.008	0.175±0.007	0.153±0.006
(χ^2/ndf)	(—)	(—)	(2.31)	(1.64)
Polarized HD	414.3±0.2	414.3±0.2	414.3±0.2	414.3±0.2
Polarization	58.1±5.8%	62.7±5.0%	33.3±1.3%	38.2±1.5%

Section 4.6

Distortion of NMR spectra

The most likely explanation of the distortion of the NMR peak shape obtained at 300 mK is due to the inhomogeneity of the local magnetic field in a superconducting solenoid magnet. We reproduced the H- and D-NMR peak shapes by the simulation. This simulation considers only the inhomogeneity of the local magnetic field in a superconducting magnet. The inhomogeneity of x and y axis are not taken into account. We wants to show that the inhomogeneity of the local magnetic field is strong enough to distort the NMR shape in this section. The most important point is, "even if the NMR spectrum is distorted by the inhomogeneity of the local magnetic field, the peak area will not be changed.".

There are some questionable points in the simple simulation. First, the target cell length of HD target is probably not 50 mm. In normal case, one mole HD is put in empty cell; if the HD is filled tight, the cell length is 50 mm. In case of HD target, there is only 0.68 mole HD; therefore the cell length may be only 34 mm if the HD is filled tight. It is also possible that the HD was not filled tight so that the possible cell length is from -38 mm to 28 mm. The cell position and cell length are assumed -5 mm and 50 mm, as shown in Fig. 4.21. But the simulation result is not locates in good agreement with the real spectrum; therefore the chi-square is large. The "most likely" result is not so trusty.

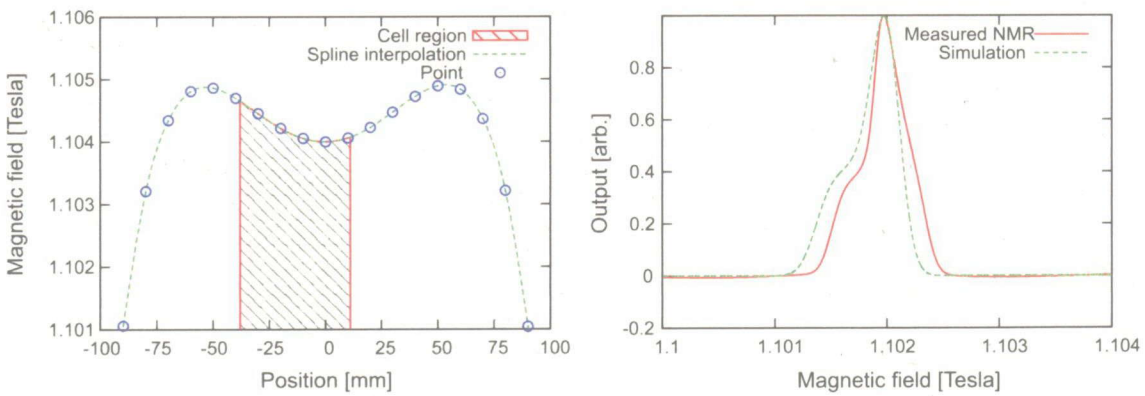

Figure 4.21: The simulation for the distortion of NMR spectrum by the inhomogeneity of the superconductor magnet. Left:A setup condition of magnetic field and target position. Right:A simulated NMR spectrum with a measured one.

Section 4.7

Discussion about polarization and relaxation time

In the first production for the polarized HD target, we obtained the polarization value of 40.8±2.3 (stat.)% and the relaxation time of 112.8±0.1 (stat.) days. The obtained polarization is lower than the expected polarization obtained at 14 mK and at 17 Tesla. The LEGS group who has developed a polarized HD target in USA succeeded to make the polarized HD target with the polarization of ~60% and the relaxation time longer than one year as listed in Table. 4.14.

Table 4.14: The polarization, the relaxation time and the aging time of the polarized HD target at RCNP and at LEGS group in USA. $[H_2]$, [HD] and $[D_2]$ is concentrations in the HD gas.

	RCNP (2009)	LEGS (2007)
Polarization	40.8±2.3(stat.)%	~60%
Relaxation time	112.8±0.1(stat.) days	$\geq$ 1 year
Aging time	53 days	3 months
$[H_2]$	1.26%	0.4%
[HD]	96.67%	99.2%
$[D_2]$	2.07%	0.4%

— 4.7.1 Discussion about polarization —

The measured polarization of 40.8±2.3% is lower than the expected polarization of 84%. Possible explanations for the low polarization degree are as follows,

1. Linearity between the polarization degree and the peak area in the NMR spectrum might be bad in case of high polarization.
2. There only remain extremely small amounts of ortho-H_2 and para-D_2 component in the purified HD gas.

In the analysis of the NMR spectra, there may be a systematic error due to hydrogen background except for the HD, and due to the drifting of the baseline. In the measured NMR spectra, there is a background signal of hydrogen. The hydrogen background except for the HD came from the enamel wire and the grease which was used for seal between a pipe for installation of the HD gas and a cell. A width of

the NMR peak due to the background is larger than that of HD. This means that sources of the background are widely-distributed materials. The NMR strength of the background is larger than that of 1 mol HD. Since the background signal affects to the systematic error for the polarization of HD, the background is desired to remove as much as possible.

Suppression of a drift and noise at NMR measurement

A baseline drifts in the measurement of the NMR spectrum. When a peak in the NMR spectrum is detected, the drift and large noise affect the NMR peak shape. The NMR spectrum is complex function which convolves from a Lorentz function and from the magnetic inhomogeneity. The function of the NMR peak shape is uncertain. The effect makes analysis complex and becomes a major contributing to systematic error. It is important to suppress a drift and noise for evaluating the polarization clearly.

Uncertainty of the amount of o-H_2

Extremely small amounts of ortho-H_2 and para-D_2 component in the purified HD gas have a possibility not to grow the polarization of the HD target. The polarization does not grow to the maximum value, if T_1 was very long at the beginning. The HD gas before pouring in the DRS was distilled for ~30 days. The o-H_2 is convert to the p-H_2 in 6.5 days. The concentration of o-H_2 decreases to 1/100 for after 30 days. The concentration of o-H_2 might convert to o-H_2 mostly.

— 4.7.2 Discussion about relaxation time —

The polarization of H decreases 1% a day when the relaxation time is 112.8 days. If we will continue the aging process of polarization HD for 3 months, the relaxation time may close with one year. By controlling the o-H_2 in the HD target at the initial process, we get the polarized HD target with a longer relaxation time. Extremely low o-H_2 contaminations in the HD target may prevent the growth of polarization of H.

70 events of ϕ photoproduction can be collected in a day. We require 2000 events×2 sets for 10% accuracy measurement of C_{BT}. Days required for the measurement are ~60 days. The relaxation time of 112.8±0.1 days is enough for the experiment of evaluation of $s\bar{s}$. If the relaxation time is one year, decreasing of polarization becomes 15%.

Part II

Improvement I

PXI-NMR

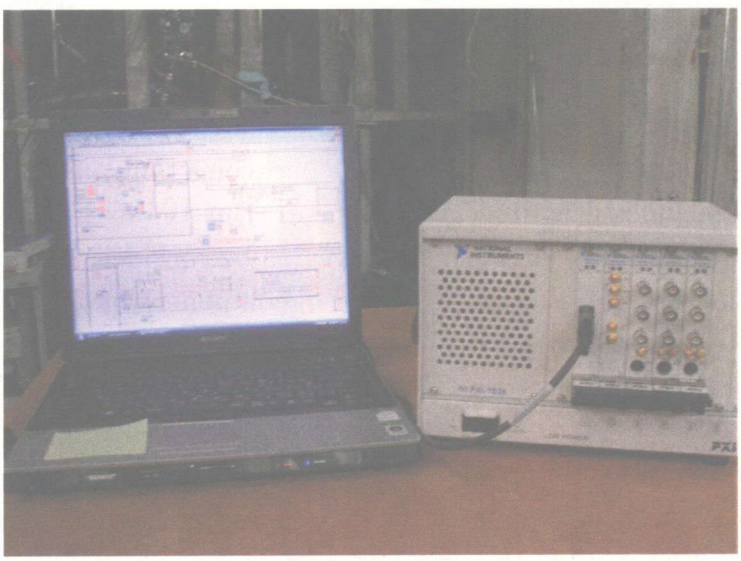

Portable NMR measurement system

Chapter 5

Improvement of NMR measurement

In this chapter, the improvement of the NMR measurement system is explained firstly, the improvement of eliminating the hydrogen background and the instability of baseline of the NMR spectra are discussed. Next, the portable NMR system required for the transportation of the polarize HD target is discussed.

Section 5.1

Elimination of the background of hydrogen

— 5.1.1 Simulation for magnetic field of coil by TOSCA —

We have observed the hydrogen peak in the NMR measurement without the HD at 4.2 K. The background was not explained. When the HD gas was poured to the HD cell, a grease was used to seal the pipe line between a tank and the cell. We knew that the grease includes a hydrogen component. But the hydrogen component of grease was thought to be out of a detectable region by considering the coil geometry. Although the amount of the included hydrogen component of the grease was much smaller than 1 mol for HD, the strength of the NMR strength was larger than the strength of 1mol HD. The coil wire, which is coated with enamel, includes a hydrogen component.

We simulated the magnetic field generated from the coil by using the TOSCA provided by OPERA-3d (an OPerating environment for Electromagnetic Research and Analysis). OPERA-3d is the pre- and post-processing system for well-known electro- magnetics analysis programs. These programs provide facilities for the creation of finite element models, specification of complicated conductor geometry, definition of material characteristics including for example, non-linear and anisotropic descriptions and graphical displays for examination of the data. The TOSCA solves non-linear magneto-static or electro-static field and current flow problems in three dimensions. It has been in use for many years, but is being continually improved to increase its accuracy and efficiency.

Figure 5.1(a) shows a designed model in TOSCA. The designed model precisely reproduces the structure and style of the coil for the NMR measurement of HD. Figure 5.1(b) shows the result of simulation for magnetic strength in the Y direction

(B_Y) on the XY plane at the center of the coil and target for the vertical axis. One can see that the magnetic field is strong around the wire. The strength of the magnetic field around the wire and the center of the coil is 2×10^{-6} gauss and 5×10^{-8} gauss, respectively. These data show that magnetic field around the wire is about 40 times stronger than that around the cell. Figure 5.1(c) shows the strength of the magnetic field of Y direction (B_Y) in the plane of cell.

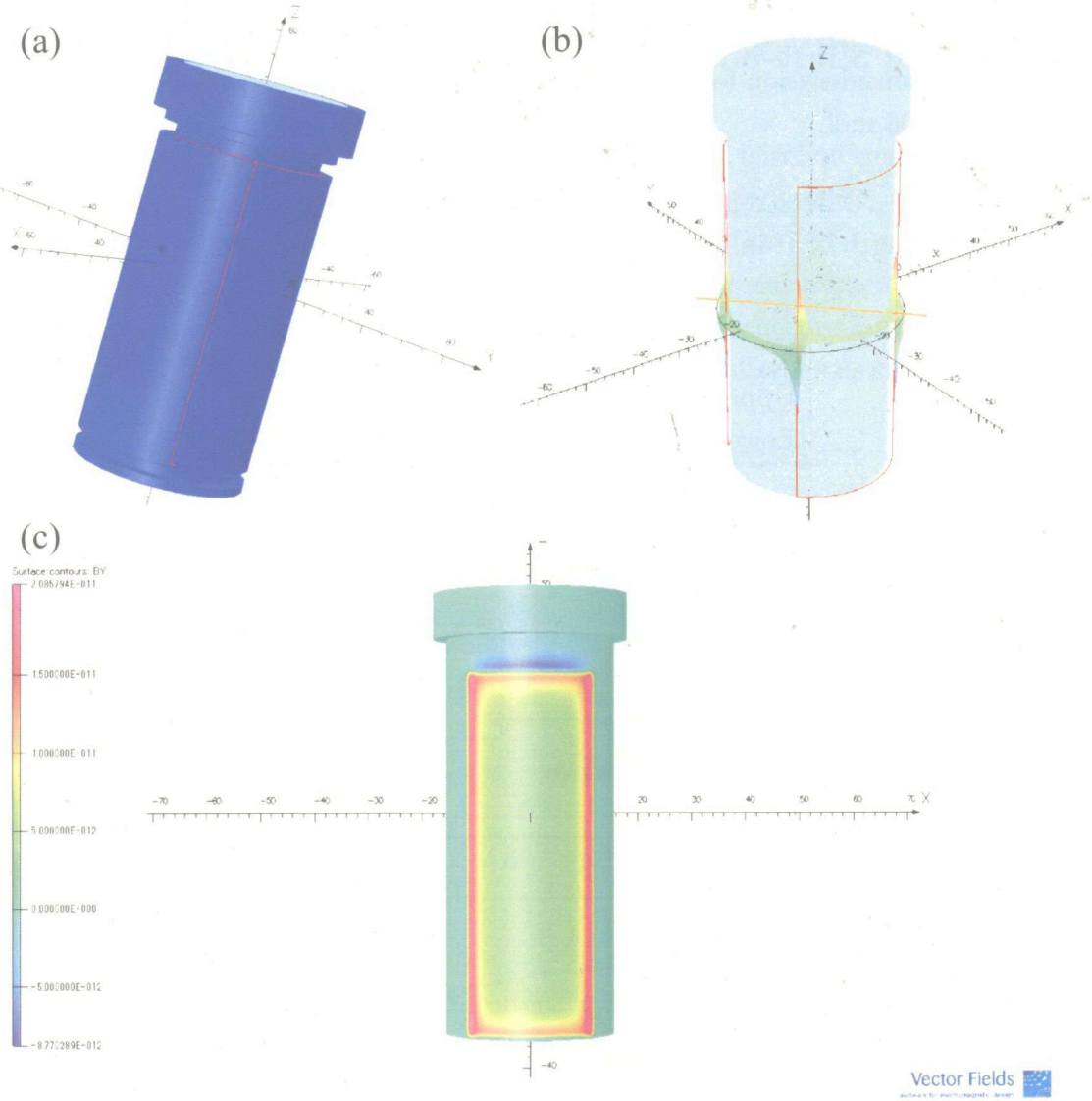

Figure 5.1: A magnetic strength simulation by TOSCA (a) A deigned model in TOSCA. (b) A simulation for magnetic strength of Y direction (B_Y) at the center of coil and target for the vertical axis. The strength is mapped on the XY plane . The red color indicates a high magnetic field. (c) A simulation for Magnetic strength of Y direction (B_Y) on surface of the cell as contours. The red color indicates a high magnetic field.

We replace the coil wire from the copper wire coated by enamel to silver wire coated by PCTE(Teflon). And then we performed a comparison test of 2 type wires. Figure 5.2 shows the measured NMR spectrum with HD and without HD. Upper panel was plotted the data measured at 4.2 K with 1.14 mol HD. Fluorine peak and obvious hydrogen peak is seen in upper panel. Lower panel was plotted the data measured at 4.2 K without HD. The NMR peak of hydrogen is not seen. We calculated NMR strength from the measured NMR spectrum as shown in table 5.1. From NMR strength of hydrogen, lower limit of amount of hydrogen is 0.07 mol. And then, in consideration for the NMR strength of fluorine, a low limit of hydrogen is less than 0.06 mol.

Table 5.1: The NMR strength calculated from the NMR spectrum for H and F. The NMR strength of H in the lower panel in Fig 5.2 is calculated from the drift of baseline.

	H	F
Upper panel	3.023 mV	9.022 mV
Lower panel	$\leq$0.192 mV	7.796 mV

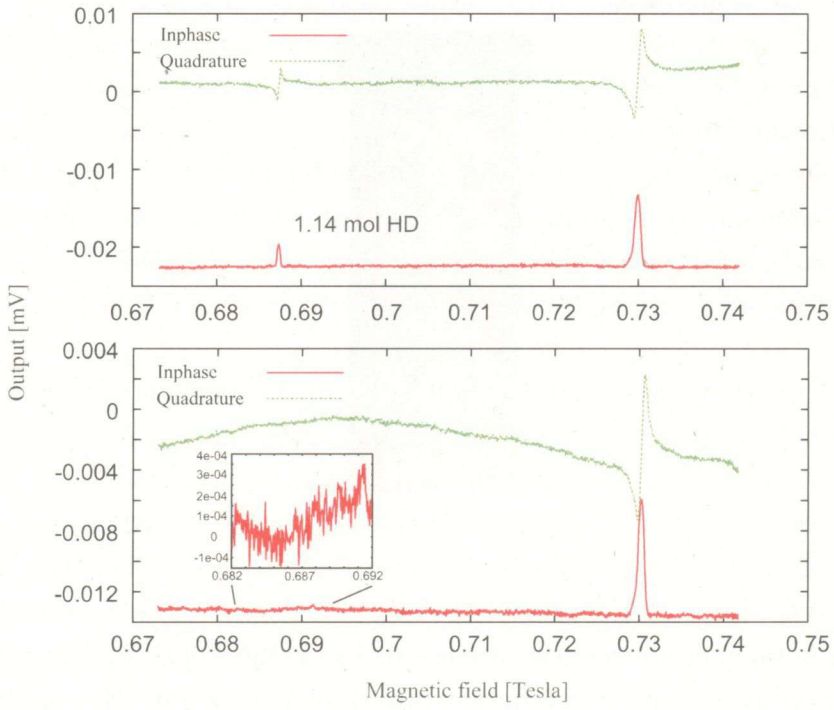

Figure 5.2: Comparison of NMR spectra including and removing enamel wire. Upper panel shows the NMR spectra including enamel wire. Lower panel shows the NMR spectra removing enamel wire.

Section 5.2
Improvement for drift and noise of baseline

— 5.2.1 Temperature control by thermo-static box —

From the NMR measurements, the drift and noise of baseline make the analysis unstable. We have tried to reduce the drift and noise of baseline. These may be caused from a fluctuation of temperature of cables for the NMR polarimeter. We made a thermo-static box and put a part of the NMR measurement system in the thermo-static box. The temperature of the Magic Tee, the pre-amp and the tune circuit was adjusted to a constant value in the thermo-static box as shown in Fig 5.3.

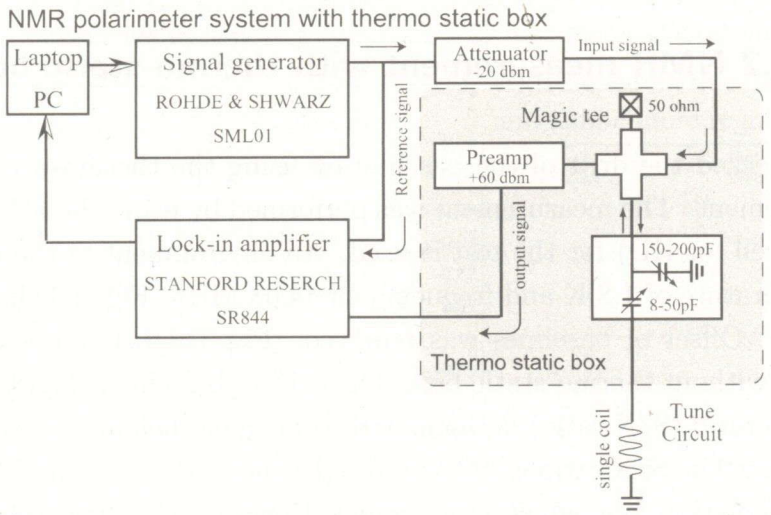

Figure 5.3: The NMR measurement system with the thermo-static box. The Magic Tee, the pre-amp and the tune circuit were installed in the thermo-static box.

Fig. 5.4 shows the scheme of the system of the thermo-static box. The box is made of aluminum with a height of 110 mm, a width of 330 mm and a depth of 330 mm. A silicon rubber heater is attached at the side of the box. The voltage of the silicon rubber heater is provided by the AC source. Furthermore, the thermo-static box is covered by foam polystyrene to increase the stability of temperature. The controller controls the solid state relay by switching the input power between on and off to set a purpose of the temperature of platinum resistance thermo-sensor pasted in the rubber heater for adjusting the temperature of rubber heater. The temperature of the static box is monitored by a thermistor.

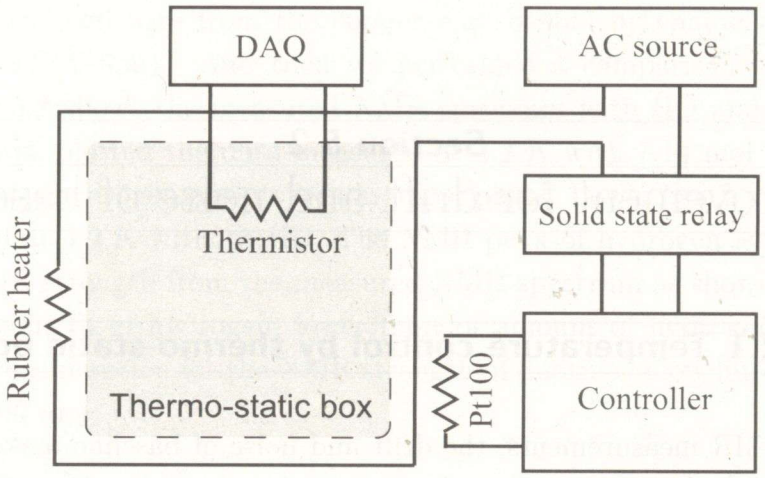

Figure 5.4: Scheme of the system of the thermo-static box. Pt100 is platinum resistance thermo-sensor monitored in the box

— 5.2.2 NMR measurement with thermo-static box —

We have checked the drift of the baseline by using the thermo-static box in the NMR measurement. The measurement was performed by using the SC. A small type cell (0.1 mol cell for HD) for the test is used. An environment of the measurement was the temperature of 1.8 K and frequency of 44.08 MHz. Fig. 5.4 shows the NMR spectra of ^{19}F. Offset of baselines was removed. Fig. 5.4 (a) shows the measured NMR spectra without thermo-static box. The drift of baseline is highly visible. The signal to noise ratio (S/N ratio) is calculated from signal height and noise including a drift of signal. The S/N ratio is 21. Fig. 5.4 (b) shows the measured NMR spectra with the thermo-static box which was opened. However, the drift of baseline is not visible, the baseline has a gradient. The S/N ratio is 207. Fig. 5.4 (c) shows the measured NMR spectra with the thermo-static box which was closed and warmed up to 40°C. The baseline was very stable. The S/N ratio is 251.

From these results, the drift of baseline is suppressed only in case that the thermo box was closed. S/N ratio was improved more than 10 times. Although there is the gradient in the baseline in the long span, the gradient is suppressed by closing the thermo box and by adjusting the temperature. The temperature adjusting of the NMR circuit was very effective for the drift suppression of the baseline. The temperature adjustment of coaxial cables may also be effective.

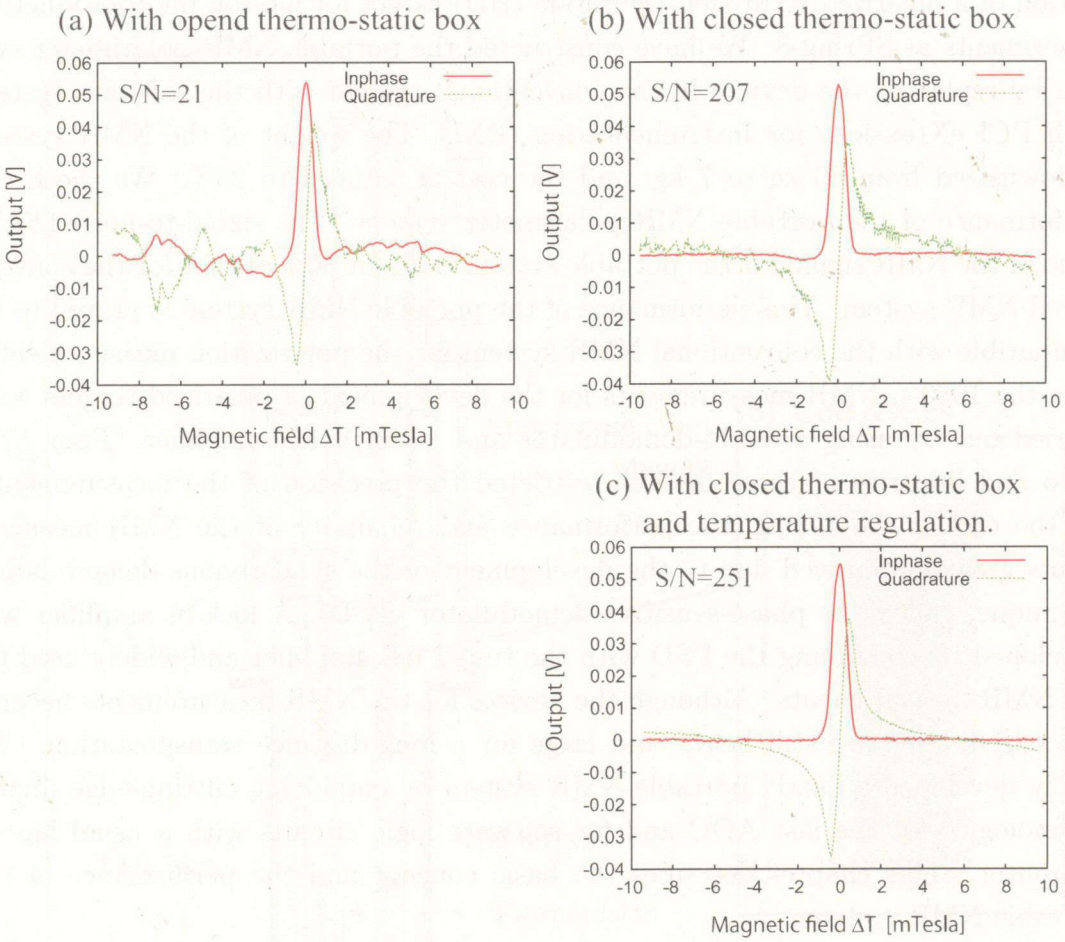

Figure 5.5: The measured NMR spectra with thermo-static box. (a) The NMR spectra with opened thermo-static box. (b) The NMR spectra with closed thermo-static box. (c) The NMR spectra with closed thermo-static box and temperature regulation.

Section 5.3
PXI-NMR

A portable NMR polarimeter system has been developed to measure the polarization of a polarized Hydrogen-Deuteride (HD) target for hadron photoproduction experiments at SPring-8. We have constructed the portable NMR polarimeter system by replacing the devices in the conventional system with the software system with PCI eXtensions for Instrumentation (PXI). The weight of the NMR system is downsized from 80 kg to 7 kg, and the cost is reduced to 25%. We check the performance of the portable NMR polarimeter system. The signal-to-noise (S/N) ratio of the NMR signal for the portable system is about 50% of that for the conventional NMR system. This performance of the portable NMR system is proved to be compatible with the conventional NMR system for the polarization measurement.

In the 1960's, NMR measurements for the development of polarized targets were carried out by using a diode demodulator and a tuned RF amplifier. Poor S/N ratio and linearity of these devices restricted the precision of the measurements. At the end of the 1960's, the performance and reliability of the NMR measurements greatly improved due to the development of the synchronous demodulation technique, called the phase-sensitive demodulator (PSD). A lock-in amplifier was developed by combining the PSD with the tuned RF amplifier and widely used for the NMR measurements. Although the devices for the NMR measurements become downsized, they are still heavy and large for a long-distance transportation. We newly developed a handy portable NMR system by employing cutting-edge digital technologies for the fast ADC and for software logic circuits with a usual laptop computer. This chapter describes the basic concept and the performance of the portable NMR system.

Section 5.4
Polarization measurement method

Fig. 5.6(a) schematically shows the storage cryostat (SC) which is used for solidifying HD and for keeping the polarization of the HD target during the transportation from RCNP to SPring-8. The SC mainly consists of liquid nitrogen (LN_2) bath, liquid helium (LHe) bath, and a superconducting magnet. The SC is equipped with a needle valve to control the HD temperature in the range of 1.5-30 K by pumping evaporated He gas from the LHe bath. The superconducting magnet cooled by LHe provides the maximum magnetic field of 2.5 T. The homogeneity $\Delta B/B$ of the

magnetic field is 1.0×10^{-4} over the target cell region. The HD gas is solidified in a cell made of Kel-F (PCTFE:Poly-Chloro-Tri-Fluoro-Ethyle) without hydrogen composition.

The set-up of the coil support frame around the target cell in the SC is shown in Fig. 5.6(b). We apply a single coil method for NMR measurements [60, 61]. A Teflon coated silver wire with a diameter of 0.1 mm is wounded as a saddle coil by 1 turn on the coil support frame which is also made of Kel-F/PCTFE.

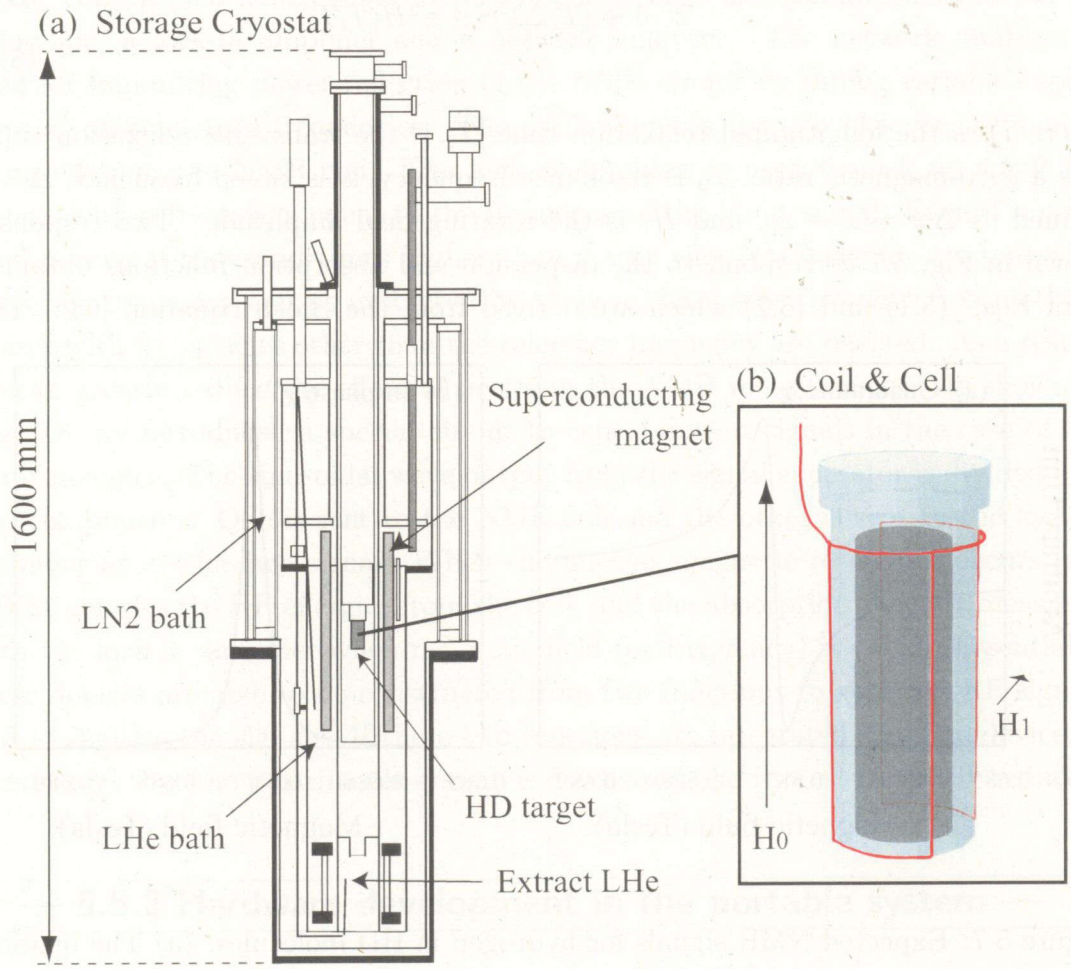

Figure 5.6: (a) The structure of the storage cryostat (SC) produced by Oxford Instruments and (b) the details of the HD cell, coil, and its support frame. The geometry of the HD target cell is 2.5 cm in diameter and 5 cm in length for the LEPS experiments. The coil winding is illustrated with the directions of the magnetic field H_0 of the superconducting magnet and the applied RF field H_1.

The polarization of a nucleus with a spin of 1/2 is defined as $P = (N_+ - N_-)/(N_+ + N_-)$, where N_+ and N_- are the numbers of sub-states $m = +1/2$ and $m = -1/2$, respectively. The absorption strength of the RF power in the NMR coil is proportional to magnetization which is also proportional to the polarization [62]. Therefore, the

proportionality between the polarization and the absorption strength can be used for determining the polarization degree.

The details about the NMR absorption functions are given by Abragam [62]. The susceptibility $\chi = \chi' - i\chi''$ is defined by the two functional forms as

$$\chi' = -\frac{1}{2} \cdot \frac{\omega_0 \Delta\omega T_2^2}{1 + (T_2\Delta\omega)^2 + \gamma^2 H_1^2 T_1 T_2} \tag{5.1}$$

$$\chi'' = \frac{1}{2} \cdot \frac{\omega_0 T_2^2}{1 + (T_2\Delta\omega)^2 + \gamma^2 H_1^2 T_1 T_2}, \tag{5.2}$$

$$\tag{5.3}$$

where T_1 is the longitudinal relaxation time, T_2 is the transverse relaxation time, γ is a gyro-magnetic ratio, ω_0 is resonance frequency, ω is sweep frequency, $\Delta\omega$ is defined as $\Delta\omega = \omega - \omega_0$, and H_1 is the rotating field amplitude. Two responses shown in Fig. 5.7 correspond to the dispersion and absorption functions obtained from Eqs. (5.1) and (5.2) which are derived from the Bloch equation [63]. The

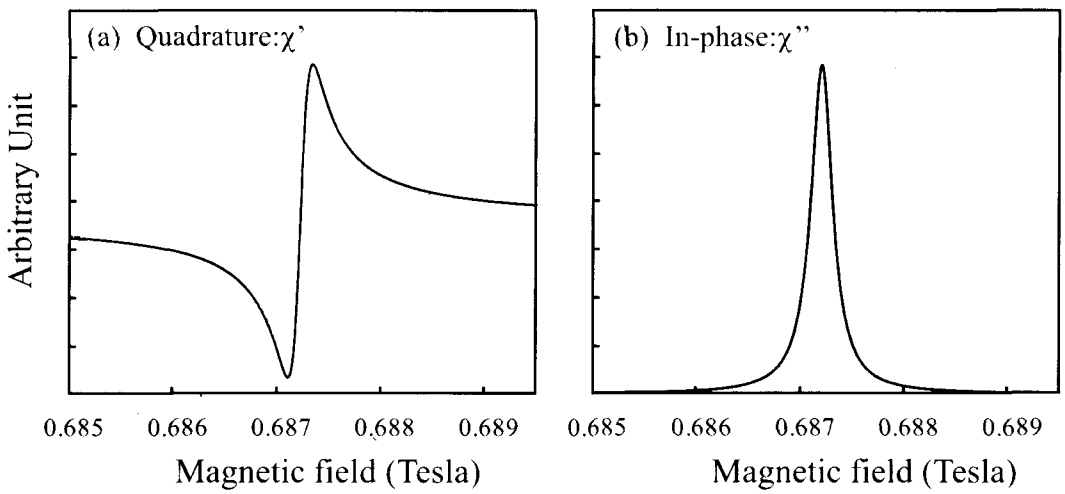

Figure 5.7: Expected NMR signals for hydrogen in HD molecules. (a) The quadrature signal corresponds to the dispersion function given in Eq. (5.1). (b) The strength of in-phase signal proportional to the polarization degree which corresponds to the absorption function given in Eq. (5.2). These NMR signals are simulated under the condition that the frequency is fixed at 29.26 MHz, the magnetic field is swept from 0.67 to 0.75 Tesla, and T_1 and T_2 are assumed to be 1 second.

polarization of the target is proportional to the strength of the absorption function χ''. Thus polarization P can be expressed as follows [64, 65, 66].

$$P \sim \int_0^\infty \chi''(\omega) d\omega. \tag{5.4}$$

Section 5.5
Development of the portable NMR polarimeter system

— 5.5.1 Hardware in the conventional system —

The conventional NMR polarimeter system consists of a signal generator, an oscilloscope, a lock-in amplifier and a network analyzer. The network analyzer is used for minimizing power reflection of the NMR circuit by tuning variable capacitors at off-resonance frequencies. The oscilloscope is used to observe the signals returned from the NMR coil. The lock-in amplifier is used to pick up small RF signals with a frequency equal to the frequency of the input signal. Even if a noise level is several thousand times higher than a true tiny NMR signal, a signal with a specific frequency can be extracted by using a phase sensitive detection method. Noises with frequencies other than the reference frequency are rejected. As a result, we can greatly reduce the effect of noises in the NMR measurement. As shown in Fig. 5.8, we introduced a special circuit to cancel output signals in the case of the non-resonance. The sinusoidal wave output from the signal generator is divided into two components. One is sent to the NMR coil and the other is sent to the lock-in amplifier as a reference signal. When the nuclear magnetic resonance occurs, the HD target absorbs RF energies from the coil, and the absorption signal is measured with the lock-in amplifier when magnetic field (or frequency) is swept. Essentially, these devices are able to be constructed from two functions to generate RF signals and to digitize the signals. If these two functions are integrated into one device, it is expected that the polarimeter system is downsized and its cost is greatly reduced.

— 5.5.2 Hardware development in the portable system —

We have constructed the portable NMR polarimeter by using "PCI eXtensions for Instrumentation (PXI)" [67]. This system consists of PXI-1036 (chassis), PXI-8360 (connection between PC and PXI), PXI-5404 (signal generator), and PXI-5142 (ADC) which are produced by National Instruments Company. The hardwares used in the present work are listed in Table 5.2. The aforementioned functions necessary for NMR measurements are virtually implemented and are realized using the LabVIEW software. The schematic drawing of the portable NMR polarimeter system is shown in Fig. 5.9. Fig. 5.10 shows the photographs of the conventional and portable NMR systems. Table 5.3 compares some specifications of the conventional and portable NMR systems. Downsizing the weight of the NMR system from 80 kg to 7 kg and reducing the cost to 25% were successfully achieved.

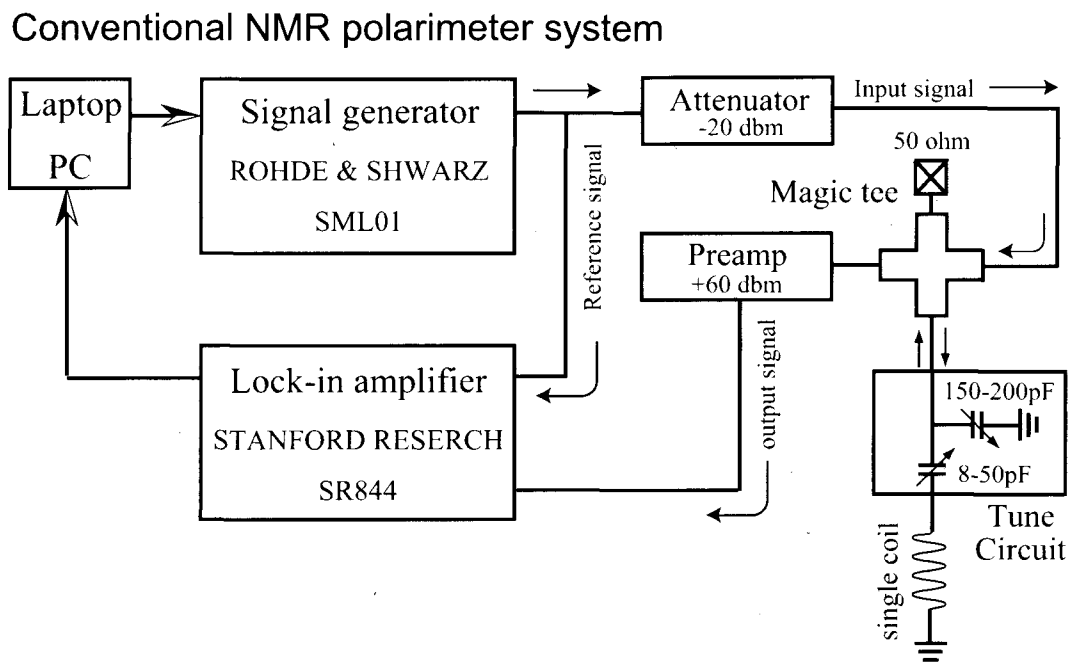

Figure 5.8: Schematic drawing of the conventional NMR polarimeter electronics.

Table 5.2: Hardware of the portable NMR polarimeter system

Product name	Function	Specification
PXI-1036	Chassie	host 1slot, module 5slot
PXI-8360	PCI bus	throughput 110MB/s
PXI-5404	Signal generator	16bit, 0-100MHz
PXI-5142	ADC	14bit, 2GS/s

Table 5.3: Comparison of weight, size, and cost for the conventional and portable NMR systems. The width, depth, and height of the conventional system are 500 mm, 500 mm and 1000 mm, respectively. Those of the portable system are 200 mm, 200 mm and 250 mm, respectively. The total sizes are compared in percentage. The weight of the portable NMR system does not include the laptop PC

	weight	size	cost
Conventional system	80 kg	100%	$60,000
Portable system	7.1 kg	4.0%	$15,000

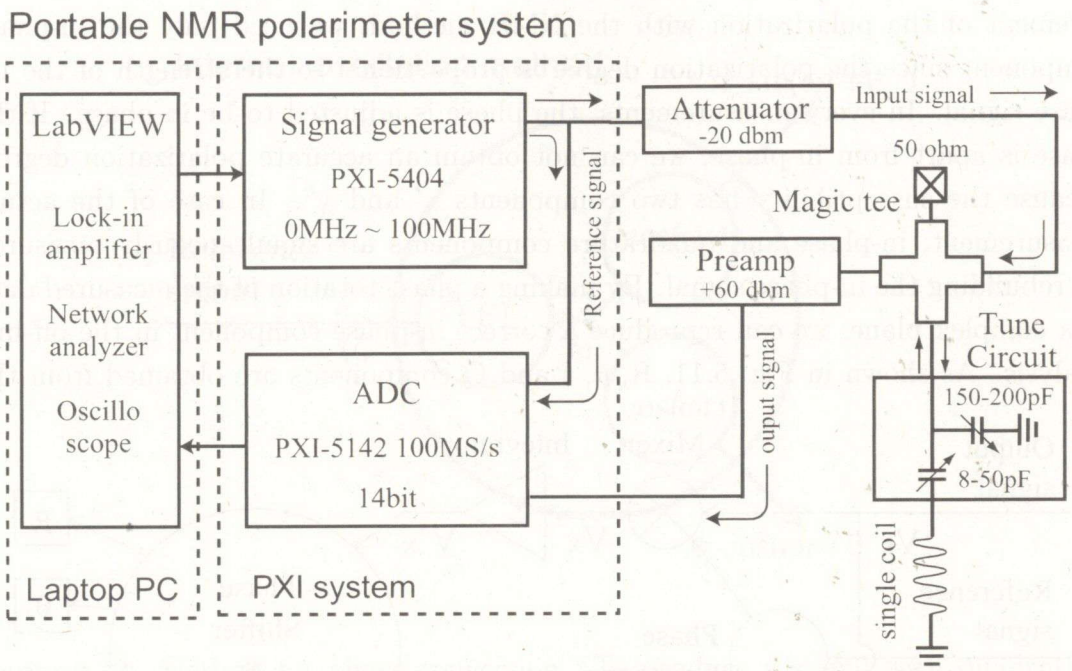

Figure 5.9: Schematic drawing of the portable NMR polarimeter system: The signal generation and data acquisition are realized by using PXI-5404 module (signal generator) and PXI-5142 (ADC) module with the software (LabVIEW).

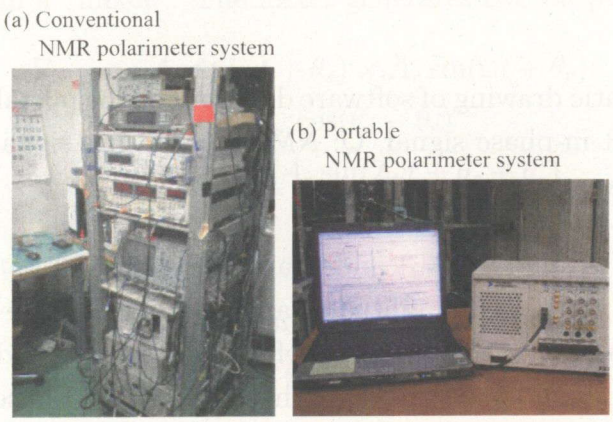

Figure 5.10: (a) The conventional NMR polarimeter system installed in a rack. Essentially, we need to prepare a signal generator, an oscilloscope, a lock-in amplifier, and a network analyzer. (b) The portable NMR polarimeter system consisting of a laptop PC and a PXI system.

— 5.5.3 Software developement in the portable system —

We developed a software LabVIEW program on the laptop PC to separate a specific NMR in-phase component from other frequencies and noises. In the mea-

surement of the polarization with the NMR method, we need only the in-phase component since the polarization degree is proportional to the strength of the in-phase signal. In every measurements, the phase is adjusted to be in-phase. If the phase is apart from in-phase, we can not obtain an accurate polarization degree, because the susceptibility has two components χ' and χ''. In case of the actual measurement, in-phase and quadrature components are simultaneously measured for rebuilding the in-phase signal. By making a phase rotation of the measured data in a complex plane, we can reproduce a correct in-phase component in the off-line analysis. As shown in Fig. 5.11, R, θ, I and Q components are obtained from the

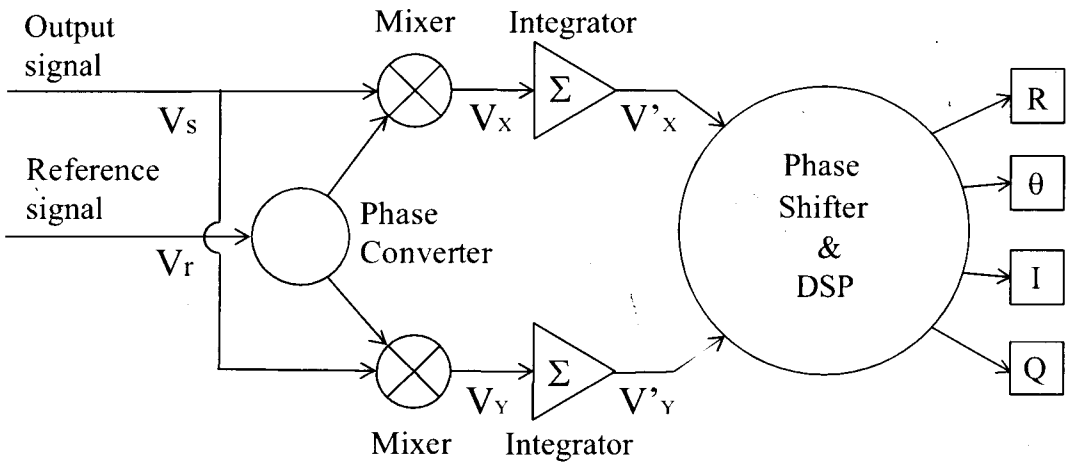

Figure 5.11: Schematic drawing of software diagram for the portable NMR polarimeter system. I: NMR in-phase signal, Q: NMR quadrature signal, R: Amplitude of signal, θ: signal phase.

output signal $V_s = A_s \sin(\omega t + \theta_s)$ and the reference signal $V_r = A_r \sin(\omega t + \theta_r)$. Here A_r and A_s are the signal amplitudes, and θ_r and θ_s are the signal phases.

To obtain the two signals, I and Q, the reference signal is divided into two signals with sine and cosine functions by using a phase converter. Phase conversion is performed with the software. For generating the cosine function from the sine function, we used "internal oscillation method" (see Fig. 5.12). In this method, the reference signal is firstly converted to a spectrum as a function of frequency by applying FFT (Fast Fourier Transformation) method. We determine the optimum frequency from the peak location in the FFT spectrum. By using the optimum frequency determined, two signals with waveform of $\sin(\omega t + \theta_r)$ and $\cos(\omega t + \theta_r)$ are generated. Digital data for these two waveforms are stored in a memory over the period of the Fourier transformation. This data are cashed in the memory, and are used as an in-phase signal for the next measurement.

In the software, the reference signal and output signal returned from the NMR

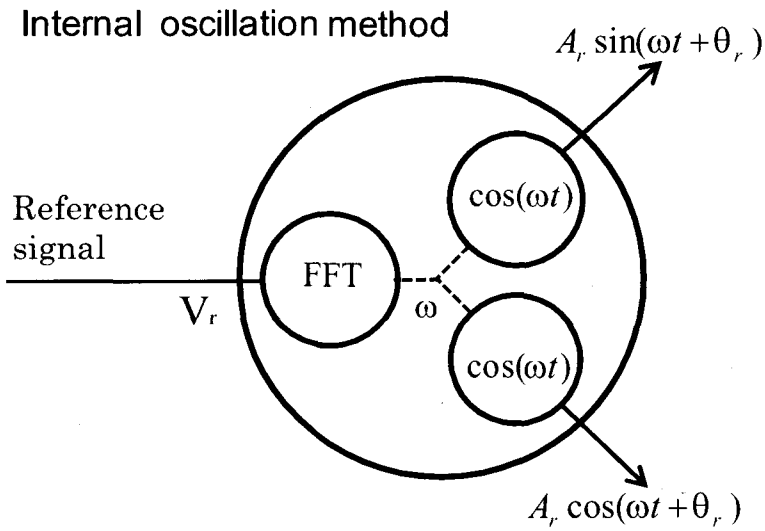

Figure 5.12: Method for phase conversion. To produce a signal with quadrature phase from the reference signal, sine and cosine functions with a frequency of the reference signal are generated. The frequency is determined from the optimum peak position in the FFT spectrum for the reference signal.

coil are multiplied in a "mixer". The mixer generates two outputs V_X and V_Y;

$$\begin{aligned} V_X &= A_s \sin(\omega t + \theta_s) \times A_r \sin(\omega t + \theta_r) && (5.5) \\ &= (1/2) A_s A_r \cos(\theta_s - \theta_r) \\ &\quad + (1/2) A_s A_r \sin(2\omega t + \theta_s + \theta_r) && (5.6) \end{aligned}$$

$$\begin{aligned} V_Y &= A_s \cos(\omega t + \theta_s) \times A_r \cos(\omega t + \theta_r) && (5.7) \\ &= (1/2) A_s A_r \sin(\theta_s - \theta_r) \\ &\quad + (1/2) A_s A_r \sin(2\omega t + \theta_s + \theta_r - \pi/2). && (5.8) \end{aligned}$$

Since the two inputs to the mixer have exactly the same frequency, the first terms of the mixer outputs in Eqs. (5.6) and (5.8) are constant. The second terms have a frequency $2\omega t$. Since the frequency of the term is doubled, they can be removed using "Integrator". Thus, the filtered outputs, V'_X and V'_Y become

$$V'_X \approx (1/2) A_s A_r \cos(\theta_s - \theta_r) \quad (5.9)$$

$$V'_Y \approx (1/2) A_s A_r \sin(\theta_s - \theta_r). \quad (5.10)$$

The noise included in the output signal is removed by the integrator as well. The in-phase component I, the quadrature component Q, the signal amplitude R, and the phase θ are derived from V'_X and V'_Y by using "Digital Signal Processor" (DSP). The phase θ is adjusted by adding a free parameter θ_{adj} to synchronize with the

in-phase signal by using "Phase Shifter". All simple formula used by the DSP in the software can be given as,

$$R = (2/A_r) \times \sqrt{V_X'^2 + V_Y'^2} = A_s \quad (5.11)$$

$$\theta = \theta_s - \theta_r + \theta_{adj} = \tan^{-1}(V_Y'^2/V_X'^2) + \theta_{adj} \quad (5.12)$$

$$I = R\sin(\theta) \quad (5.13)$$

$$Q = R\cos(\theta). \quad (5.14)$$

It is noted that in these processes mentioned above, we can separate the in-phase component I from the quadrature component Q of the NMR signal. After repeating many measurements by sweeping the magnetic field, we produce the NMR spectrum.

Section 5.6
Evaluation of the portable NMR polarimeter

— 5.6.1 Experimental procedure —

Since the NMR measurement is carried out without reducing the polarization for the HD target, a very weak input signal must be applied. Accordingly, an output signal becomes small, which makes the NMR signal observation difficult in noisy circuit background. In the NMR measurement, one million samples of digitized NMR signal heights are accumulated and averaged in each magnetic field setting. In this averaging process, statistical errors are decreased. It should be noted that the major part of noises come from thermal fluctuation. In order to obtain a high S/N ratio, it is important to accumulate a number of samples within a measurement period at a well controlled constant temperature. The HD gas with an amount of 1 mol was filled to the target cell and was solidified at 1.5 K in the SC. Two kinds of NMR signals were measured with the conventional and portable NMR polarimeter systems by exchanging only polarimeter part (shown in the dashed box of Fig. 5.9). The sweeping-speed of the magnetic field was 0.0137 Tesla/second and the RF frequency was kept at 29.45 MHz. The magnetic field was swept once and the data were recorded to a hard-disk.

— 5.6.2 Experimental results —

Fig. 5.13 shows NMR spectra obtained by using the conventional NMR system and the portable NMR system. Both H and F resonance signals are clearly observed at 0.688 and 0.729 Tesla, respectively. The resonance of F originates from the Teflon (PTFE:Poly-Tetra-Fluoro-Ethyle) coat of silver wire and the target cell and the support frame made of Kel-F, and that of H originates from the HD. The F resonance is stronger than the H resonance. This is explained by the difference of the numbers of H and F nuclei and the difference of effects of the magnetic field from the NMR coil. The NMR signals measured with the portable system are stronger than those measured with the conventional system. This difference would stem from the gain difference of the two systems depending on the RF frequency.

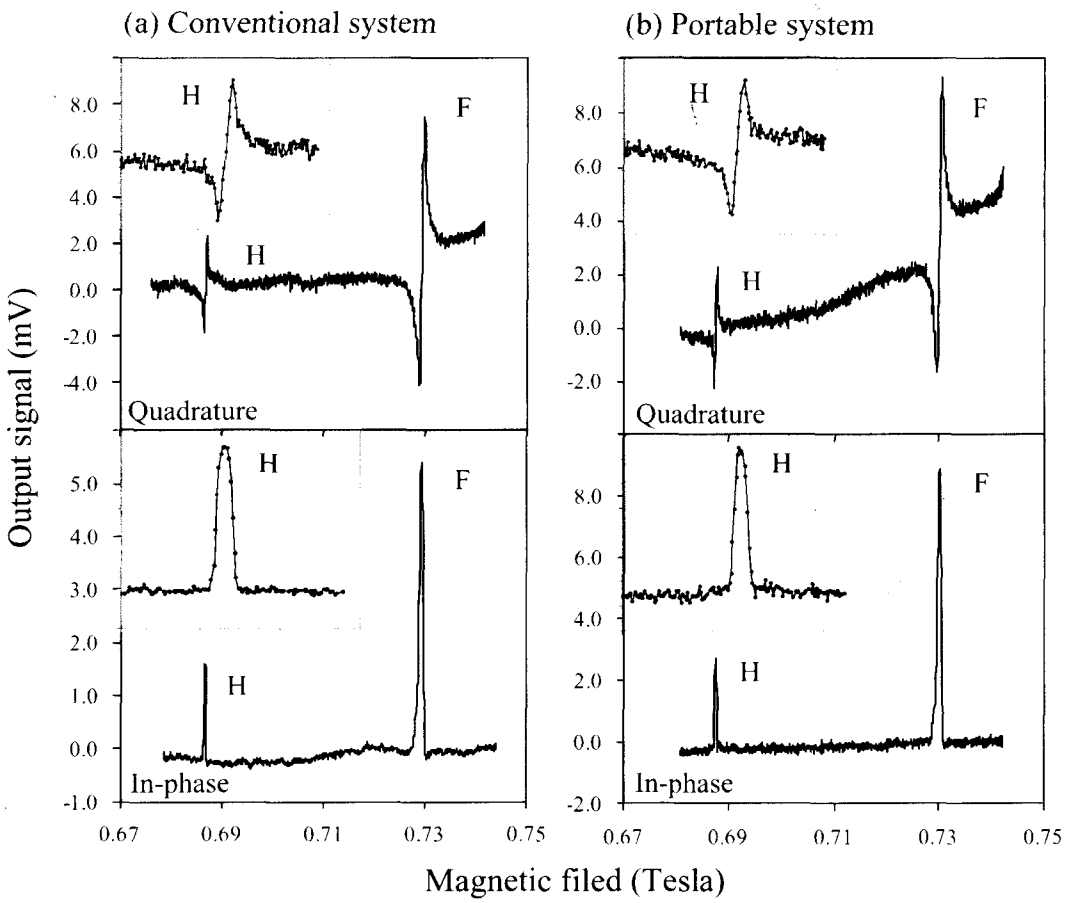

Figure 5.13: The NMR signals measured by the (a) conventional and (b) portable systems. The vertical axes are the magnitude of NMR output resonance. The horizontal axes are the magnetic field.

Table 5.4 shows the S/N ratios obtained for H and F in-phase peaks. The S is

the peak height and the N is the standard deviation of the baseline fluctuation near the peak. The S/N ratios measured with the portable system are about 50% lower than those with the conventional system. We checked the stability of the H peak

Table 5.4: S/N ratios of the H and F NMR signals measured by the conventional and portable NMR systems.

	H (proton)	F (Flourine)
Conventional system	74± 1	225± 1
Portable system	38± 1	111± 1

measured with the portable system periodically in a day. The fluctuation of the peak strength was found to be smaller than 5%. This stability satisfies the requirement that the hydrogen polarization degree must be determined within a precision of 10%.

Section 5.7

Summary of PXI-NMR

A portable NMR polarimeter system was developed for measuring the polarization degree of the polarized HD target at RCNP and SPring-8. Downsizing of the NMR system was successfully achieved by building the signal generator, oscilloscope, lock-in amplifier and network analyzer in the software (LabVIEW) with PXI. The performance of the portable NMR system was proved to be compatible with the conventional NMR system.

The S/N ratio of the portable NMR polarimeter system depends on the mathematical operation speed. If the number of samplings for averaging increases, statistical errors decrease. In the present development, we used a usual laptop PC (CPU:Core 2 Duo T7700, 2.4 GHz) for the portable NMR system. Thus, it is expected that the S/N ratio will be improved furthermore if we use PXI-express devices with higher speed of data transportation and a higher performance PC.

Improvement II

GC-QMS

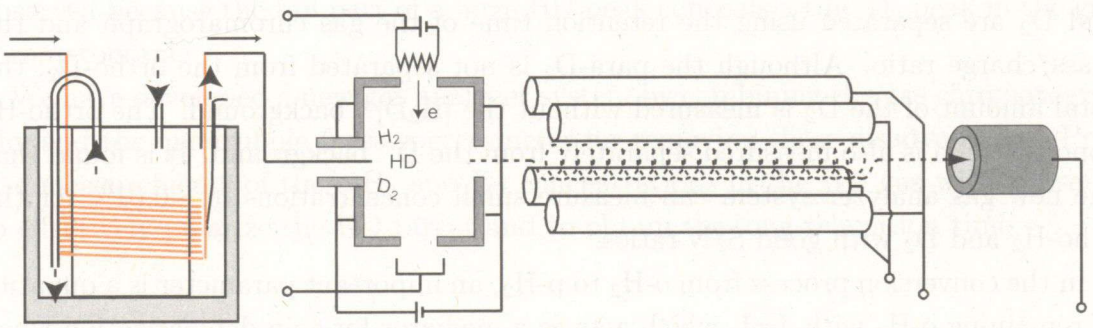

New gas analyzer system for HD

Chapter 6

Improvement II GC-QMS

A gas analyzer system has been developed to analyze Hydrogen-Deuteride (HD) gas for producing frozen-spin polarized HD targets, which are used for hadron photoproduction experiments at SPring-8. Small amounts of ortho-H_2 and para-D_2 gas mixtures ($\sim$0.01%) in a purified HD gas are a key to realize a frozen-spin polarized target. However, there was an intrinsic difficulty to measure these small mixtures in the HD gas with a quadrupole mass spectrometer (QMS) because D^+ and $[H_2D]^+$ produced from the ionization of HD molecules were misidentified as H_2 and D_2 molecules, respectively, and became backgrounds for the measurement of the H_2 and D_2 concentrations. In addition, the ortho-H_2 and para-D_2 are not distinguished from the para-H_2 and ortho-D_2, respectively, with the QMS. In order to obtain reliable concentrations of these gas mixtures in the HD gas, we produced a new gas analyzer system combining two independent measurements with a gas chromatograph and the QMS. Helium or neon gas was used as a carrier gas for the gas chromatograph which was cooled at $\sim$110 K. The para-H_2, ortho-H_2, HD, and D_2 are separated using the retention time of the gas chromatograph and the mass/charge ratio. Although the para-D_2 is not separated from the ortho-D_2, the total amount of the D_2 is measured without the $[H_2D]^+$ background. The ortho-H_2 concentration is also measured separately from the D^+ background. It is found that the new gas analyzer system can measure small concentrations of $\sim$0.01% for the otho-H_2 and D_2 with good S/N ratios.

In the conversion process from o-H_2 to p-H_2, an important parameter is a quantity of remaining o-H_2 with J=1, which acts as a mediator for spin depolarization when the temperature of the solid HD target rises up to more than 4 K: the lower the impurity of o-H_2, the longer the relaxation time of hydrogen polarization. Thus, it is essential to control the admixture of o-H_2 in the highly purified HD gas.

When the HD gas is kept in the gas container for a long time, the quality of the HD gas is deteriorated due to the dissociation process, $2HD \longleftrightarrow H_2 + D_2$ and the H_2 and D_2 gasses are naturally yielded. For the HD purification, we installed a distillation still to make the pure HD gas with a purification level of 99.99%. The next indispensable problem to be solved is how to measure the small admixtures of o-H_2, p-H_2, and D_2 in the HD gas. The conventional method is to use a quadrupole mass spectrometer (QMS) for gas analysis. This instrument makes use of a principle that the analyzed gas is ionized at an ion source by electron bombardment and ions are mass-separated according to the mass/charge ratio (u/e). When a HD gas is entered in the ion source of the QMS, small amounts of H^+ and D^+ are produced

from HD molecules. Other ions of H_3^+, $[H_2D]^+$, $[HD_2]^+$, and D_3^+ are also produced by recombination. This means that D^+ and $[H_2D]^+$ are misidentified as H_2^+ and D_2^+, respectively. The QMS cannot distinguish the molecules and fragments with a same mass/charge ratio. We call this problem as "fragmentation problem". The fragments produced by ionization are listed in Table 6.1.

Table 6.1: The isomers in the HD gas and expected fragments.

u/e	1	2	3	4	5	6
Molecules		H_2^+	$[HD]^+$	D_2^+		
Fragments	H^+	D^+	H_3^+	$[H_2D]^+$	$[HD_2]^+$	D_3^+

To overcome the fragmentation problem, we designed a system combined with a gas chromatograph and the QMS for the HD gas analysis with a high dynamic range of more than 10^4. The gas chromatograph separates the isomers in the HD gas in terms of time. The QMS separates the isomers in terms of mass/charge. By combining two different analysis systems, it is possible for us to analyze the H_2 and D_2 concentrations in the HD gas, precisely. The James Madison University group has successfully employed a gas chromatography for distinguishing o-H_2 and p-H_2 [68]. However, a small D_2 admixture with a level of 0.01% cannot be clearly observed because the tail part of a huge HD peak conceals a tiny D_2 peak in the gas chromatogram.

We have developed a new gas analyzer system by combining the gas chromatography and the quadrupole mass spectrometer for removing these disadvantages. Precise measurements of the o-H_2 and D_2 concentrations in the HD gas will be useful to effectively polarize the HD target and to obtain the long relaxation time.

Section 6.1
System overview

Fig. 6.1 shows a schematic diagram of a new gas analyzer system. The HD gas with a volume of 500 μl is infused into a column by a gas sampler. The sample gases are pushed in the column together with a carrier gas. The isomers of o-H_2, p-H_2, HD, and D_2 in the HD gas are separated by using the difference of adsorbent action to zeolites which are affixed on the inner wall surface of the column. The separated isomers in the HD gas are analyzed by the quadrupole mass spectrometer as a function of the mass/charge ratio. In the usual method of gas chromatography, the temperature of a thin zeolite column is increased during the analysis because the retention time of the gas is very long. On the other hand, since the hydrogen

and deuterium are light and small particles, the retention times of o-H_2, p-H_2, HD and D_2 are as short as a few second at the room temperature. Because of this, the zeolite column is cooled down to about 110 K to attain a reasonably long retention time for the hydrogen and deuterium gases. Actually, the column is cooled down in a constant temperature dewar by controlling the vapor flow from liquid N_2 (LN_2). The column is installed in the dewar with the vacuum insulation layer. LN_2 is stored at the center layer, and the cold vapor gas from LN_2 flows from the inner layer to the outer layer. We use the He or Ne gas as a carrier gas. The flow rate of the gas is controlled by using a flow controller. The sample which is out of the column is detected by the QMS. This QMS is a product of MKS Instruments [69] and is specially tuned-up to increase the sensitivity for detecting light molecules such as H_2, HD, D_2, and T_2.

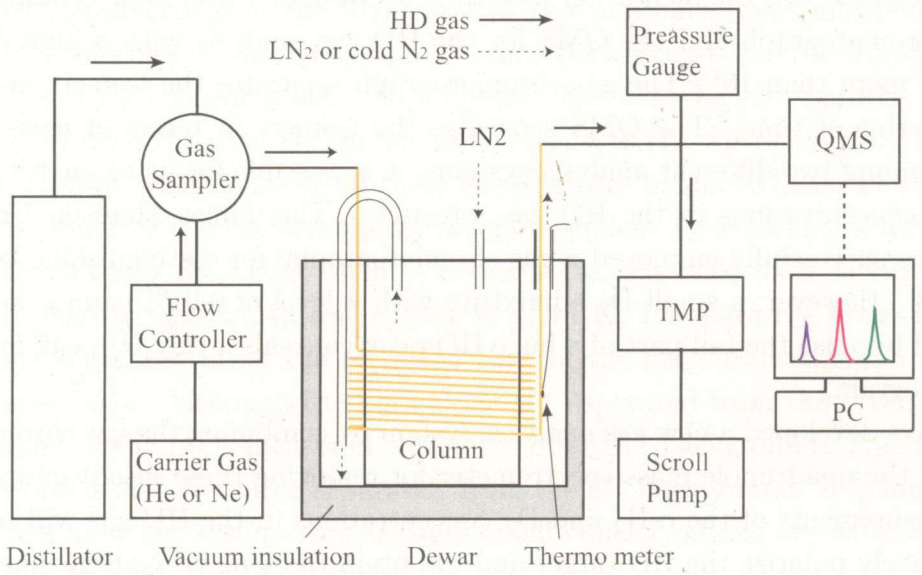

Figure 6.1: Schematic diagram of the gas chromatograph and the quadrupole mass spectrometer for the HD gas analysis. The HD gas is injected with a carrier gas from the entrance of the column via gas sampler. QMS: quadrupole mass spectrometer. TMP: Turbo molecular pump.

— 6.1.1 Distillator —

To make a polarized HD target with a long relaxation time of more than one month, we need to prepare a highly purified HD gas. However, if we use highly purified HD gas, the aging time for polarizing the HD becomes long. This is an experimental dilemma. One of methods to overcome this dilemma is to dope an appropriate amount of o-H_2 and p-D_2 impurities in the purified HD gas. The appro-

priate amount is approximately an order of 0.01%. The purity of the commercially available HD gas is about 96%. Contaminations are mostly H_2 ($\sim$ 2%) and D_2 ($\sim$2%).

The HD gas is necessary to be purified up to $\geq$ 99.99% for optimizing the amount of impurities. The gas distillation system used to purify the HD gas at RCNP is shown in Fig. 6.2. The commercial gas is fed to the pot inside the ditillator. There are stainless cells called "Helipack" inside the pot. Temperature gradient is realized by cooling the top of the pot and heating the bottom by the thermal radiation. Heat exchange between gas and liquid takes place on the cells. A gas with a low boiling temperature is extracted from the top of the distillator. By using the difference of the boiling temperatures of HD (16.6 K), H_2 (14.0 K) and D_2 (18.7 K), we separate the HD gas from the others. In the initial trial, the concentrations of HD, H_2, and D_2 were measured with the QMS. Although the H_2 and D_2 concentrations were decreased less than 0.1%, it was not possible to measure the concentrations precisely because of the fragmentation problem.

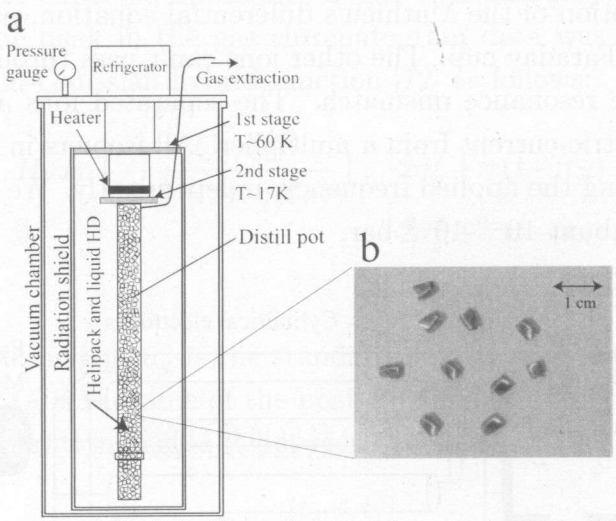

Figure 6.2: (a) The design view of the distillator. The H_2 gas is extracted from the top of the distilllation pot. (b) The photograph of stainless steel packs which are filled into the pot in the distillator. Each pack has a rolled shape like a coil and twisted for efficient heat conduction between gas and liquid.

We operated the distillator for one week to obtain pure HD gas. The commercial HD gas with an amount of 5.3 mol was fed to the pot. The HD gas was extracted from the distillator with a flow rate of 2.0 ml/min to the gas storage tanks made of stainless steel. The H_2 concentration was very high in the beginning and the HD purity gradually increased in a few days. After extracting about 1 mol gas, the gas analysis started.

— 6.1.2 Quadrupole mass spectrometer(QMS) —

The quadrupole mass spectrometer (QMS) consists of an ion source, an extraction plate, four cylindrical electrodes, and a Faraday cup. A high mass resolution and compactness are its good features. The present QMS (made by MKS Instruments, Microvision Plus [69]) is equipped with a multiplier to measure a partial pressure down to 10^{-17} bar. The QMS has an ability to well distinguish the masses of He (amu=4.0026) and D_2 (amu=4.0282), because its performance is customized to measure low mass molecules such as H_2, D_2, and T_2 in the mass range of 1~6 [70].

Constant and alternative voltages are applied to four cylindrical electrodes (quadrupole rods) as shown in Fig. 6.3. The sample gas is ionized in an ionization chamber by an electron impact method and then accelerated by the extraction plate along to the symmetry axis of the quadrupole rods. Ionized ions move towards the Faraday cup with a spiral motion coupled to a displacement motion. Ionized ions, which satisfy the resonance condition of the Mathieu's differential equation, pass the quadrupole rods and reach the Faraday cup. The other ions can't pass through the quadrupole rods because of the resonance mismatch. The separated ions are detected at the Faraday cup as electric current from a multiplier. All isomers in the HD gas can be measured by scanning the applied frequency, independently. We operated the QMS with a pressure of about 10^{-9}-10^{-8} bar.

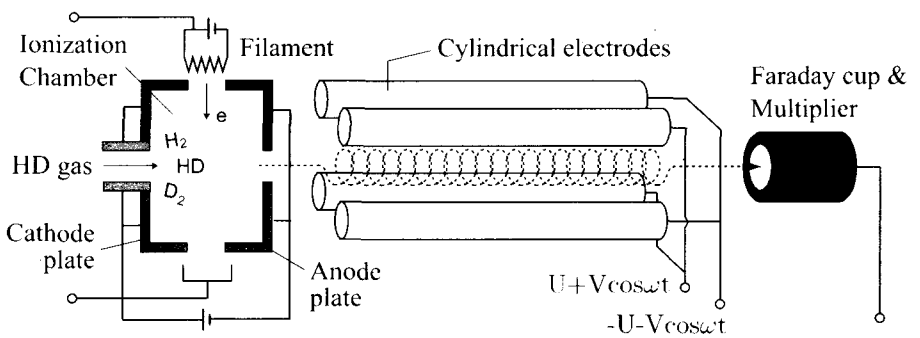

Figure 6.3: Structure of the quadrupole mass spectrometer. Constant (U) and alternative (V·cos(ωt)) voltages are applied to four cylindrical electrodes. The input HD gas is ionized in the ionization chamber by electron bombardment. Ions are injected along the central symmetry axis of the four cylindrical electrode-rods. An ion satisfying a resonance condition with a frequency ω makes a helical movement coupled to a displacement movement towards the Faraday cup, and is finally detected with a multiplier.

— 6.1.3 Gas chromatography (GC) —

We use the Molsieve 5Å PLOT (porous layer open tubular) type column. The capillary column is made of fused silica and coated by polyimide. The size of the capillary column is summarized in Table 2.

Table 6.2: Specification of the fused silica column. Molsieve 5Å PLOT type column [71] was used. OD and ID stand for the outer and inner diameters of the column.

OD	ID	Length	Zeolite thickness
0.70 mm	0.50 mm	50 m	0.050 mm

Fig. 6.4 shows an expected spectrum of gas chromatography as a function of retention time. The peak in the gas chromatogram data was analyzed by fitting with the exponential-Gaussian hybrid function [72] as follows:

$$f(t) = \begin{cases} Hexp\left(\dfrac{-(t-t_R)^2}{2\sigma_g^2 + \tau(t-t_R)}\right), & 2\sigma_g^2 + \tau(t-t_R) > 0 \\ 0, & 2\sigma_g^2 + \tau(t-t_R) \leq 0, \end{cases} \tag{6.1}$$

where H is the peak height, σ_g is the standard deviation of the Gaussian, τ is the time constant, and t_R is the time of the peak maximum.

We define the separation degree R between two peaks as,

$$R = \frac{(t_2 - t_1)}{(\sigma_1 + \sigma_2)}, \tag{6.2}$$

where t_1 and t_2 are their retention time, σ_1 and σ_2 are calculated as,

$$\sigma_1 = \sqrt{\sigma_{g1}^2 + \tau_1^2}, \ \sigma_2 = \sqrt{\sigma_{g2}^2 + \tau_2^2}, \tag{6.3}$$

where σ_{g1} and σ_{g2} are the standard deviation for the peak 1 and the peak 2, respectively, and τ_1 and τ_2 are the time constant for the peak 1 and peak 2, respectively.

Longer column length and longer retention time are considered to give large separation R. But very long retention time is not appropriate for the present work. To measure the HD gas from the distillator efficiently, we have estimated the best R by changing various parameters such as the temperature of the column and the flow rate of the He carrier gas.

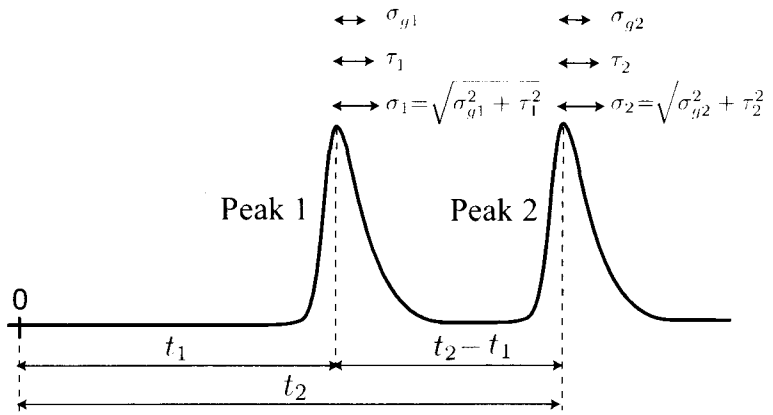

Figure 6.4: Expected peaks in the gas chromatography. t_1 and t_2 are the retention times. τ_1 and τ_2 are the time constant of the peak. The separation degree R is defined by Equation 6.2. Two peaks are separated completely with R > 1.5.

Section 6.2
Experimental results and analysis

— 6.2.1 Effect of temperature and gas flow —

For precise measurement of the concentration of isomers in the HD gas, R is required to be more than 1.5. To determine the optimum temperature and the flow rate, the separation degree R between HD and D_2 was measured by changing various parameters of the temperature and the flow rate as shown in Table 6.3. Lower temperature (105K) with a flow rate of 10ml results in the best separation. We used a helium carrier gas for the gas chromatograph in this study.

Table 6.3: The separation degree R between HD and D_2. Errors are the sum of the statistical.

Flow rate	1 ml	3 ml	5 ml	10 ml	20 ml	30 ml
105 K	–	–	5.754±0.009	7.988±0.042	4.568±0.007	5.346±0.008
110 K	–	4.881±0.005	5.346±0.032	7.646±0.017	6.107±0.013	6.685±0.026
120 K	2.610±0.002	4.383±0.018	7.425±0.054	7.702±0.061	6.800±0.043	6.862±0.055
130 K	2.369±0.002	2.416±0.004	3.946±0.087	5.253±0.027	3.748±0.062	3.802±0.016

— 6.2.2 Measurement of combination with GC and QMS —

We prepared a sample gas by mixing appropriate amounts of H_2, HD, and D_2 gases. The sample was analyzed by the gas analyzer system. The neon gas with a flow rate of 35 ml/min was used to carry the sample through the column cooled at 105 K. The p-H_2 and o-H_2 were detected at 8 and 9 minutes, respectively, after the injection of the sample as shown in Fig. 6.5(a). The HD and D_2 gases were detected at 11 and 14 min, respectively, as shown in Fig. 6.5(b) and (c). Using both the GC and the QMS, we could observe the p-H_2, o-H_2, HD, and D_2 gases separately by measuring the retention time in the GC and by determining the mass/charge ratios in the QMS as shown in Fig. 6.6. When the purity of the sample HD gas becomes very high (~99.9%), backgrounds disturb clear observation of the H_2 and D_2 peaks. This problem is discussed in Sec. 6.2.4.

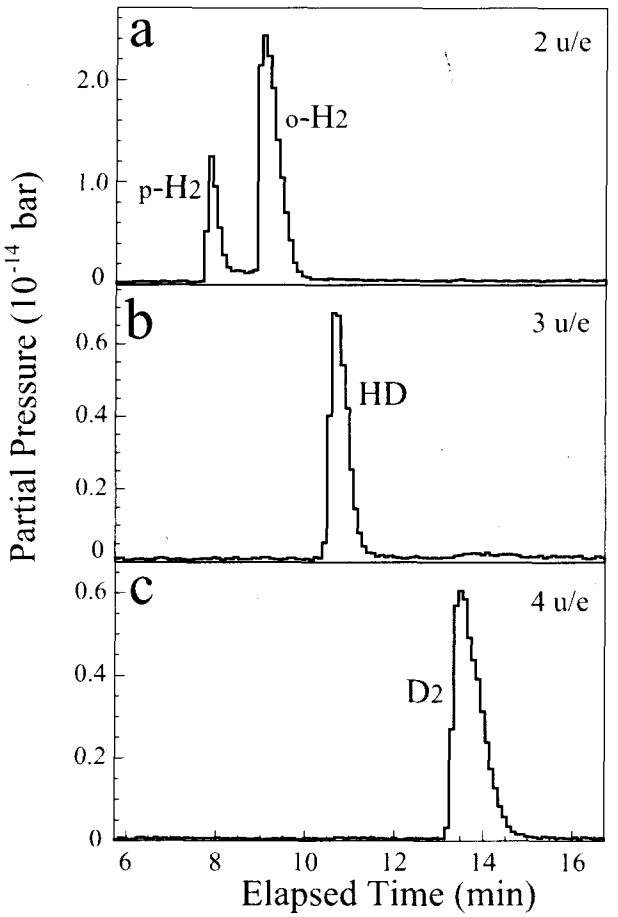

Figure 6.5: Gas chromatograms for the gases with the mass/charge ratios of (a) 2 (b) 3 and (c) 4. The vertical axis is the partial pressure for each gas and the horizontal axis is the elapsed time after the injection of the gas sample.

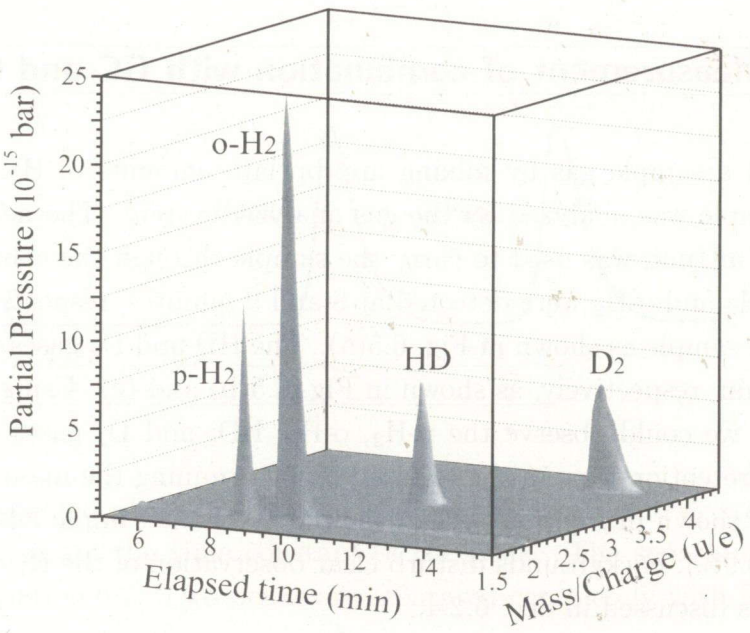

Figure 6.6: Three-dimensional plot of the elapsed time of the GC vs the mass/charge ratio measured by the QMS. The z axis is the partial pressure of each gas.

— 6.2.3 Transition between p-H_2 and o-H_2 —

There are mysterious events between the p-H_2 and o-H_2 peaks in the gas chromatograms as shown in Fig. 6.5(a). These events are considered to be produced by the transition from p-H_2 to o-H_2 or o-H_2 to p-H_2 in the column at low temperature. If the p-H_2 or o-H_2 molecule interacts with magnetized materials, the transition can be induced although the materials have not been clearly specified yet. Such events between the p-H_2 and o-H_2 peaks are observed in another experiment [68].

We fit the gas chromatogram data as shown in Fig. 6.7 with the function consisting of two exponential-Gaussian hybrid functions written in Eq. 6.1, a function (Eq. 6.4) for reproducing the transition events written below, and a constant for background events.

$$f_{o\Leftrightarrow p}(t) = \begin{cases} CH_1 exp\left(\dfrac{-(t-t_1)^2}{2\sigma_{g1}^2 + \tau_1(t-t_1)}\right), \\ 2\sigma_{g1}^2 + \tau_1(t-t_1) > 0 & t \leq t_1 \\ C\left(\dfrac{(H_1 - H_2)}{(t_1 - t_2)} \times (t-t_1) + H_1\right), & t_1 < t < t_2 \\ CH_2 exp\left(\dfrac{-(t-t_2)^2}{2\sigma_{g2}^2 + \tau_2(t-t_2)}\right), \\ 2\sigma_{g2}^2 + \tau_2(t-t_2) > 0 & t_2 \leq t, \end{cases} \tag{6.4}$$

where C is a normalization factor. H_1 and H_2 are the p-H_2 and o-H_2 peak heights, σ_{g1} and σ_{g2} are the standard deviation of the Gaussian, τ_1 and τ_2 are the time constants, and t_1 and t_2 are the time of the peak maximum, respectively.

The errors for the output of the QMS are estimated from the measurement fluctuation at a stable pressure. The reduced χ^2 for the fit is 37. The tail of the o-H_2 peak is not well reproduced, which makes the reduced χ^2 large. The concentrations of p-H_2, o-H_2, and transition events are obtained as shown in Table 6.4. The errors of the parameters in the fit and the deviation between the fit and the data at the o-H_2 peak tail are considered as errors of the concentrations.

Table 6.4: Concentrations of p-H_2, o-H_2, and transition events obtained by the fit to the data.

	para-H_2	para-H_2 $\Leftrightarrow$ ortho-H_2	ortho-H_2
Concentration	20±1%	7±1%	73±2%

— 6.2.4 Analysis for pure HD —

The best separation of the peaks was obtained when the helium carrier gas with a flow rate of 10 ml/min was used at 105 K as listed in Table 6.3. When the purity of a sample HD gas becomes very high, the experimental condition needs to be optimized in order to reduce backgrounds. A pure sample HD gas was analyzed by using a helium carrier gas with a flow rate of 1.0 ml/min at 125 K. As shown in Fig. 6.8(a), the HD peak is dominantly observed at 16.5 min in 3 u/e. Another peak is also observed at the same position in 2 u/e. This peak is due to D^+ produced from the ionization of HD. Without the GC, the D^+ component could not be easily separated from

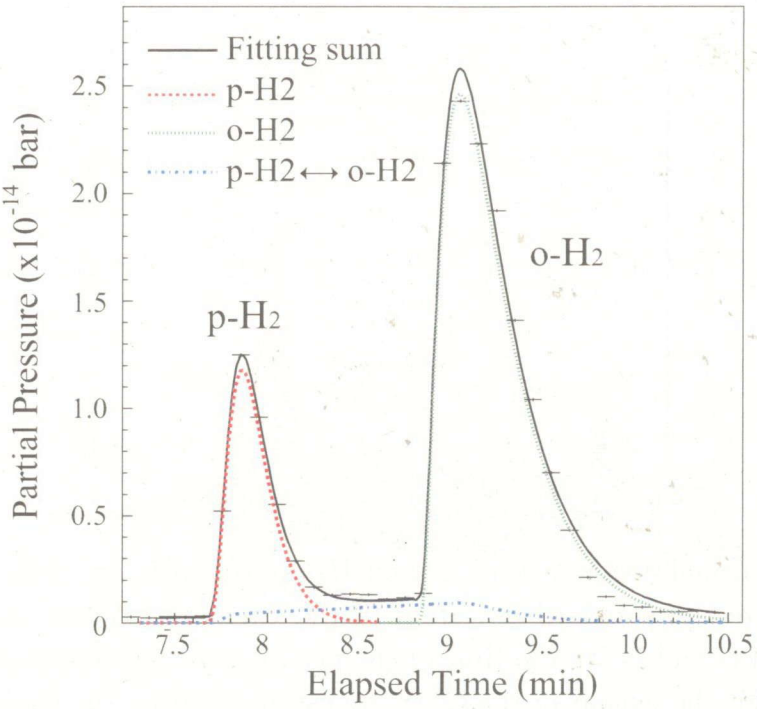

Figure 6.7: The fitting to the data with 2 u/e. Peaks of o-H_2 and p-H_2 are fitted by using Eqn. 6.1. The continuum in the transition region is fitted by using Eqn. 6.4 as shown by the dash-dotted curve.

real H_2 signals and the measurement of the H_2 concentration was uncertain. The o-H_2 peak is observed at 15.5 min separately from the p-H_2 peak at 14.1 min. The concentrations of p-H_2 and o-H_2 were obtained as 0.005±0.001(stat.)±0.001(syst.)% and 0.010±0.001(stat.)±0.002(syst.)%, respectively as listed in Table 6.5. The H_2 events between the p-H_2 and o-H_2 peaks and the tail of the peaks were assumed to be the p-H_2 or o-H_2 with a ratio of 5 (p-H_2) to 10 (o-H_2). Present background level in 2 u/e gas chromatogram enables us to measure the o-H_2 concentration with a precision better than 0.01%.

The linearity of the output of the QMS and the detection efficiency of the GC were taken into account as the systematic errors. We checked the linearity in the partial pressure region of 10^{-16}-10^{-12} bar. The relation between the amount of sample gas and the partial pressure measured by the spectrometer were well fitted with a linear function. The deviation from the linear function was smaller than 12% of the measured partial pressure. The detection efficiency was measured by storing the sample gas and the carrier gas in a tank after passing through the gas chromatography and the QMS. The uncertainty of the detection efficiency was found to be about 17%.

A pure sample HD gas was analyzed by using a neon carrier gas with a flow rate of 1.0 ml/min at 125 K. As shown in Fig. 6.8(b), the HD peak is dominantly observed at

16.0 min in the gas chromatogram with 3 u/e. At the same location of the HD peak, another peak is observed in 4 u/e. This peak is inferred to appear due to the $[H_2D]^+$ molecule produced by the ionization of HD, which was confirmed by the result that the $[HD_2]^+$ was also observed at the same location in the gas chromatogram with 5 u/e (not shown). The D_2 peak is clearly observed at 19.8 min on top of the long tail of the $[H_2D]^+$ peak. The concentration of D_2 in the sample HD gas was obtained as

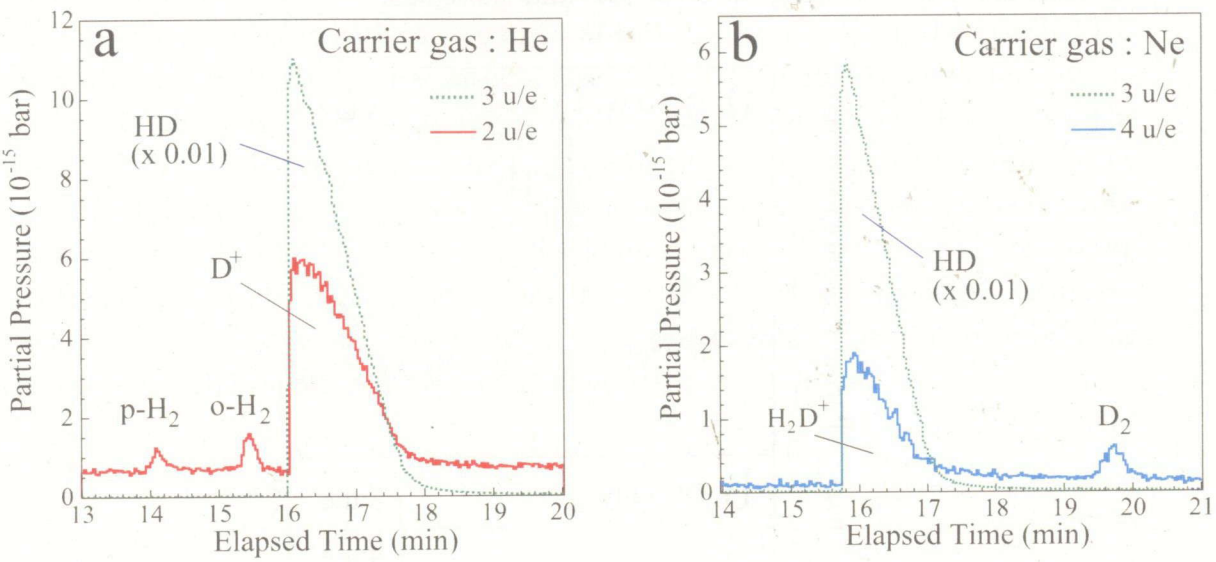

Figure 6.8: (a) Gas chromatograms for a distilled HD gas measured by using the helium carrier gas. The gas chromatograms with 2 u/e (solid curve) and 3 u/e (dotted curve) are plotted. (b) Gas chromatogram for the distilled HD gas measured by using the neon carrier gas. The gas chromatograms with 3 u/e (dotted curve) and 4 u/e (solid curve) are plotted. The vertical axis is the partial pressure of each gas. The horizontal axis is the elapsed time.

0.043 ± 0.001(stat.)± 0.009(syst.)%. Judging from the fluctuation of the background around the D_2 peak, the D_2 concentration of 0.01% can be detected by using the present new gas analyzer system.

Table 6.5: The measured concentrations of p-H_2, o-H_2, HD, and D_2 in the distilled HD gas

Isomers	Concentration			
p-H_2	0.005	± 0.001(stat.)	± 0.001(syst.)	%
o-H_2	0.010	± 0.001(stat.)	± 0.002(syst.)	%
HD	99.942	± 0.002(stat.)	± 0.009(syst.)	%
D_2	0.043	± 0.001(stat.)	± 0.009(syst.)	%

In Fig. 6.9, a D_2 peak in gas chromatogram with 4 u/e, measured by using the gas chromatography and QMS, is compared with another small D_2 peak in the gas chromatogram, measured by using the gas chromatography only. The D_2 peak is clearly observed with a good S/N ratio in Fig. 6.9(a). However, it is very difficult to find the small D_2 peak because of large backgrounds from the tail of the HD peak in Fig. 6.9(b). The S/N ratio for the D_2 peak was improved by a factor of 10 in the measurements by using both the GC and the QMS.

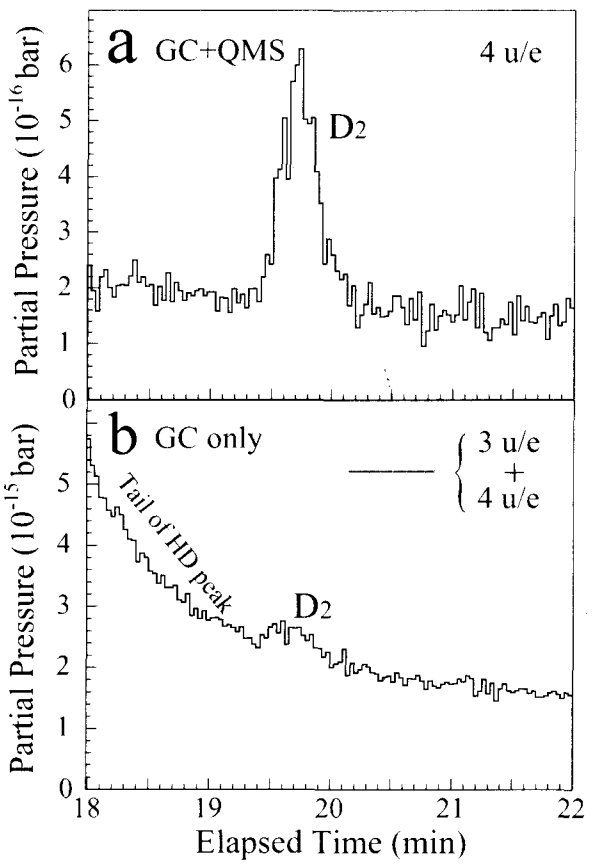

Figure 6.9: (a) The gas chromatogram with 4 u/e for a distilled HD gas measured by using the neon carrier gas. (b) The sum of the gas chromatograms with 3 u/e and 4 u/e for a distilled HD gas measured by using the neon carrier gas. The vertical axis is the partial pressure of each gas. The horizontal axis is the elapsed time.

Section 6.3

Summary of GC-QMS

We have developed a new HD gas analyzer system by combining the gas chromatograph and the quadrupole mass spectrometer for producing the polarized HD target to be used for the hadron photoproduction experiments at SPring-8. The new system enabled us to observe p-H_2, o-H_2, HD, and D_2 separately. We succeeded in measuring small concentrations ($\sim$0.01%) of p-H_2, o-H_2, and D_2 in the distilled HD gas with good S/N ratios. Recently, another effort to measure the small concentrations of the p-H_2, o-H_2, and D_2 in the HD gas is devoted at JLab [73]. The Rome group is trying to analyze the HD gas for the JLab polarized HD project, by using the Raman scattering of laser light. The accuracy of measuring the concentrations will be improved by introducing the Raman spectroscopy although the setup is awfully complicated. It should be noted that the developments of gas analyzing techniques reported in the present work will play an important role in producing the polarized HD target under a well defined HD gas condition.

Improvement III

HD-Distill

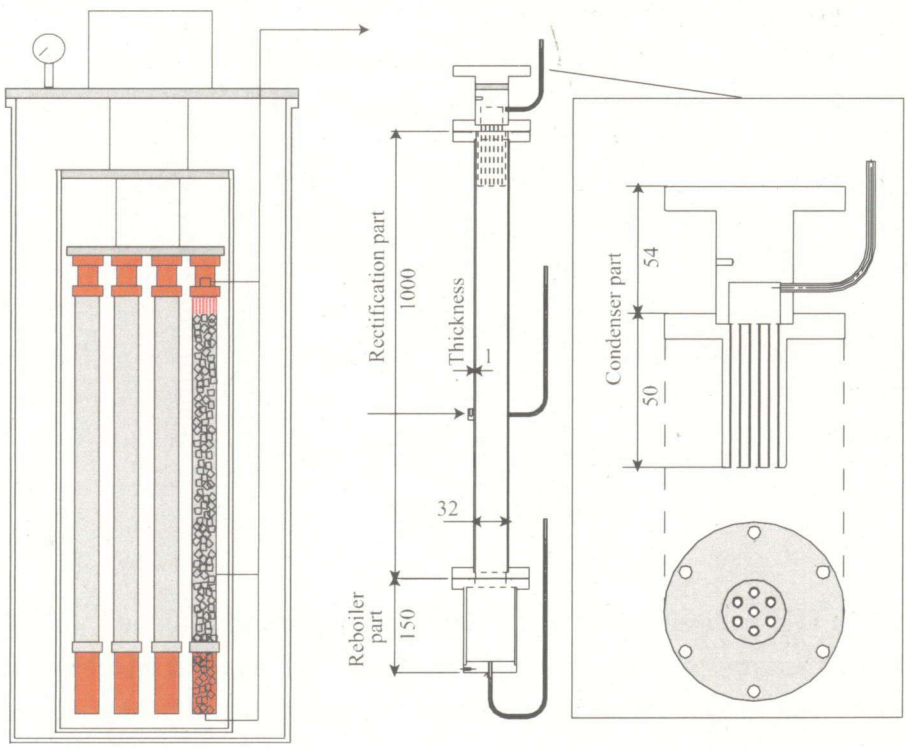

New distillation system for HD

Chapter 7

Improvement III HD-Distill

We have developed a new cryogenic distillation system to purify Hydrogen-Deuteride (HD) gas for polarized HD targets in LEPS experiments at SPring-8. A small amount of ortho-H_2 ($\sim$0.01%) in the HD gas plays an important role in efficiently polarizing the HD target. Since there are 1$\sim$5% impurities of H_2 and D_2 in commercially available HD gases, it is necessary to purify the HD gas up to $\sim$99.99%. The distillation system is equipped with a cryogenic distillation unit filled with many small stainless steel cells called "Heli-pack". The distillation unit consists of a condenser part, a rectification part, and a reboiler part. The unit is kept at the temperature of 17$\sim$21 K. The Heli-pack has a large surface area that makes a good contact between gases and liquids. An amount of 5.2 mol of commercial HD gas is fed into the distillation unit. Three trials were carried out to purify the HD gas by changing temperatures (17.5 K and 20.5 K) and gas extraction speeds (1.3 ml/min and 5.2 ml/min). The extracted gas was analyzed using a gas analyzer system combining a quadrupole mass spectrometer with a gas chromatograph. One mol of HD gas with a purity better than 99.99% has been successfully obtained for the first time. The effective NTP (Number of Theoretical Plates), which is an indication of the distillation performances, is obtained to be 37.2$\pm$0.6. This value is in good agreement with a designed value of 37.9. The HD target is expected to be efficiently polarized under a well-controlled condition by adding an optimal amount of ortho-H_2 to the purified HD gas.

One of the common problems is related to the measurement of the HD gas concentration purified by distillation. In the past, the purity of the HD gas was measured by using a quadrupole mass spectrometer (QMS). The HD gas is ionized in the QMS by electron bombardment, which produces not only HD^+ but also D^+. The D^+ is mis-identified as the H_2^+ impurity because the mass and charge are the same. Therefore, the amounts of impurities were not precisely determined, and the distillation performance was not checked correctly. However, the afore-mentioned problem was solved by introducing a new gas analyzer system combining a gas chromatograph with the QMS [74]. This new gas analyzer enables us to measure the concentrations of the impurities with a precision better than 0.01%.

Since the commercial HD gas has about 1$\sim$5% impurities of H_2 and D_2, we need to purify it up to $\sim$99.99% by distillation. After the distillation, an optimal amount of the o-H_2 is added to efficiently polarize the HD target. In the past, we used a cryogenic distillation system, which had a rectification column containing about 20 cells called Stedman packing [44, 70], provided by the ORSAY group in 2006.

This distillation system required us to prepare the subsequent second distillation in order to obtain a high purity HD gas for the polarized HD target. The HD gas was distilled, and the H_2 component was removed in the first distillation. Next the HD gas was again distilled, and the D_2 component was removed in the second distillation. The periods of the first and second distillations were 20 days and 10 days, respectively. Another group used a distillation system consisting of many stainless coiled ribbons, called Dixon Ring, for separating hydrogen isotopes [75]. The Dixon Ring has a large surface area, giving a good separation of the hydrogen isotopes.

We have developed a new cryogenic distillation system containing many small stainless steel cells called "Heli-pack" [76]. The Heli-pack, which has a surface area larger than the Dixon Ring, is expected to give a better separation of the hydrogen isotopes. In this chapter, we report the performance of the newly developed cryogenic distillation system for producing the pure HD gas.

Section 7.1
Experiment

— 7.1.1 Principle —

In general, the distillation system is used to separate a desired chemical component from the mixed compound by utilizing the vaporability difference. A low-boiling component vaporizes, and is separated from others as a gas. Then high-boiling components are liquefied. In chemical industries, this kind of the distillation method is used to acquire a high purity chemical component for large-volume production.

In the case of the HD distillation, H_2, HD, and D_2 gases are liquefied by a refrigerator at a low temperature. Using differences between the boiling points among H_2, HD, and D_2, HD gas is separated from the others. At the beginning of the distillation process, the low-boiling component, H_2, is kept as a gas at the upper part of the distillation unit. The other (HD and D_2) components drop down to the bottom of the distillation unit as liquids. Packs, which promote the separation of the components, are filled in the distillation unit and make a good contact between gases and liquids. The bottom of the distillation unit is warmed up by radiation heating. Since the middle part of the distillation unit is made of stainless steel with small heat conduction, a temperature gradient is realized. The H_2 gas is extracted from the top through a pipe connected to a gas storage tank. Then, the remaining HD component vaporizes with a high purity after extracting the H_2 component. The

HD is extracted to another tank, and is used for the polarized HD target.

As seen in Fig. 7.1(a) [77], the H_2 component is easily evaporated in comparison with the HD component at 17 K. The vaporability of a low-boiling component to a high-boiling component is expressed by using the vapor pressure ratio of the two components, and is defined in terms of the relative volatility α as a function of temperature. Fig. 7.1(b) shows a relative volatility α for $P(H_2)/P(HD)$ and $P(HD)/P(D_2)$. The relative volatility increases with decreasing the temperature. The distillation efficiency increases with increasing relative volatility. However, the distillation efficiency decreases when HD is solidified. Therefore, the distillation efficiency is expected to be optimum at around 17 K.

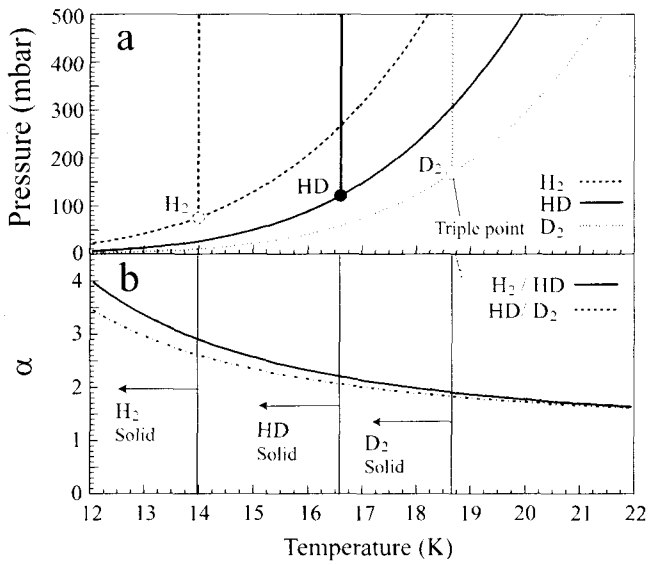

Figure 7.1: (a) Phase diagram of H_2, HD, and D_2. Triple points for three components are indicated by the circles. The lines in the right side of the triple points show the border of the transition between liquid and gas (vapor pressure curve). The vertical lines show the border of the transition between solid and liquid (melting curve). The lines in the left side of the triple points show the border of the transition between solid and gas (sublimation curve). These curves connect at the triple point. (b) Relative volatility α for $P(H_2)/P(HD)$ and $P(HD)/P(D_2)$ as a function of temperature.

The separation ability of the distillation is expressed in terms of NTP (Number of Theoretical Plates), which is defined by using the concentrations of a low-boiling component at the bottom and upper parts of the distillation unit [78]. In the case of the distillation of the HD gas, the NTP is given as;

$$NTP = \frac{\ln\left(\frac{[H_2]_{Top}}{1-[H_2]_{Top}}\right) - \ln\left(\frac{[H_2]_{Bot}}{1-[H_2]_{Bot}}\right)}{\ln\alpha}, \tag{7.1}$$

where $[H_2]_{Top}$ and $[H_2]_{Bot}$ are the concentrations of the H_2 gas at the top and bottom parts, respectively, and α is the relative volatility between H_2 and HD. To increase the separation ability, it is important to increase the NTP. The NTP depends on the structure and the surface area of the packs and the height of the stacked column. We designed the distillation system with NTP=37.9 as discussed later.

— 7.1.2 Apparatus —

Fig. 7.2 shows a schematic view of the HD gas distillation system. The upper part of the distillation unit is cooled with a cryogenic panel directly connected to the refrigerator, and the bottom part is warmed by radiation heating. The radiation shield is connected to the first stage of the refrigerator and is kept at a temperature of about 90~100 K. The distillation unit is cooled down to around 17 K. We use the refrigerator system (Refrigerator unit: RDK-408S, Compressor unit: CSW-71C) produced by Sumitomo Heavy Industries. The cooling power of the refrigerator is 35 W at 45 K in the first stage and 6.3 W at 10 K in the second stage. The lowest temperature of the second stage is 7 K. The temperatures and pressure in the distillation unit were monitored periodically. The distillation system has additional three distillation units to increase the productivity of pure HD gas in the future. Only one distillation unit was used in this experiment. The stainless steel packing called "Heli-pack" is filled into the distillation unit to promote the separation among the H_2, HD, and D_2 components. Heat exchange between gas and liquid takes place on the surface of the Heli-pack cells. A gas with a low-boiling component is extracted from the upper part of the distillation unit to the tanks through the mass flow controller.

The impurity of the extracted gas is monitored with a hydrogen isotope analyzer system which combines the Gas Chromatograph with the Quadrupole Mass Spectrometer (GC-QMS) [74]. In the gas chromatograph, a narrow capillary tube with a diameter of 0.50 mm is cooled at 110 K. Neon gas is used as a carrier gas. The p-H_2, o-H_2, HD, and D_2 are separated using the retention time of the narrow capillary tube and injected to the QMS. In the QMS, the analyzed gas is ionized at an ion source by electron bombardment. Ions are mass-separated according to the mass/charge ratio (u/e). The GC-QMS enables us to observe the p-H_2, o-H_2, HD, and D_2 gases separately by measuring the retention time in the GC and by determining the mass/charge ratios in the QMS.

Fig. 7.3 shows a sectional drawing of the distillation unit. The distillation unit consists of three parts. Each part has a gas inlet/outlet tube. The condenser part is made of copper. The outer casing of the rectification part is made of stainless steel. The outer casing of the reboiler part is made of copper. The specification of the distillation unit is listed in Table 7.1. Three silicon-diode temperature sensors

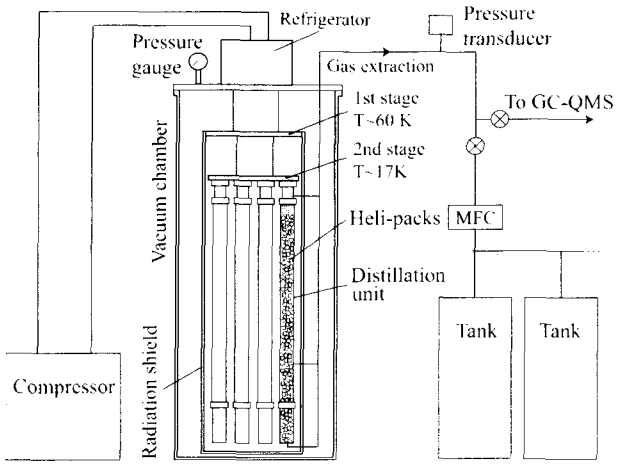

Figure 7.2: Schematic view of the HD gas distillation system. The distillation system is equipped with the refrigerator to liquefy the commercial HD gas. MFC is a mass flow controller. The mass flow controller (MC-3000L) is made by LINTEC Corporation. A pressure transducer is installed at the gas extraction line. GC-QMS is a gas analyzer system. The radiation shield is made of copper with a thickness of 1 mm.

are set for monitoring the temperature of the condenser, rectification, and reboiler parts. A film heater for controlling the temperature is wound around the condenser part. The power of the heater is 20~30 W. The reboiler part is warmed up by radiation heating. At the condenser part, the H_2 gas can only pass through to the extraction pipe, and the HD and D_2 are liquefied.

Fig. 7.4 shows a photograph of the Heli-packs. The distillation unit is filled with about 100,000 Heli-packs. Each pack has a rolled shape like a coil and is twisted for efficient heat conduction between gas and liquid. The NTP is determined from the HETP of the Heli-pack theoretically calculated as

$$NTP = \frac{Packed\ length}{HETP} = \frac{1100\ mm}{29\ mm} = 37.9 \tag{7.2}$$

With NTP=37.9, the H_2/HD ratio is enhanced by a factor of $1.74^{37.9}$ when the relative volatility α is assumed to be 1.74 at 20.5 K. If the H_2 concentration is 0.001% at the reboiler part, the H_2 is purified to 99.993% at the condenser part, which is derived from Equation (7.1).

— 7.1.3 Distillation procedure —

We operated three times to obtain pure HD gases by changing experimental parameters. Table 7.2 lists the experimental parameters for the distillation. The

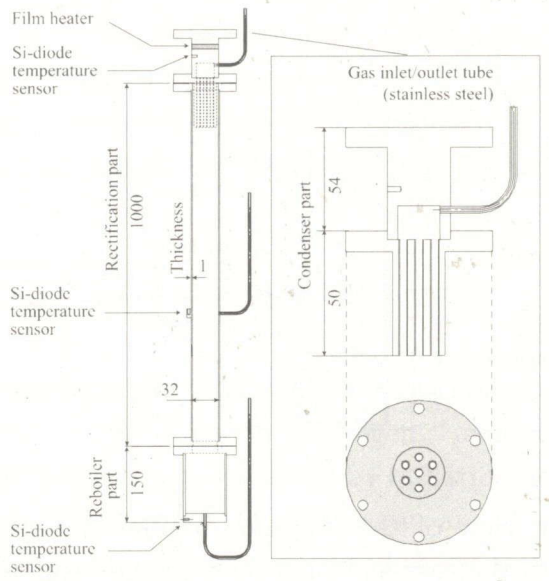

Figure 7.3: Sectional drawing of the distillation unit. At the bottom of the condenser part, seven screw holes are prepared for solidifying the commercial HD gas. All the numerical numbers are given in unit of mm.

Table 7.1: Specifications of the distillation unit and Heli-pack. The notation, SWG, indicates Standard Wire Gauge. HETP (Height Equivalent to a Theoretical Plate) [76] indicates the Heli-pack separation ability.

Specification of the distillation unit	
Material and Height	
Condenser part	Copper 110 mm
Rectification part	Stainless steel 1000 mm
Reboiler part	Copper 150 mm
Inner diameter	32 mm
Inner volume	1 L
Packed length	1100 mm
Specification of the Heli-pack [76]	
HETP	29 mm
Wire diameter (SWG)	0.0193 mm (#36)
Surface area	3160 m^2/m^3
Free volume	97.1%
Density	1450 kg/m^3
Material	Stainless steel

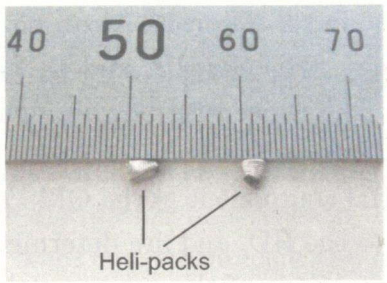

Figure 7.4: Photograph of Heli-packs which are filled into the rectification and reboiler parts.

amount of 5.2 mol of commercial HD gases in the tanks were fed into the distillation unit through the inlet/outlet tube, and solidified at the condenser part which was cooled at 8 K. The valve between the distillation unit and the tanks was closed after solidifying the HD gases. The HD solid was melted by heating up and was liquefied. It took 6 hours until realizing the equilibrium of H_2, HD, and D_2. The concentration of H_2 increased to more than 99%. The gas was extracted from the condenser part to the gas storage tanks made of stainless steel through the mass flow controller with a constant flow rate. The concentrations of H_2, HD, and D_2 were monitored by the GC-QMS during the gas extraction process. The temperature of the condenser part was controlled in the range of 17~21 K by changing the heater power.

Table 7.2: Experimental parameters for the distillation.

	Run 1	Run 2	Run 3
Temperature (K)	17.5	20.5	20.5
Extraction speed (ml/min)	1.3	1.3	5.2
Experimental period (day)	17	17	7

Section 7.2
Experimental results and analysis

— 7.2.1 Gas analysis of commercial HD gas —

Fig. 7.5 shows the results of the gas analysis for a commercial HD gas. Peaks of p-H_2, o-H_2, HD, and D_2 are observed with a good resolution. The continuous

component between the p-H_2 and o-H_2 peaks is caused from the para-ortho transition of H_2 in the capillary tube. The H_2, HD, and D_2 yields have been obtained by integrating the peak areas. The concentrations are calibrated by dividing the obtained yields by factors of 2.18 for H_2 and of 0.77 for D_2 because the sensitivities are different from those for the HD component in the QMS measurement. These factors are the relative sensitivities to the HD, and are determined by analyzing calibration gases. The calibrated concentrations of the commercial HD gas are 1.327±0.003%, 93.127±0.008%, and 5.546±0.007%, respectively for H_2, HD, and D_2.

The calibration gases have been prepared by mixing the HD gas and another gas (H_2 or D_2) with a ratio of 1:1. The factor of 2.18 is obtained from the analysis of a gas with HD and H_2. The factor of 0.77 is obtained from the analysis of a gas with HD and D_2. At the same location of the HD peak, other peaks are observed in the spectra with u/e=2 and u/e=4. These peaks are due to D^+ and H_2D^+, respectively, produced from the HD component as fragmentations at the ionization process in the QMS. A shape of the peak depends on the amounts of the components in the injected gas. When the amounts in the injected gas are relatively smaller than a receptible volume of the capillary tube, the width of the peaks is narrow. On the other hand, when the amounts are much larger than the volume of the capillary tube, we observe a broad peak. However, it is found that the distortion of the peak shape does not give any serious effect in determining the gas concentrations [74].

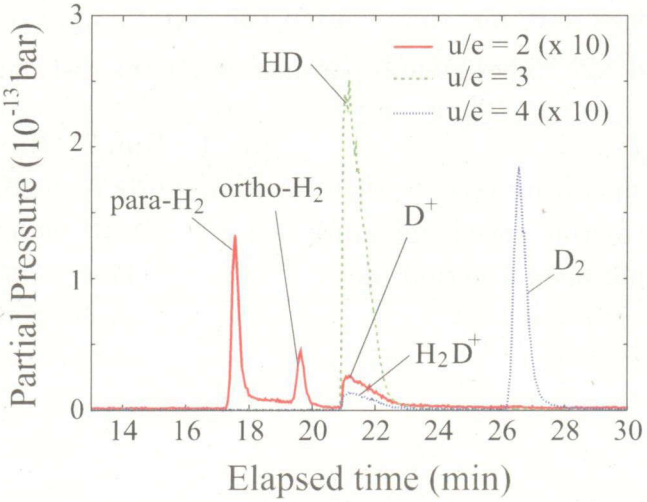

Figure 7.5: Results of the gas analysis with the GC-QMS for the commercial HD gas. The horizontal axis is the elapsed time after the gas injection to the gas chromatograph. The vertical axis is the partial pressure of each gas measured with the QMS. u/e is the mass/charge ratio. The solid line, dashed line, and dotted line show the spectra with u/e=2, 3, and 4, respectively.

— 7.2.2 Gas analysis of pre-extraction and effective NTP —

After feeding the commercial HD gas to the distillation unit, the distribution of the gas concentrations in the distillation unit reached to equilibrium in a few hours. The impurities, H_2 and D_2, were concentrated in the condenser and reboiler parts respectively. The temperatures at the condenser and reboiler parts were 20.5 K and 23.0 K, respectively. Fig. 7.6(a) shows the results of the gas analysis with the GC-QMS for the gas from the condenser part in Run 2 before the extraction. The p-H_2 and o-H_2 peaks are dominantly observed in the spectrum with u/e=2. The D_2 component is not observed clearly. The concentrations of the H_2, HD, and D_2 are 99.963±0.003%, 0.035±0.001%, and 0.002±0.001%, respectively. At the same location of the H_2 peaks, other peaks are observed in the spectrum with u/e=3. The peaks are due to H_3^+ produced from the H_2 component as a fragmentation. Fig. 7.6(b) shows the results of the gas analysis for the gas from the reboiler part before the extraction. The HD peak is dominantly observed in the spectrum with u/e=3. The D_2 peak is observed in the spectrum with u/e=4. The concentrations of the H_2, HD, and D_2 are 0.0018±0.0002%, 95.036±0.004%, and 4.962±0.002%, respectively.

An effective value of the NTP, which is an indication of the distillation performance, is derived from the concentrations of H_2 in the condenser and reboiler parts. The effective value of the NTP is experimentally obtained as

$$NTP = \frac{\ln\left(\frac{99.963\times10^{-2}}{1-99.963\times10^{-2}}\right) - \ln\left(\frac{0.0018\times10^{-2}}{1-0.0018\times10^{-2}}\right)}{\ln\alpha_g} = 37.2, \qquad (7.3)$$

where α_g is 1.66, which is the geometrical mean for 1.74 and 1.58, at the temperatures of 20.5 K and 23.0 K, respectively [77]. By taking the uncertainties of all the parameters into account, 37.2±0.6 is obtained for the NTP. The result of the NTP is in good agreement with a designed value of 37.9.

— 7.2.3 Gas analysis of purified HD —

The gas with a high H_2 concentration was extracted from the condenser part, and the HD concentration increased gradually. Fig. 7.7 shows results of the gas analysis near the end of the distillation in Run 2. The H_2 and D_2 components are not observed at the level of 0.001%. The concentration of the HD component is obtained to be 99.999±0.002%.

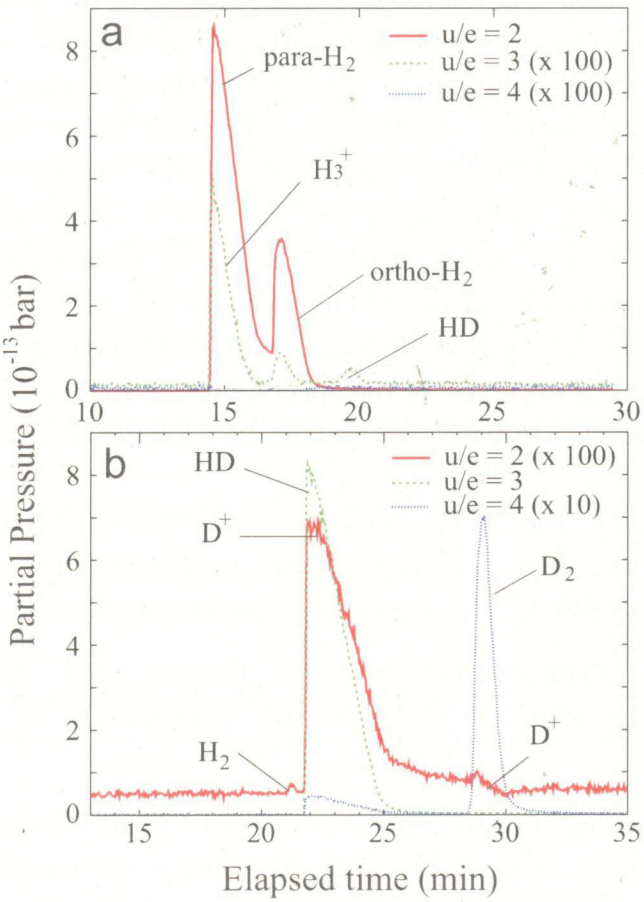

Figure 7.6: Results of the gas analysis with the GC-QMS for the gas from the condenser (a) and reboiler (b) parts before the gas extraction operation. Notations are the same as in Fig. 7.5.

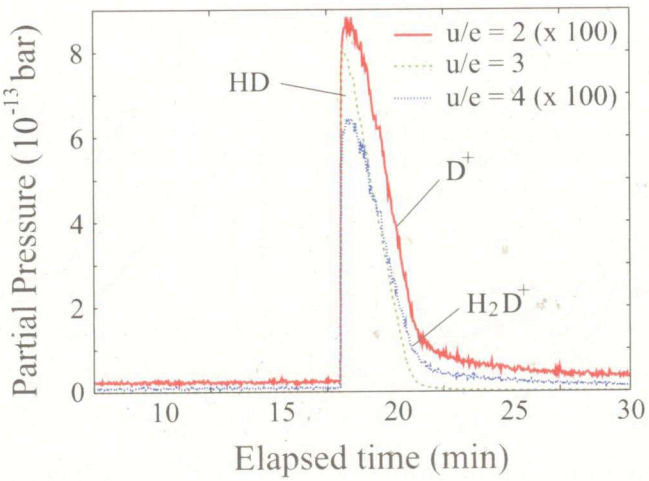

Figure 7.7: Results of the gas analysis with the GC-QMS for the distilled gas after the 14-day gas extraction at 20.5 K, and with an extraction speed of 1.3 ml/min. Notations are the same as in Fig. 7.5.

— 7.2.4 Reduction of the H_2 concentration —

Fig. 7.8(a) shows a concentration of H_2 including both p-H_2 and o-H_2, as a function of the extracted volume. The concentrations of the gas extracted from the condenser part are measured for Run 1, Run 2, and Run 3. The H_2 concentration at the condenser part is nearly 100% before extracting the gas. The H_2 concentration decreases as the gas is extracted from the distillation unit. At the end of Run 2, we confirmed that a very small amount of the D_2 component was detected, where D_2 concentration was 0.008±0.001%. The H_2 concentration reaches to 0.01% in Run 1. The H_2 concentrations reach the level under 0.001%, which is near the detection limit of the GC-QMS, after extracting 1.0 mol and 2.0 mol gases, respectively, in Run 2 and Run 3.

The H_2 concentration decreases rapidly in the early step, and gradually reaches the level under 0.1% at the extraction volume of 0.4 mol in Run 1. The H_2 concentration decreases continuously in Run 2. Judging from the comparison between Run 1 and Run 2, a small amount of the H_2 gas might have been trapped inside the solid D_2 around the condenser part at 17.5 K, and evaporates slightly in Run 1. The extraction efficiency of the H_2 component at the condenser-part temperature of 20.5 K is better than that at 17.5 K. The H_2 concentration drops rapidly to 0.3% in the early step, and gradually decreases with increasing the extraction volume in Run 3.

Fig. 7.8(b) shows H_2 concentration as a function of elapsed time. In Run 1, the H_2 concentration decreases rapidly in the period of 4 days, and gradually reaches the level under 0.1% at the extraction of 17 days. In Run 2, the H_2 concentration

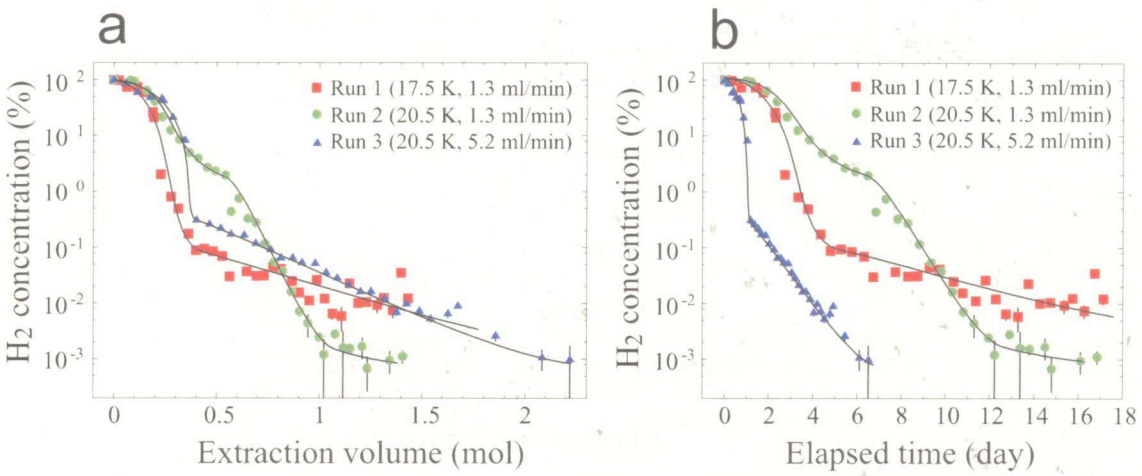

Figure 7.8: (a) The H_2 concentration in the distilled gas as a function of extracted gas volume. (b) The H_2 concentration in the distilled gas as a function of elapsed time. The squares are the results of the concentration with a temperature of 17.5 K and an extraction speed of 1.3 ml/min (Run 1). The circles are the results of the concentration with a temperature of 20.5 K and an extraction speed of 1.3 ml/min (Run 2). The triangles are the results of the concentration with a temperature of 20.5 K and an extraction speed of 5.2 ml/min (Run 3). The curves are given for convenience to guide the eyes.

decreases continuously, and reaches to the level of 0.001% after a long extraction time of 14.8 days. In Run 3, the H_2 concentration reaches to 0.01% at the extraction time of 4 days and 0.001% at the extraction time of 6 day. The periods of 17 days are needed to obtain the pure HD gas in Run 1 and Run 2, while the period is only 7 days in Run 3. At the end, we have obtained 1 mol of HD gas with a purity better than 99.99% from the extraction volume of 1.25 mol to 2.25 mol within a week in Run 3. In addition, the concentration of o-H_2 in the produced pure HD gas is smaller than 0.001%.

Section 7.3

Summary of new HD distillation system

We have developed a new cryogenic distillation system in order to produce a pure HD gas for the polarized HD target. The distillation system is equipped with a cryogenic distillation unit, which is cooled at 17∼21 K, filled with Heli-packs. We succeeded in obtaining 1 mol of the HD gas with a purity better than 99.99% for producing the polarized HD target. The highest concentration of HD is 99.999±0.002%

at the elapsed time of 14.8 days in Run 2. The effective NTP, an indicator of the distillation performance, is obtained to be 37.2±0.6, which is in good agreement with a designed value of 37.9.

Since the maximum amount of the D_2 component was 0.008% in the obtained high purity HD gas, the second distillation [44] for reducing the concentration of the D_2 component is not required. In addition, we tried to shorten the operation period for the HD distillation. The mass flow rate was set at 5.2 ml/min. The HD distillation period was, in the present work, shortened from 30 days [44] to 7 days. Since the pure HD gas can be produced with the new distillation system, the HD target will be efficiently polarized by adding an optimal amount of o-H_2 to the HD gas for future LEPS experiments at SPring-8.

Finally, it should be noted that during the course of the present work, we recognize that distillation using the Heli-packs is carried out in other laboratories, such as Los Alamos National Laboratory in USA for the ITER [79] and St. Petersburg Nuclear Physics Institute in Russia for the MuCap experiment [80]. The distillation system with Heli-packs for producing pure hydrogen isotopes will be more commonly used for various scientific and industrial applications in the near future.

Chapter 8

Summary

We have started to develop the polarized HD target since 2005 for hadron physics. A polarized HD target will be prepared at RCNP (Osaka University) and installed in the LEPS beam-line at SPring-8. The produced target is transferred from one refrigerator to another via 5 refrigerators. Since ortho-H_2 and para-D_2 prompt to decay polarization of HD target, highly purified HD gas is used for freezing the polarization. By many test experiments and training, the DRS for cooling down the target and the distillation system for the purification of HD gas have been prepared. We had tried to produce the polarized HD target in 2008-2009 as a first step.

The polarization degree and the relaxation time T_1 of the proton (H) were obtained by using the measured NMR spectra. The HD gas purified to 97.6% was fed to a dilution refrigerator and solidified. Then, the HD was cooled down to 14 mK with a high magnetic field of 17 T. The reference NMR data of H (B=1 T, T=4.2 K) at the thermal equilibrium state were measured. After the aging time of 53 days, the NMR spectra were obtained. The polarization degree of about 84% is possible for the proton at the temperature of 14 mK and at the magnetic field of 17 T. After 53 days, the polarization degree and the relaxation time were obtained as 40.8±2.3 (stat.)% and 112.8±0.1 (stat.) days, respectively. The relaxation time of 112.8 days is longer than the period of 60 days needed for taking data for investigating the nucleon hidden structure. The polarization degree measured is much lower than that expected from the thermal equilibrium of the aging condition. Non-linear relation between the NMR signal height and the polarization degree or extremely low impurity of o-H_2 is considered to be the main source of the low polarization degree. Extremely small amounts of o-H_2 and p-D_2 components in the purified HD gas do not probably grow the polarization of the HD target. The appropriate amount of impurities in the HD is approximately an order of 0.01%. We need to develop a device to analyze a concentration of o-H_2 with a high precision of about 0.001% in order to optimize the amount of impurities.

To establish the technology of making the polarized HD target, we have focused on developing the systems for NMR measurement and purifying the HD gas. The analysis of the hydrogen background indicates that the contribution from the enamel wire is large. Therefore, we replaced the enamel wire to the Teflon coated silver wire. A signal to noise ratio for the NMR measurement was largely improved by introducing 180-phase-combiners/dividers and a thermostatic box for an electric circuit. The portable NMR system (PXI-NMR) was developed for the NMR measurement for the use in both places of RCNP and SPring-8. The PXI-NMR allows us to perform

the NMR measurement anywhere and under the same condition. The gas analysis system (GC-QMS) and the distillation system for the HD gas (HD-Distill) were developed for purifying the HD gas. The GC-QMS allows us to analyze concentrations of o-H_2, p-H_2, HD and D_2 with a high precision of about 0.001%. The HD-Distill enables us to obtain one mol HD gas with a purity better than 99.99%.

Since the pure HD gas can be produced reliably with the new distillation system, the HD target will be efficiently polarized by adding an optimal amount of o-H_2 and D_2 to the HD gas. It is now possible for us to reduce the aging time for producing the polarized HD target and to have the spin-frozen HD target with a long relaxation time. We have established the technology of making the polarized HD target. We are ready to produce the polarized HD target for the hadron physics experiment at SPring-8.

Acknowledgments

I would like to thank the HD group members for all of their help and support.

I am gratefully acknowledge Dr Hideki Kohri. He has continuously encouraged me. He has been leading me to proceed the research, giving me many advises and taking remarkable care of me

I am grateful to Prof. Mamoru Fujiwara. A lot of his advices have helped me polish up the manuscripts of publications. I have spent the research work with his unwearying talk

I appriciate Prof Masaru Yosoi. He provided helpful comments and suggestions about NMR.

I am deeply appreciate to Dr Kohji Fukuda, Dr Takayuki Kunimatsu for many invaluable discussions with me. They have given me many suggestions for NMR measurement and analysis.

I thank J.-P. Didelez, S. Bouchigny, and G. Rouille for giving important advices to me.

I have a lot to thank Chiharu Morisaki, Su-Yin Wang, Keisuke Ueda and Satoshi Ono for working withe me in the construction of the HD target.

I thank Dr. T. Kageya for fruitful discussions and Prof. T. Kishimoto for his encouragement.

I would also like to express my gratitude to my family for their moral support and warm encouragements. The present work was supported in part by the Ministry of Education, Culture, Sports, Science and Technology in Japan and by the National Science Council of Republic of China (Taiwan). This work was also supported by Program for Enhancing Systematic Education in Graduate Schools and Department of Physics, Osaka University.

Appendix A

Relaxation time

The polarization reduces by depolarization which depends on the relaxation time. In the case of HD, The relaxation time T_1 change in real time and depends on the residual amount of the ortho-H_2.

T_{conv} is the conversion time from the ortho-H_2 to the para-H_2. The equation is shown as follows

$$T_1 = \frac{T_0}{N_{ortho-H2}} = \frac{T_0}{exp{-t/T_{conv}}},$$
$$T_0 = T_1 \ (t = 0).$$

The polarization is given as a function of time:

$$\begin{aligned}
\frac{dP}{dt} &= (1 - P(t))\frac{1}{T_1} \\
\frac{dP}{1 - P(t)} &= 1/T_1 dt \\
\frac{dP}{1 - P(t)} &= \frac{exp(-t/T_{conv})}{T_0} dt \\
-log(1 - P(t)) &= -\frac{T_{conv} exp(-t/T_{conv})}{T_0} + C \\
1 - P(t) &= exp\left\{\frac{T_{conv}}{T_0} exp(-t/T_{conv}) - C\right\}.
\end{aligned}$$

The polarization is 0 when t=0. Thus we obtain C=T_{conv}/T_0.

$$\begin{aligned}
P(0) &= 1 - exp\left\{\frac{T_{conv}}{T_0} exp(-t/T_{conv}) - \frac{T_{conv}}{T_0}\right\} \\
&= 1 - exp\left\{\frac{T_{conv}}{T_0}(exp(-t/T_{conv}) - 1)\right\}.
\end{aligned}$$

The amounts of o-H_2 converts to p-H_2 with time constant of 6.5 days. Then, T_{conv}=6.5 day,

$$P(t) = 1 - exp\left\{\frac{6.5}{T_0}(exp(-t/6.5) - 1)\right\}. \quad \text{(A.1)}$$

If T_0 is over one day, polarizing the H in the HD become to be hard. Figure A.1 shows decaying the amounts of o-H_2 with elapsed days. The amounts of o-H_2 decreases to 1/10 per 15 days. A effect under a high magnetic field and a low temperature to the conversion from o-H_2 to p-H_2 unknown. Figure A.1 shows the change

of polarization degree of the H with time constants of 1 days, 2 days, 5 days and 10 day. The polarization with the time constant of 1 day reaches expected polarization degree. The polarization with the time constant of 10 day become unable to reaches expected polarization since relaxation time T_1 is too long. This means that too small amounts of o-H_2 at the initial make the polarization degree of H in the HD do not grow the expected polarization degree.

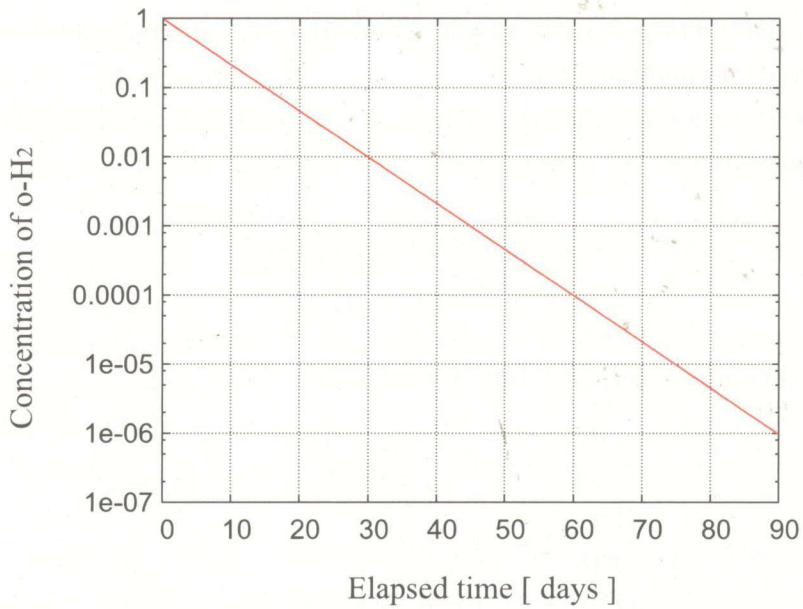

Figure A.1: Decaying the amounts of o-H_2 with elapsed days. The time constant of ortho-para conversion assumed to be 6.5 days.

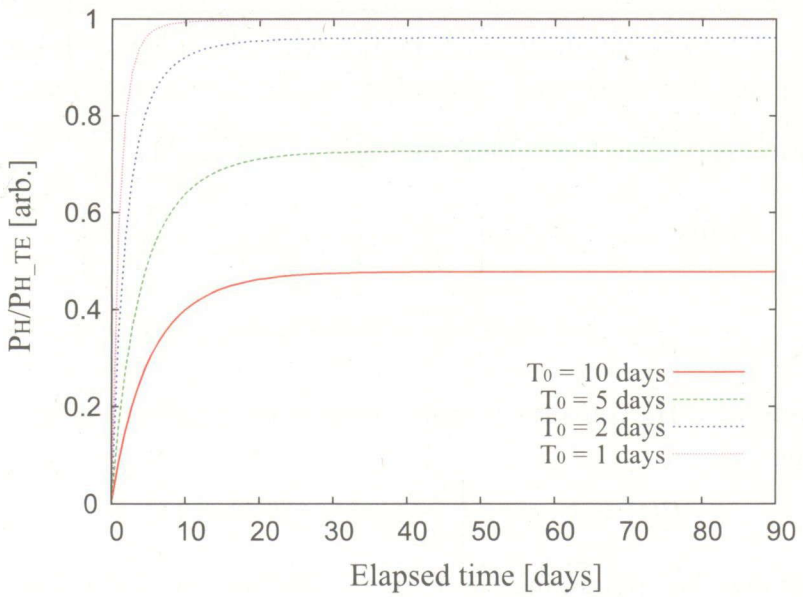

Figure A.2: The Polarization degree of the H with time constants of 1 days, 2 days, 5 days and 10 day.

Appendix B

Calculation of ortho-para ratio

The ortho-H_2 is an important factor for the relaxation time of the polarized HD target. At room temperature and thermal equilibrium, hydrogen consists of 25% para-H_2 and 75% ortho-H_2. The ortho-para ratio depends on the temperature, and the para-H_2 dominates at low temperature (approximate. 99.8% at 20 K). In this appendix, we consider the ortho-para ratio in each temperature.

The ortho-para ratio is obtained by calculating the partition function by taking the fact into account that the both the para-H_2 and the ortho-H_2 have the rotational excited states. The rotational partition function is written as

$$Z = \sum_{\infty}^{J=0} P_J e^{E_J/k_B T} \tag{B.1}$$

where E_J is a rotation energy, P_J is a degeneracies and k_B is the Boltzmann constant (8.65 eV/K). The energies of the rotational states is given by

$$E_J = \frac{J(J+1)\hbar^2}{2I} = BJ(J+1), \quad B = \frac{\hbar^2}{2I}. \tag{B.2}$$

Where B is called rotational constant. I denotes the moment of inertia of the molecule as

$$I = \mu R^2,$$

μ is the reduced mass of the molecule and R is the distance between the two atoms.

$$where\ \mu = \frac{m_1 m_2}{m_1 + m_2},$$

In the case of hydrogen molecular, the distance R is 0.741$\mathring{A}$. The reduced mass μ is $4.69 \times 10^8 eV/c^2$. The moment of inertia of the heydrogen molecule is obtained as follows,

$$I = \mu R^2 = \frac{4.69 \times 10^8}{(2.998 \times 10^8)^2} \times 0.741 \times 10^8 = 2.87 \times 10^{-27}\ [\mathrm{cV{\cdot}m^2}].$$

The rotation constant is

$$B = \frac{\hbar^2}{2I} = \frac{(6.58E-16)^2}{2 \cdot 2.87 \times 10^{-27}} = 7.56\ [\mathrm{meV}]$$

When the nuclear spin coupling is para (J=0,2,4..) and ortho (J=1,3..), the degeneracies P_J are given by

$$P_J = 2J + 1 : para\ (J = 0, 2, ..) \tag{B.3}$$

$$P_J = 3 \times 2J + 1 : ortho\ (J = 1, 3, ..) \tag{B.4}$$

The factor of 3 for ortho-H_2 accounts for the spin degeneracy associated with l_z = 1, 0, -1. The Partition function is written separately for ortho and para as

$$Z_{para} = \sum_{J=0,2..}^{\infty} (2J+1)exp(-\frac{7.56J(J+1)}{K_BT}) \tag{B.5}$$

$$Z_{ortho} = \sum_{J=1,3..}^{\infty} 3(2J+1)exp(-\frac{7.56J(J+1)}{K_BT}). \tag{B.6}$$

Table B.1: The calculated of the ortho-para ratio.

Temp	J = 0	J = 1	J = 2	J = 3	J = 4	para-H_2	ortho-H_2
300 K	0.132	0.665	0.115	0.084	0.003	25.10%	74.90%
200 K	0.191	0.718	0.069	0.021	0.000	26.10%	73.90%
150 K	0.252	0.705	0.038	0.005	0.000	28.97%	71.03%
100 K	0.386	0.604	0.010	0.000	0.000	39.61%	60.39%
77 K	0.517	0.480	0.003	0.000	0.000	52.02%	47.98%
50 K	0.786	0.214	0.000	0.000	0.000	78.63%	21.37%
20 K	0.999	0.001	0.000	0.000	0.000	99.86%	0.14%
10 K	1.000	0.000	0.000	0.000	0.000	100.00%	0.00%
4.2 K	1.000	0.000	0.000	0.000	0.000	100.00%	0.00%

Appendix C

Magnetic moments

Table C.1: Intrinsic magnetic moments of some elementary particles [81, 82, 83]

Nuclear spices	Spin	Magnetic dipole moment	Gyro-quadrupole moment	Magnetic magnetic ratio	Relative sensitivity to ^{1}H
	$I/\hbar$	μ/μ_n	μ/μ_n	γ [MHz/T]	γ^3/γ_H^3
^{1}H	1/2	2.79277	-	42.575	1.000E+00
^{2}H	1	0.857409	0.00282	6.536	9.647E-03
^{3}He	1/2	-2.12756	-	32.433	4.421E-01
^{7}Li	3/2	3.25629	-0.04	16.546	2.935E-01
^{11}B	3/2	2.68864	0.04	13.660	1.651E-01
^{13}C	1/2	0.702384	-	10.705	1.590E-02
^{14}N	1	0.40356	0.01	3.076	1.005E-03
^{15}N	1/2	-0.2831	-	4.314	1.040E-03
^{17}O	5/2	-1.89391	-0.026	5.772	2.907E-02
^{19}F	1/2	2.628363	-	40.069	8.336E-01
^{21}Ne	3/2	-0.66176	0.093	3.361	2.460E-03
^{23}Na	3/2	2.21752	0.11	11.261	9.253E-02
^{27}Al	5/2	3.64141	0.146	11.094	2.064E-01
^{29}Si	1/2	-0.55525	$< 10^{-4}$	8.458	7.839E-03
^{31}P	1/2	1.13166	-	17.235	6.634E-02
^{33}S	3/2	0.64327	-0.064	3.265	2.256E-03
^{35}Cl	3/2	0.82183	-0.079	4.171	4.703E-03
^{39}K	3/2	0.39141	0.09	1.987	5.083E-04
^{53}Cr	3/2	-0.47436	-0.03	2.406	9.023E-04
^{59}Co	7/2	4.616	0.4	10.054	2.765E-01
^{63}Cu	3/2	2.2262	-0.018	11.284	9.310E-02
^{67}Zn	5/2	0.87524	0.17	2.663	2.854E-03
^{113}Cd	1/2	-0.62249	-	9.449	1.093E-02
^{119}Sn	1/2	-1.0463	-	15.877	5.186E-02
^{127}I	5/2	2.8094	-0.79	8.518	9.343E-02
^{129}Xe	1/2	-0.77688	-	11.776	2.116E-02
^{195}Pt	1/2	0.60591	-	10.278	1.407E-02

Bibliography

[1] D. Adams *et al.*, Phys. Lett. B **329**, 399 (1994).

[2] K. Abe *et al.*, Phys. Rev. Lett. **74**, 346 (1995).

[3] L.A. Ahrens *etal.*, Phys. Rev. D **35**, 785 (1987).

[4] J.F. Donoghue and C.R. Nappi, Phys. Lett. B **168**, 105 (1986).

[5] A. Bertin *et al.*, Phys. Lett. B **388**, 450 (1996).

[6] D.S. Armstrong *et al.*, Phys. Rev. Lett. **95**, 092001 (2005).

[7] A. Acha *etal.*, Phys. Rev. Lett. **98**, 032301 (2007).

[8] A. Airapetian *et al.*, Phys. Rev. Lett. **92**, 012005 (2004).

[9] A.I. Titov, Y. Oh, and S.N. Yang, Phys. Rev. Lett. **79**, 1634 (1997).

[10] T. Mibe *et al.*, Phys. Rev. Lett. **95**, 182001 (2005).

[11] W.C. Chang *et al.*, Phys. Rev. C **82**, 015205 (2010).

[12] W.C. Chang *et al.*, Phys. Lett. B **658**, 209 (2008).

[13] W.C. Chang *et al.*, Phys. Lett. B **684**, 6 (2010).

[14] T. Ishikawa *et al.*, Phys. Lett. B **608**, 215 (2005).

[15] R.G.T. Zegers *et al.*, Phys. Rev. Lett. **91**, 092001 (2003).

[16] M. Sumihama *et al.*, Phys. Rev. C **73**, 035214 (2006).

[17] K. Hicks *et al.*, Phys. Rev. C **76**, 042201(R) (2007).

[18] H. Kohri *et al.*, Phys. Rev. Lett. **97**, 082003 (2006).

[19] M. Niiyama *et al.*, Phys. Rev. C **78**, 035202 (2008).

[20] K. Hicks *et al.*, Phys. Rev. Lett. **102**, 012501 (2009).

[21] N. Muramatsu *et al.*, Phys. Rev. Lett. **103**, 012001 (2009).

[22] H. Kohri *et al.*, Phys. Rev. Lett. **104**, 172001 (2010).

[23] M. Sumihama *et al.*, Phys. Lett. B **657**, 32 (2007).

[24] M. Sumihama *et al.*, Phys. Rev. C **80**, 052201(R) (2009).

[25] T. Nakano *et al.*, Phys. Rev. Lett. **91**, 012002 (2003).

[26] T. Nakano *et al.*, Phys. Rev. C **79**, 025210 (2009).

[27] M. Fujiwara *et al.*, Photoproduction Experiment with Polarized HD Target at SPring-8, LEPS/RCNP proposal (2003).

[28] A. Honig *et al.*, Nucl. Instr. and Meth. in Phys. Research, **356** 39 (1995).

[29] J.-P. Didelez, Nuclear Physics News, Vol 4, N^0 **3**, 10 (1994).

[30] A. Honig *et al.*, Nucl. Instr. and Meth. in Phys. Research **356**, 39 (1995).

[31] A. Honig, Phys. Rev. Lett. **19**, 1009 (1967).

[32] R.S. Rubins, A. Feldman, and A. Honig, Bull. Am. Phys. Soc. **11**, 907 (1966) .

[33] T. Moriya and K. Motizuki, Progr. Theoret. Phys. **18**, 183 (1957).

[34] K. Motizuki ann T. Nagamiya, J. Phys. Soc. Japan **11** 93 (1956).

[35] A. Honig et al., Workshop on Polarized Ion Source and PolarizedTargets, University of Wisconsin, Madison, May 23-27, 1993, eds. L.W. Anderson and W.

Haeberli, AIP Conf. Proc. **No. 213**, 50 (1994).
[36] A. Honig et al., Nucl. Instr. and Meth. A **356**, 39 (1995).
[37] X. Wei et al., Physica B **284**, 2051 (2000) .
[38] X. Wei et al., AIP Conf. Proc. **570**, 846 (2001).
[39] X. Wei et al., Nucl. Instr. and Meth. A **426** 157 (2004).
[40] M. Breuer et al., Nucl. Instr. and Meth. A **415**, 156 (1998).
[41] G. Rouillé et al., Nucl. Instr. and Meth. A **464**, 428 (2001).
[42] M. Bassan et al., Nucl. Instr. and Meth. A **526**, 163 (2004).
[43] S. Bouchigny, C. Commeaux, J.-P. Didelez, and G. Rouillé, Nucl. Instr. and Meth. A **544**, 417 (2005).
[44] S. Bouchigny, J.-P. Didelez, F. Dubois, and G. Rouillé, Nucl. Instr. and Meth. A **607**, 271 (2009).
[45] S. Hoblit et al., (LEGS-Spin Collaboration), Phys. Rev. Lett. **102**, 172002 (2009).
[46] Approved experiment at Hall B in Jefferson Laboratory, http://www.jlab.org/exp_prog/proposals/06/PR-06-101.pdf
[47] H. Kohri et al., Nuclear Physics Review Vol.26 Suppl. pp.79-82 (2009).
[48] H. Kohri et al., International Journal of Modern Physics E **19**, 903 (2010).
[49] H. Kohri et al., Journal of Physics : Conference Series Vol.295 012025 (2011).
[50] C. Morisaki, Master Thesis, Department of Physics, Osaka University, Osaka, Japan (2009).
[51] S. Y. Wang, Master Thesis, Department of Physics, National Kaohsiung Normal University, Kaohsiung, Taiwan(2009).
[52] K. Ueda, Master Thesis, Department of Physics, Osaka University, Osaka, Japan (2010).
[53] S. Ono, Master Thesis, Department of Physics, Osaka University, Osaka, Japan (2011).
[54] N. doshita, K. kondo, T. Iwata, Journal of Physical society of Japan Vol.66 No.12, pp905-913 (2011)
[55] A. Honig and H. Mano, Phys. Rev., **14**, 1858 (1976).
[56] A. Honig *et al.*, Spin96, Proceedings of the 12th Int. Symp. on High-Energy Spin Physics, Amsterdam Sept. 1996, edited by C.W. de Jager et al., in World Scientific, p. 365.
[57] Christopher M.Bade, Doctoral dissertation, the College of Arts and Sciences (2006)
[58] T. Ohta *et al.*, Annual report of RCNP Osaka university (2006).
[59] K.R. Jefferey and R.L. Armstrong, Rev. Sci. Instr. **38**, 634 (1967).
[60] E. Fukushima and S. B. W. Roeder, Experimental Pulse NMR, Westview press, Colorad p.393 (1981) .
[61] M.P. Klein and D. E. Phelps, Rev. Sci. Instrum. **38**, 1545 (1967).
[62] A. Abragam, Oxford University Press Inc., New York (1961).

[63] F Bloch, Phys. Rev. **70**, 460 (1946).
[64] M. Goldman, J.Magn. Reson. **17** 393 (1975) .
[65] G.R. Court, et al., Nucl. Instr. and Meth. A **324**, 433 (1993).
[66] K.Kondo, et al., Nucl. Instr. and Meth. A **526**, 70 (2004).
[67] PXI system alliance: http://www.pxisa.org/Specifications.html.
[68] C.S. Whisnant, P.A. Hansen, T.D. Kelley, Rev. Sci. Inst. **82**, 024101 (2011) .
[69] MKS Instruments homepage, http://www.mksinst.com.
[70] S. Bouchigny, PhD Thesis, Université Paris-SudXI, Orsay IPN0-T-04-07 (2007).
[71] http://www.varianinc.com/.
[72] K. Lan and J. W. Jorgenson, J. Chromatography A **915** (2001).
[73] A. D'Angelo, Private communications.
[74] T. Ohta et al., Nucl. Instr. and Meth. A 640 (2011) 241.
[75] M. Enoeda, T. Yamanishi, H. Yoshida, Y. Naruse, H. Fukui and K. Muta, Fusion Engineering and Design **10**, 319 (1989).
[76] TO-TOKU Engineering Corporation homepage (in japanese), <http://to-toku.co.jp/>
[77] Chemical engineering handbook 6th revision, The society of chemical engineerings, Japan, 1999, p. 18 (in Japanese).
[78] M.R. Fenske, Ind. Eng. Chem. **24**, 482 (1932) .
[79] Y. Iwai, T. Yamanishi, H. Nakamura, K. Isobe, M. Nishi and R. S. Willms, J. Nucl. Sci. Tech. **39**, 661 (2002).
[80] Cryogenic and Superconductive Techniques, Laboratory High Energy Physics Division of St. Petersburg Nuclear Physics Institute. <http://lkst.pnpi.nw.ru/projects/dru/>
[81] Rika Nenpyo (Chronological Scientific Tables 2007), National Astronomical Observatory, Japan, 2007, p. 102
[82] Proceedings of the International Conference on Nuclear Moments and Nuclear Structure, 1972
[83] Suppl. J. Phys. Soc. Jpn. **34**, 601 (1972).

List of Figures

List of Tables